

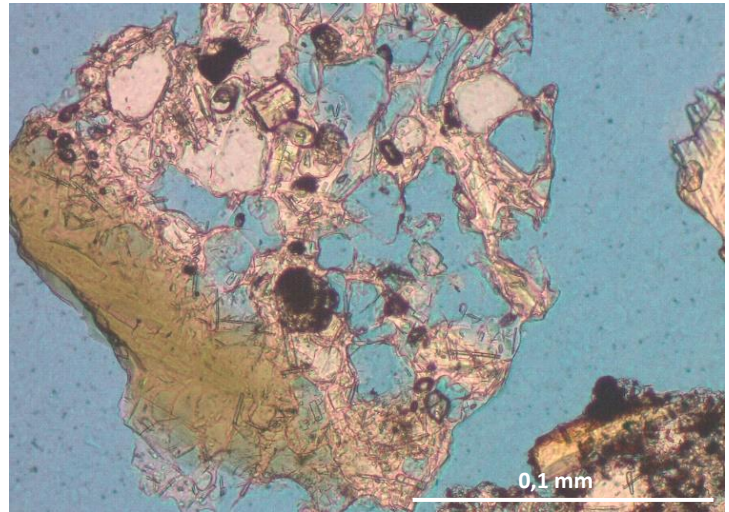
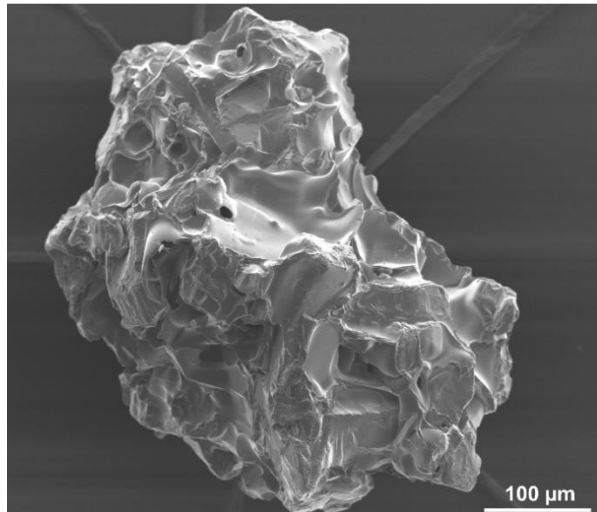


Freiberg Online Geoscience

FOG is an electronic journal registered under ISSN 1434-7512



2019, VOL 55



Marie-Luise Richter & Christoph Breitzkreuz

Granulometry and microtextures on grain surfaces from subaerial and submarine deposits of recent eruptions of Soufrière Hills Volcano, Montserrat

71 pages, 30 figures, 7 tables, 98 references

Abstract

Montserrat - a small island of the Lesser Antilles in the Caribbean - has received great attention in recent decades for the volcanic activity of the Soufrière Hills. Many scientists have studied the processes inside and outside the volcano intensively. This study examines the processes and effects that modify the morphology of the individual particles in the volcanic vent, during eruption and transportation of the pyroclasts up to the deposition on land or in the sea. Thereby it was essential to identify and characterize different microtextures on the grains and to define their origin.

Grain size analysis, grain shape and point counting measurements as well as microscopy were applied on eighteen samples of various origin. Here, the analysis of 50 selected grains of each sample on the SEM was of major importance. With the help of selected literature, an overview was created in which the surface structures of various processes from eruption, transport - as ashfall, pyroclastic flow, block-and-ash flow or turbidite current- to deposition on were summarized.

Differences were mainly observed in the grain size analysis, which was divided into three zones. These consist of offshore samples (zone I), ashfall deposits (zone II) and reworked beach samples (III) influenced by several volcanic transport (pyroclastic flows, surges, block-and-ash flows) and climatic processes. Further significant differences could not be observed among the individual environments, but it was possible to associate the microtextures with the formation processes eruption, transport and deposition and to determine relationships between one another. In addition, an overview of the microtextures identified on the grains could be provided. A combination of different classifications of surface structures, which until then had mainly been applied to quartz grains, and the SEM investigation of pyroclasts (mainly of basaltic origin) was carried out.

Acknowledgements

This work would not have been possible without the samples provided by Prof. S. Sparks of the University of Bristol and Dr. Adam Stinton and the MVO staff. The British Ocean Sediment Core Research Facility (BOSCORF) is thanked for supplying the offshore sediment samples.

We acknowledge Dr. Birgit Gaitzsch of the TU Bergakademie Freiberg as a reviewer of this thesis. We would also like to thank Gitta Schneider for the use of the sediment laboratory and permanent help in case of problems, Dr. Michael Magnus for the production of the thin sections and the data for grain shape and point counting analysis and Anja Obst of the SEM laboratory who spent hours with photographing over a thousand grains on the REM. Without their passionate participation and input, the basis of this thesis could not have been successfully conducted.

Table of Contents

LIST OF FIGURES	1
LIST OF TABLES	2
LIST OF ABBRAVIATIONS	3
1. INTRODUCTION	4
2. GEOLOGICAL BACKGROUND	5
2.1 Regional setting.....	5
2.2 Geology of Montserrat.....	6
2.3 Recent activity (1995-2013).....	8
2.4 Lava dome eruptions and the transition of pyroclastic flows.....	9
2.4.1 <i>Vulcanian eruptions</i>	10
2.4.2 <i>Pyroclastic flows and interaction with sea water</i>	11
2.5 Granulometry and microtextures – Previous studies.....	12
3. MATERIAL AND METHODS	14
3.1 Samples.....	14
3.2 Laboratory analysis.....	16
3.2.1 <i>Sieving</i>	16
3.2.2 <i>Grain size analysis</i>	16
3.2.3 <i>Grain Shape Analysis</i>	17
3.2.4 <i>Sample preparation</i>	18
3.3 Microscopic examination methods.....	18
3.3.1 <i>Optical Microscopy</i>	18
3.3.2 <i>Scanning Electron Microscopy (SEM)</i>	19
4. RESULTS	20
4.1 Grain size analysis and statistic parameters.....	20
4.2 Grain shape analysis.....	23
4.3 Microscopy.....	24
4.3.1 <i>Offshore samples</i>	24
4.3.2 <i>Vulcanian ashfall samples</i>	25
4.3.3 <i>Co-pyroclastic flow ashfall samples</i>	26
4.3.4 <i>Belham Valley (BV) & Plymouth (Plym) samples</i>	26
4.3.5 <i>Trant’s and Spanish Point Samples</i>	27
4.4 Point Counting.....	29

4.5	Microtextures	30
4.5.1	<i>Grain outline and relief</i>	30
4.5.2	<i>Mechanical features</i>	32
4.5.3	<i>Chemical features</i>	38
4.5.4	<i>Other features</i>	44
5.	DISCUSSION	48
5.1	Granulometry	48
5.2	Microtextures	49
5.2.1	<i>Eruption mechanisms</i>	49
5.2.2	<i>Transport processes</i>	49
5.2.3	<i>Deposition</i>	50
6.	CONCLUSION	52
7.	REFERENCES	53
APPENDIX	59

LIST OF FIGURES

Figure 1: A – Map of the Lesser Antilles showing the evolution of the island arc. The green dotted line marks the older limestone Caribbees and the red line the recent volcanic arc (modified after NAGLE & STIPP 1976, and MACDONALD ET AL. 2000). B – Map of Central America with the Lesser Antilles in the westernmost part (black box). Online map from d-maps.com (2018). C – Geological map of Montserrat showing the stratigraphic units Silver Hills, Centre Hills, Soufrière Hills and South Soufrière Hills. The dotted areas around Garibaldi and St. George’s Hill are uplifted by tectonic forces (modified after ZELLMER ET AL., 2003). 5

Figure 2: Bathymetric map of Montserrat and offshore regions with the Belham Valley Fault (black line) and a suggested fault trending NW-SE through Centre Hills (dashed line) 8

Figure 3: Typical sequence of a Vulcanian eruption in 1997 at Soufrière Hills on Montserrat adopted from DRUITT ET AL. (2002)..... 10

Figure 4: Schematic profile shows a typical Soufrière type Vulcanian eruption on Montserrat characterized by the collapse from the eruption column..... 11

Figure 5: Location map of the analysed samples (red points) with an overview of the Lesser Antilles island arc. 14

Figure 6: Detail of the topographic W-E profile of Montserrat from Soufrière Hills Volcano peak down to the Tar River Valley and the area offshore with the water depth of the samples JR123-15-V and JR123-23-V (modified after TROFIMOV ET AL., 2008)..... 15

Figure 7: Scanning electron microscope JEOL JSM-7001F at the Institute of Geology in Freiberg (left). The right image shows the opened sample chamber with carbon coated mount. 19

Figure 8: Comparison of grain size frequency histograms of the analysed samples; the classification of the grain sizes was adopted from BLOTT & PYE (2001)..... 20

Figure 9: Median diameters vs. sorting coefficients of the 18 samples. 22

Figure 10: Overview of the cumulative percentage of the roundness classes after POWERS (1953) calculated for each sample..... 23

Figure 11: **A** –Lithic clast (C) with granular groundmass of plagioclase and pyroxene (centre). JR123-23-V. **B** – Porphyritic clasts (C) with plagioclase and clinopyroxene phenocrysts in a vitric matrix surrounded by hornblende (Hbl) and plagioclase (Pl) crystal fragments. JR123-15-V. **C** –Overview of porphyritic clasts (C) and broken plagioclase (Pl) crystals. JR123-23-V. **D** – Plagioclase and pyroxene crystals are irregularly distributed in the vitric matrix of a clast (C). JR123-23-V. All images were taken under crossed nicols..... 24

Figure 12: **A** – Overview of sample MVO1703 with juvenile andesite lava fragments (C) and broken plagioclase (Pl) crystals. Crossed nicols. **B** – Glomerophytic clast (C) consisting of plagioclase, hornblende and pyroxene crystals. MVO1701. Crossed nicols. **C** – Vitric pumice with plagioclase and opaque mineral phenocrysts showing flow foliation. MVO1702. **D** – Pumice with elongated vesicles, plagioclase and opaque minerals as phenocrysts in the matrix. MVO1701. **E** – Glass shard with a single large vesicle and with amphibole phenocrysts. MVO1701..... 25

Figure 13: **A** – Highly vesicular lava fragment (C)t with plagioclase and phenocrysts in the groundmass. MVO290. Crossed nicols. **B** – Juvenile clast (C) with orthopyroxene crystals in a coarse-grained vitreous groundmass rich in plagioclase, orthopyroxene (Opx) and opaques. MVO290. Crossed nicols..... 26

Figure 14: **A** – Etched pyroxene crystal with characteristic needle-like endings. BV1. **B** – SEM picture of an etched pyroxene grain of BV1. **C** – Highly vesicular clast with plagioclase, hornblende and opaque mineral phenocrysts. BV1. **D** – Twinned plagioclase crystals in a glassy groundmass. BV2. **E** – Amphiboles with a striking foamy glass rim. BV2. **F** – Overview of a porphyritic andesite clast and an

opaque mineral phase. BV2. **G** – Clast with a homogeneous groundmass of plagioclase, pyroxene and the opaque mineral phase identified as magnetite. BV3. Crossed nicols. **H** – Glomerophytic texture of plagioclase and pyroxene. Plym01. Crossed nicols. **I** – Juvenile lava fragment with a medium vesicularity. Plym01..... 27

Figure 15: A – Highly vesicular juvenile lava fragment. Spanish Point. **B** – Glomerophytic texture of plagioclase and pyroxenes. Trant’s 1. **C** – Fine-grained andesite clast with phenocrysts of plagioclase and opaque minerals. Spanish Point. Crossed nicols. **D** – Plagioclase with oscillating zonation and a flame-like wall. Spanish Point. **E** – SEM picture of a plagioclase crystal with a bubble-wall texture for comparison with the thin section. Spanish Point..... 28

Figure 16: Cumulative percentage of rock fragments and phenocrysts estimated by point counting. 29

Figure 17: The upper diagram shows the grain outline of the analysed grains and their association to low (rounded), medium (subangular) and high (angular). The lower diagram depicts the relief regarding to the classification low (smooth), medium (semi-smooth) and high (irregular). 31

Figure 18: SEM micrographs of the different types of grain outline and relief. 32

Figure 19: SEM micrographs of surface textures on grains to compare flat cleavage, fresh and weathered surfaces. 33

Figure 20: SEM micrographs of surface textures on grains. 35

Figure 21: SEM micrographs of surface textures on grains. 36

Figure 22: Micrographs of some surface textures on grains..... 37

Figure 23: SEM micrographs of surface structures caused by mechanical stress..... 39

Figure 24: SEM micrographs of dissolution etching on grain surfaces. 40

Figure 25: SEM micrographs showing vesicularity and glassy coating. 42

Figure 26: SEM micrographs of some chemical features on grain surfaces. 43

Figure 27: SEM micrographs of other features. 44

Figure 28: SEM micrographs of juvenile lava fragments..... 45

Figure 29: SEM micrographs of the grain size fractions 63 – 100 μm and < 63 μm 46

Figure 30: The grain size distribution of all samples is depicted and a clear differentiation between the individual sample groups can be achieved..... 48

LIST OF TABLES

Table 1: Classification of the morphology and texture of pyroclasts from hydrovolcanic eruptions... 13

Table 2: Source type and setting of the samples. 15

Table 3: Selected grain shape descriptors after DIN ISO 9276-6. 17

Table 4: Distribution type and statistics summary (values of Φ) after FOLK & WARD (1957) 21

Table 5: Summary statistics of the grain size data..... 21

Table 6: Overview of the microtextures and their frequency subdivision..... 47

Table 7: Overview of the microtextures observed in the studied samples 51

LIST OF ABBRAVIATIONS

IODP – Integrated Ocean Drilling Program

SEM – Secondary Electron Microscope

MVO – Montserrat Volcano Observatory

BOSCORF – British Ocean Sediment Core Research Facility

BV – Belham Valley

Plym – Plymouth

GRADISTAT – Grain size Distribution and Statistics

SE – Secondary Electron

1. INTRODUCTION

Clastic particles can provide information on chemical and physical processes that have affected them during sedimentation based on their shape and textural characteristics. The grains of a beach, which have been influenced by water energy and wave activity, can be distinguished from wind-affected grains from a desert or particles of a glacial environment by their signature. Volcanic clasts, which are more complex than sedimentary grains, can provide a wide range of information on the physical and chemical conditions in the magma chamber up to the volcanic vent, the degree of explosivity, the mode of sedimentation, or hydrothermal as well as weathering processes.

This thesis is part of the IODP 340 project with the main goal of understanding the constructive and destructive processes along the volcanic arc of the Lesser Antilles (LE FRIANT ET AL., 2015). However, the study area of this work is restricted to Montserrat and its products of recent volcanic activity. Montserrat is a highly investigated island of the Lesser Antilles island arc, which has caught attention especially over the last two decades through a strong volcanic activity of the Soufrière Hills volcano.

The aim of this work is to find out if there are special microtextures on grains of andesitic to dacitic composition of Montserrat that have been formed as a result of volcanic activity near the coast. In this context, not only the processes within the volcano or during the ejection of volcanic material are of importance, but also the transport medium (as pyroclastic flow, surge, block-and-ash flow, ash fall or submarine mass flow) and the interaction with water, for example when pyroclastic flows reach the sea. For this purpose, about 50 grains of each of the 18 subaerial and submarine samples were examined with the SEM. In addition, grain size and grain shape analysis were accomplished to complete the investigations of microtextures. Furthermore, the petrographic composition of the samples was determined using microscopy and point-counting methods.

2. GEOLOGICAL BACKGROUND

The following paragraph provides an overview of the geological situation of the Lesser Antilles, the evolution of the island of Montserrat and the volcanic activity of Soufrière Hills Volcano, especially since the mid-1990s. Furthermore, there is a description of vulcanian eruptions, and the entrance of subaerial pyroclastic flows into the ocean.

2.1 Regional setting

Montserrat is a small volcanic island located in the northern part of the Lesser Antilles in the Caribbean Sea (Figure 1). The Lesser Antilles extend as an island arc about 850 km in NS direction along the eastern margin of the Caribbean Plate (BOUYSE, 1984; WADGE & SHEPHERD, 1984). It is a subduction zone in which the Atlantic Plate slides under the Caribbean Plate, with a relatively low subduction rate of

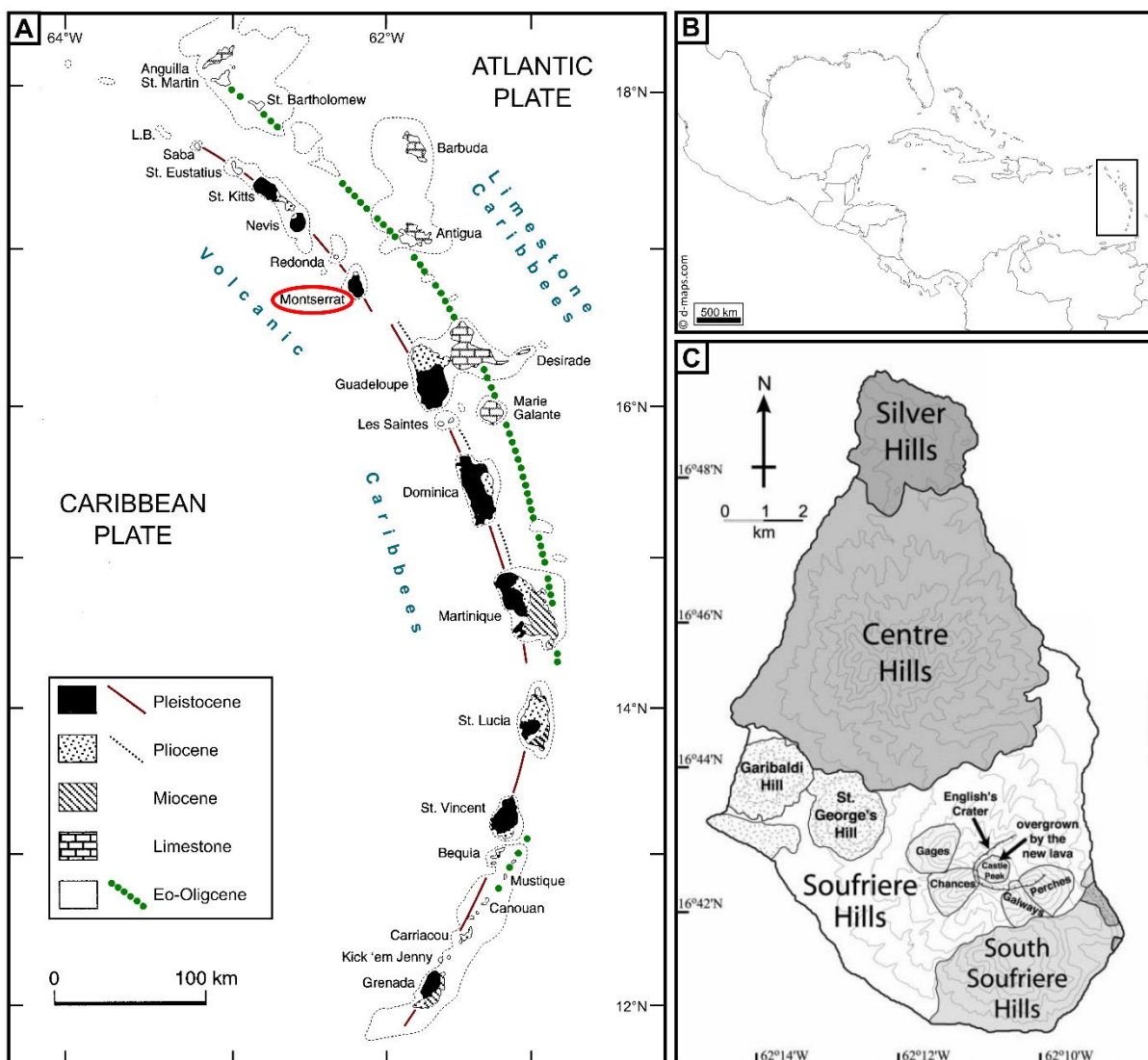


Figure 1: A – Map of the Lesser Antilles showing the evolution of the island arc. The green dotted line marks the older limestone Caribbees and the red line the recent volcanic arc (modified after NAGLE & STIPP 1976, and MACDONALD ET AL. 2000). B – Map of Central America with the Lesser Antilles in the westernmost part (black box). Online map from d-maps.com (2018). C – Geological map of Montserrat showing the stratigraphic units Silver Hills, Centre Hills, Soufrière Hills and South Soufrière Hills. The dotted areas around Garibaldi and St. George's Hill are uplifted by tectonic forces (modified after ZELLMER ET AL., 2003).

2 - 4 cm a⁻¹ (MACDONALD ET AL., 2000). As a result, a slightly curved, volcanically active island arc has developed - the Lesser Antilles. The extension ranges from the South American continental margin to the Anegada Passage, which is the boundary to the Greater Antilles (BOUYSE, 1984). A further subdivision of the islands from the northwest to the southeast are the Leeward Islands (British Virgin Islands, Anguilla, Saint Martin, Saint Barthelemy, Saba, Saint Eustatius, Saint Kitts, Nevis, Barbuda, Antigua, Montserrat, and Guadeloupe), the Windward Islands (Dominica, Martinique, Saint Lucia, Barbados, Saint Vincent and the Grenadines, Grenada, Tobago, and Trinidad) and the Leeward Antilles Islands (Aruba, Curaçao and Bonaire), which are usually not associated with the Lesser Antilles island arc (ALLEN, 2017). MARTIN-KAYE (1969) described the Lesser Antilles as a 'double arc' encompassing an older and a more recent island arc that join at Martinique and continue southwards. The eastern part of the double arc is called Limestone Caribbees and the western branch is named Volcanic Caribbees. According to WESTERCAMP (1988), the older island arc evolved in a period from the early Eocene (about 50 Ma) to the Oligocene (about 30 Ma). Subsequently, an 8 Ma long period of quiescence took place until subduction resumed in the early Miocene (about 22 Ma ago) and the western island arc evolved. The volcanic activity of the older island arc declined, and sedimentation of calcareous deposits occurred during the Neogene. Today, thick limestone banks cover the volcanically induced basement of the islands. For detailed information about the tectonic evolution of the Caribbean Sea and the Lesser Antilles island arc see ALLEN (2017). The low subduction rate of 2-4 cm/a also results in a low magma production rate, which according to MACDONALD ET AL. (2000) is about 3 - 5 km³ Ma⁻¹ km⁻¹. Therefore, specific characteristics regarding the magma compositions occur. The magma in the northern part of the island arc has a tholeiitic composition, in the central part it is calcalkaline and in the area of Grenada and the Grenadines alkaline (WESTERCAMP, 1988).

2.2 Geology of Montserrat

The island of Montserrat is located in the northern-central part of the volcanic active inner arc (Leeward Islands). The extension of the island is 16.5 km in NS direction and 10 km from west to east. The geographical location results in a humid tropical sea climate with large variations in precipitation over the year and an influence by hurricanes in the months July to December (ALLEN, 2017). The 160 km² large island comprises three volcanic massifs (see Figure 1 C): Silver Hills (ca. 2.17 - 1.03 Ma), Centre Hills (ca. 1.14 - 0.38 Ma), Soufrière Hills and South Soufrière Hills (ca. 0.45 Ma to present). The presented and most recent ages were determined via ⁴⁰Ar/³⁹Ar-dating (HATTER ET AL., 2018). The age sequence from old to young (North to South) results in a characteristic geomorphology that is flat in the north and steeper in the south (LE FRIANT ET AL., 2004).

Silver Hills is a deeply eroded volcanic centre in the north of Montserrat and is built up of the oldest rocks (two-pyroxene andesites; REA, 1974) of the island (HATTER ET AL., 2018). Areas of hydrothermal alteration (e.g. Yellow Hole), debris avalanche deposits (e.g. Little Bay), volcanoclastic sequences and eroded lava domes are typical (HARFORD ET AL., 2002; HATTER ET AL., 2018).

Located south of Silver Hills, the Centre Hills consists mainly of two-pyroxene andesite and hornblende-hypersthene andesite (REA, 1974; HATTER ET AL., 2018). The andesitic volcanoclastic material has been deposited by block-and-ash flows, pumice-and-ash flows, pumice falls, lahar, fluvial and debris avalanche deposits (HARFORD ET AL., 2002; HATTER ET AL., 2018). The centre is composed of remnants of massive andesitic lava domes (HARFORD ET AL., 2002). Erosion (for example caused by strong easterly winds and oceanic activity) already changed the morphology significantly (HARFORD ET AL., 2002).

South Soufrière Hills and Soufrière Hills are well preserved, and the effect of erosion is not as large as in the northern part of Montserrat due to recent volcanic activity (HARFORD ET AL., 2002). Between 450-290 ka hornblende-orthopyroxene lavas erupted (HATTER ET AL., 2018). A period of mafic volcanism between ~280 and ~130 ka lead to the formation of Soufrière Hills. Subsequently, the evolution of the South Soufrière Hills took place at around 130 ka conveying magma with basaltic to basaltic andesite composition. The material was mainly deposited as lava, scoria-fall and sedimentary mass-wasting processes (HATTER ET AL., 2018). Four horseshoe shaped complexes are characteristic for the summit area and mark remnants of dome collapse (HARFORD ET AL., 2002).

Soufrière Hills is the area where the most recent volcanic eruptions occurred. In its centre the Soufrière Hills Volcano is located, a Peléean type volcano (SPARKS & YOUNG, 2002). The composition of the rocks is mainly andesitic, and the mountainous volcanic complex of Montserrat is covered by volcanoclastic deposits (HARFORD ET AL., 2002). The mineralogy changed from two-pyroxene andesite to hypersthene-hornblende andesite (HATTER ET AL., 2018). The centre of Soufrière Hills comprises four old domes (Gages Mountain, Chances Peak, Galways Mountain and Perches Mountain) surrounded by associated volcanic aprons. In the centre of this old dome complex is the English Crater with a dome formed during recent eruptions (1995-2010) and an opening in eastern direction passing into the Tar River Valley. For detailed information about the geomorphological and volcanic evolution of Montserrat and the different volcanic complexes see REA (1974), ROOBOL & SMITH (1998); HARFORD ET AL. (2002), ZELLMER ET AL. (2003), LE FRIANT ET AL. (2004), SMITH ET AL., 2007; HATTER ET AL. (2018) and references therein.

ZELLMER ET AL. (2003) summarized the petrological composition of the Silver Hills, Centre Hills and Soufrière Hills consisting predominantly of highly porphyritic (30-55 wt %) andesites to dacites with a microlite-rich groundmass and a SiO₂ content of 48 to 64 wt % (HARFORD ET AL., 2002). Mineral phases are plagioclase, oxides, orthopyroxene, ± clinopyroxene, ± hornblende, ± quartz, ± olivine (rare). Hornblende and quartz are absent in the basaltic andesites of Southern Soufrière Hills (ZELLMER ET AL., 2003).

In the early evolution phase of Soufrière Hills volcano, the tectonically uplifted areas Garibaldi Hill and St. Georges Hill are interpreted as deposits related to Centre Hill. This also includes Roches Bluff in the SE part of Soufrière Hills (LE FRIANT ET AL., 2014). The Belham Valley Fault – a volcano-tectonic structure – crosses the island of Montserrat in NW-SE direction (see Figure 2).

Offshore Montserrat large landslides have been deposited, which resulted from multiple flank collapse events of Soufrière Hills in pre-historic and recent times (DEPLUS ET AL., 2001; LE FRIANT ET AL., 2004; TROFIMOV ET AL., 2006, 2008; HATTER ET AL., 2018). Recent events since 1995 are for example the 26 December 1997 (Boxing Day) eruption with a debris avalanche reaching the sea at the mouth of White River south of Soufrière Hills Volcano or the lava dome collapse in July 2003 that produced a large pyroclastic flow that hit the sea after moving down the Tar River Valley (VOIGHT ET AL., 2002; TROFIMOV ET AL., 2008). A closer look at the bathymetry around Montserrat (see Figure 2) reveals the large shallow submarine shelf surrounding the northern part of the island. It reaches depth up to 100 meters with an average water level of 20-60 m (LE FRIANT ET AL., 2004). Within a few 100 m the shelf drops to a depth of the ocean floor to 500-600 m. LE FRIANT ET AL. (2004) suggested that the shallow shelf depth is linked to glacio-eustatic sea-level changes.

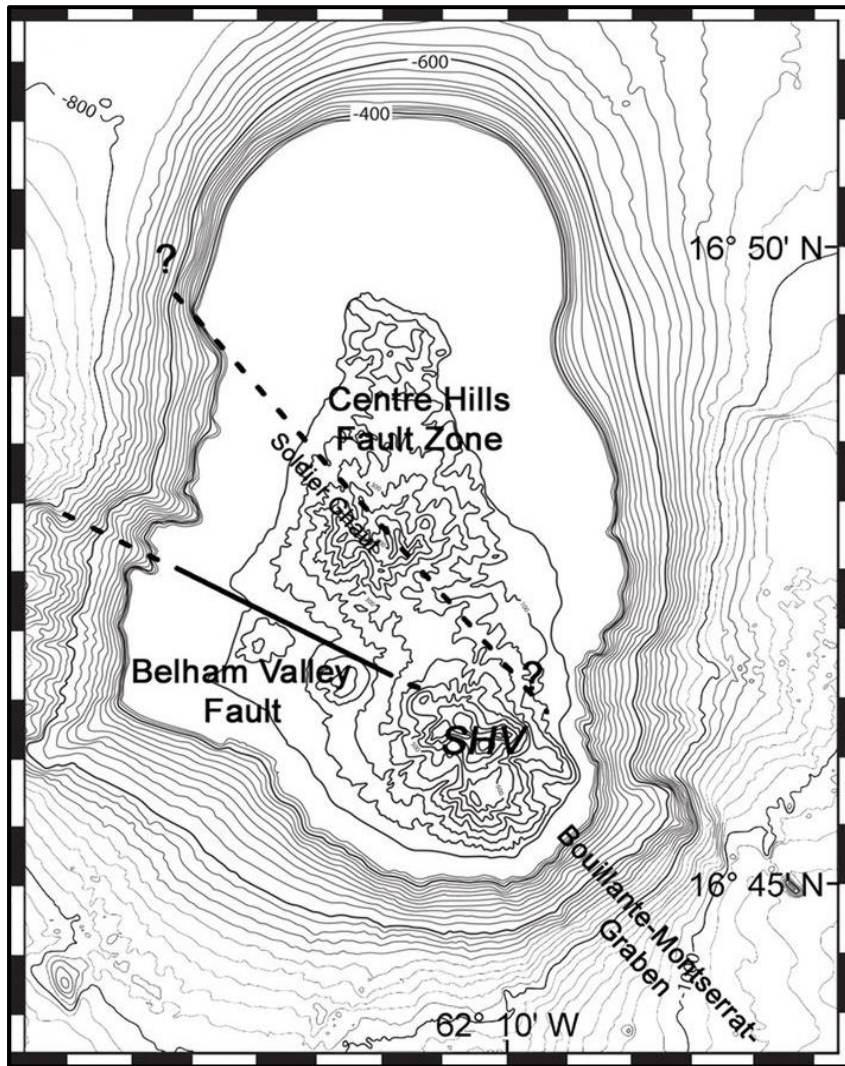


Figure 2: Bathymetric map of Montserrat and offshore regions with the Belham Valley Fault (black line) and a suggested fault trending NW-SE through Centre Hills (dashed line), after HAUTMANN ET AL. (2014).

2.3 Recent activity (1995-2013)

A considerable amount of literature has been published on the volcanic activity of Soufrière Hills volcano since it became active again in 1995 after an approximately 350-year period of quiescence (EDMONDS & HERD, 2005). Some of the most important scientific studies have been compiled in two works (DRUITT & KOKELAAR 2002, and WADGE ET AL. 2014a) that provide a detailed overview of the five eruption phases between 1995 and 2010. In addition, there are many other publications dealing with the evolution of the island (LE FRIANT ET AL., 2004; ZELLMER ET AL., 2003; HATTER ET AL., 2018), geochemistry and petrology of the extruded rocks (DEVINE ET AL., 1998; MURPHY ET AL., 2000; CHRISTOPHER ET AL., 2014; EDMONDS ET AL., 2016), subaerial and submarine mass movements caused by volcanic activity (COLE ET AL., 1998; HART ET AL., 2004; EDMONDS & HERD, 2005; TROFIMOV ET AL., 2006; TROFIMOV ET AL., 2008; KARSTENS ET AL., 2013), or vulcanian explosions and dome growth (CLARKE ET AL., 2002; STINTON ET AL., 2014; RODGERS ET AL., 2016; BURNS ET AL., 2017). Here, a brief overview is given of the recent volcanic activity of the Soufrière Hills volcano.

As mentioned before, the eruptions were divided into five phases, which were followed by times of lower activity. The phases of lava dome growth and collapses occurred from November 15th, 1995 - March 10th, 1998; November 27th, 1999 - July 28th, 2003; August 1st, 2005 - April 20th, 2007; July 28th, 2008 - January 3rd, 2009 and October 9th, 2009 - February 11th, 2010 (WADGE ET AL., 2014b).

Phase 1 began with the growth of a porphyritic andesite lava dome in November 1995 and it lasted till March 1998. Since July 1995 phreatic explosions occurred (SPARKS & YOUNG, 2002). This period is characterized by different styles of volcanic activity including phreatic explosion, lava-dome growth with dome-collapse-related pyroclastic flows, magmatic explosions, commonly with fountain-collapse-fed pyroclastic flows, sector collapse with associated explosive dome disruption and pyroclastic density current and ash-venting (KOKELAAR, 2002). Major dome collapses occurred on 25 June 1997 and 26 December (Boxing Day) 1997 (SPARKS & YOUNG, 2002). The capital Plymouth was destroyed by a large block-and-ash flow on 3 August 1997. After the large sector collapse of Galway's Wall on the SW side of English's Crater at Boxing Day 1997 18 months of volcanic quietness followed till November 1999 (WADGE ET AL., 2014b).

Phase 2 was initiated by returning dome growth and it was characterized by three large dome collapse events (20 March 2000, 29 July 2001 and 12-13 July 2003). The most intense collapse was the 12 to 13 July 2003 event that resulted in $200 \times 10^6 \text{ m}^3$ of material running down the slope and reacting explosively with seawater. This triggered a base surge that moved inland (EDMONDS & HERD, 2005). Large amounts of volcanic material ended in the sea as pyroclastic flow deposits. The second period was also the longest time of near-continuous lava extrusion which continued for almost 3.5 years followed by one year of very low residual activity (WADGE ET AL., 2014b).

Phase 3 lasted from August 2005 till April 2007 and began with another dome growth phase with the major collapse on 20 May 2006 (WADGE ET AL., 2014b). LOUGHLIN ET AL. (2010) suggested that the event was caused by a high amount of ascending magma coupled with heavy rainfalls (WADGE ET AL., 2014b). Compared to phase 1 and phase 2 explosion events were rare, except the major collapse in May 2006, but the magma output was comparable to the one of the first phase (WADGE ET AL., 2014b).

Phase 4 started with a seismic crisis and a coupled explosion on 29 July 2008 (WADGE ET AL., 2014b). The high explosivity was a characteristic feature of phase 4 and differed significantly from the first three phases. The sub-daily cyclicity and the average intrusion rate increased towards the end (WADGE ET AL., 2014b). Some pyroclastic flows were produced during this period but no significant ashfalls have been recorded (BAXTER ET AL., 2014).

Nine months of quiescence followed till *phase 5* began on 9 October 2009. This short period was characterized by high extrusion and explosivity rates accompanied by ash venting, dome growth and block-and-ash flows, which culminated in a large partial dome collapse on 11 February 2010 (BURNS ET AL., 2017). It was the largest event on the northern side of the volcano and produced a horseshoe-shaped crater opened in northern direction (WADGE ET AL., 2014b). The ascending plume reached a height of 15 km. After the large intense dome collapse event activity is limited to seismic activity, ash venting and active fumaroles (WADGE ET AL., 2014b).

The samples analyzed in this thesis can be assigned to different phases. On the one hand, the ashfall samples were collected during phase 1. The offshore samples mostly contain material from the dome collapse in July 2003 (Phase 2) and the samples from Belham Valley, Plymouth, Trant's and Spanish Point can be associated with material from the volcanic activity of each of the five phases.

2.4 Lava dome eruptions and the transition of pyroclastic flows

This chapter deals with a general overview of Vulcanian eruptions. It also examines the processes that occur when a dome collapses and, as a consequence, a pyroclastic flow is generated that eventually (in the case of Montserrat) reaches the sea. The processes involved are explained and associated accordingly.

2.4.1 Vulcanian eruptions

Vulcanian eruptions are short-lived explosive eruptions that cover a wide range of fragmentation and distribution area (SELF ET AL., 1979; CLARKE ET AL., 2015; RODGERS ET AL., 2016). Historically, Vulcanian explosions are based on the eruptions of Fossa on Vulcano, Aeolian Islands, Italy (HEIKEN & WOHLLETZ, 1985). CLARKE ET AL. (2015) collected the most important attributes: short eruptions (< 120 sec.), relatively small magnitude (VEI 3-4), relatively fine ejecta, low-vesicularity pyroclasts but variable clast vesicularity, blocky shape of ash particles and strong ballistic ejections. Furthermore, they often culminate in sub-Plinian or Plinian eruptions and they are accompanied by a shock wave (CLARKE ET AL., 2015). Vulcanian eruptions are often related to andesitic-dacitic magmas and are associated with long-lived dome growth eruptions (RODGERS ET AL., 2016). A dome growth period comprises phases of quiescence, effusive and explosive modes. Thereby, the latter culminates often in dome collapse events (RODGERS ET AL., 2016).

Figure 3 depicts a sequence of a typical Vulcanian eruption on Montserrat in 1997. The explosion is initiated by the ejection of ash and debris (DRUITT ET AL., 2002). This is followed by shot-like sounds, a rising plume and ballistics that were ejected up to 1.7 km from the vent. As the jets reach their maximum height they collapse and fall down to the ground to generate pyroclastic flows and surges

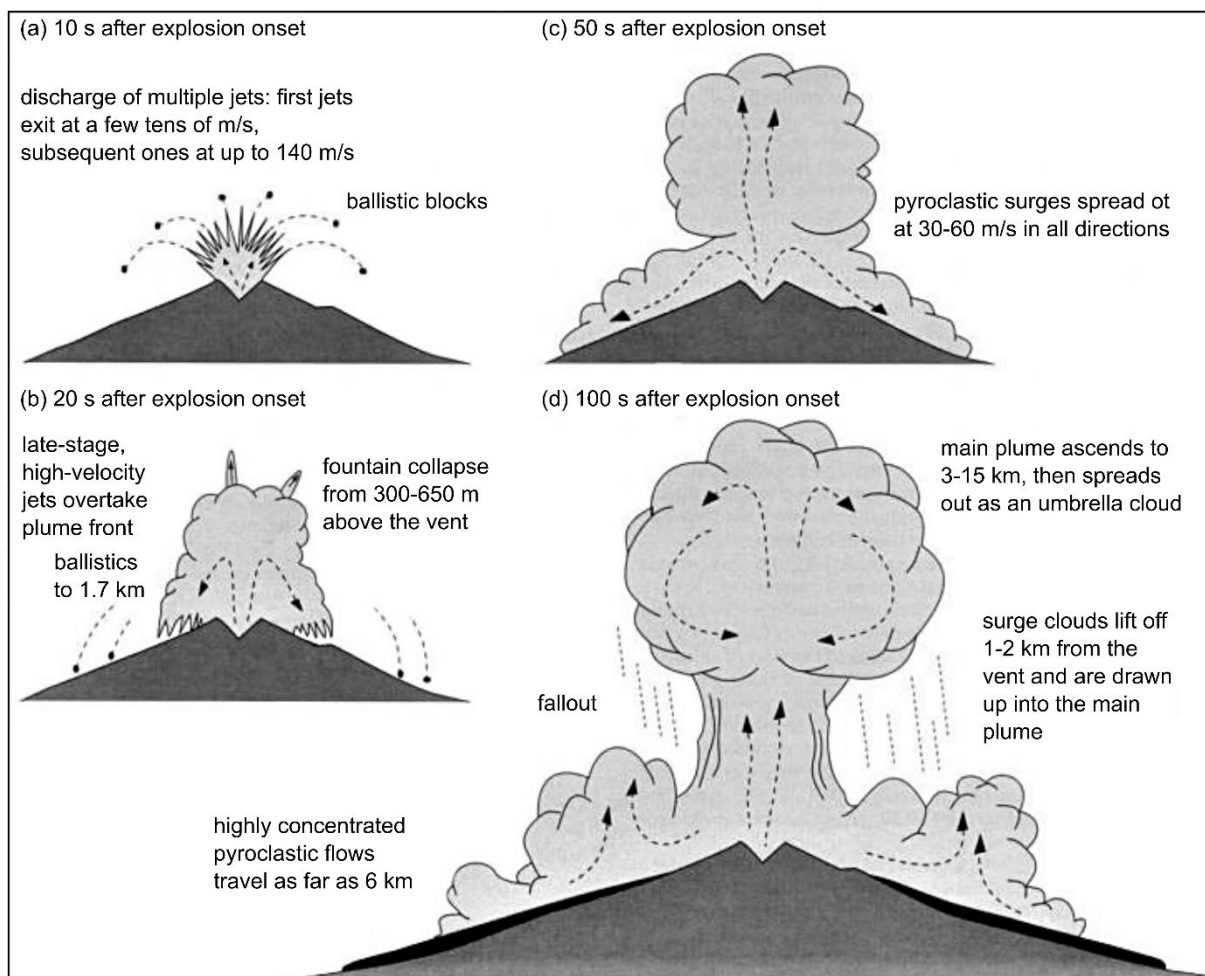


Figure 3: Typical sequence of a Vulcanian eruption in 1997 at Soufrière Hills on Montserrat adopted from DRUITT ET AL. (2002).

that move downwards with 30-60 m/s in all directions. The umbrella-like plume ascends to 3-15 km and the column collapse lead to highly concentrated pyroclastic flows (DRUITT ET AL., 2002).

2.4.2 Pyroclastic flows and interaction with sea water

According to SMITH (1960) and SPARKS ET AL. (1980) a pyroclastic flow is a hot, highly-concentrated debris or mass flow commonly denser than water. Nevertheless, the density of the hot particle-gas composite can differ considerably. SPARKS ET AL. (1980) suggests that the transport of pyroclastic flows on land is facilitated by the exsolution of gases. However, as soon as a pyroclastic flow encounters water, the reverse situation sets in and the exerted pressure prevents the gas release (SPARKS ET AL., 1980). Flows denser than water can provide a more or less smooth entrance of the pyroclastic flow into the water (SPARKS ET AL., 1980; TROFIMOV ET AL., 2008). COLE & DECELLES (1991) stated some remarkable differences between submarine and subaerial pyroclastic flow deposits. Submarine deposits, for example, show perlitic cracks in nonvesicular, juvenile grains and pumice and shattered crystals occur as well as steam vesicles within the groundmass. In general, pumice segregation toward the top of the beds takes place (TROFIMOV ET AL., 2008). They suggest that these characteristics are a result of quench fragmentation of the hot material that is mixed with the seawater when a pyroclastic flow enters the sea (TROFIMOV ET AL., 2008).

A schematic profile from the volcano to the sea is shown in Figure 4. The eruption mechanism involved is a Vulcanian explosion after dome growth like it is typical for Montserrat. After reaching the highest point of ascent the plume collapses and generates pyroclastic flows running down the slopes to the

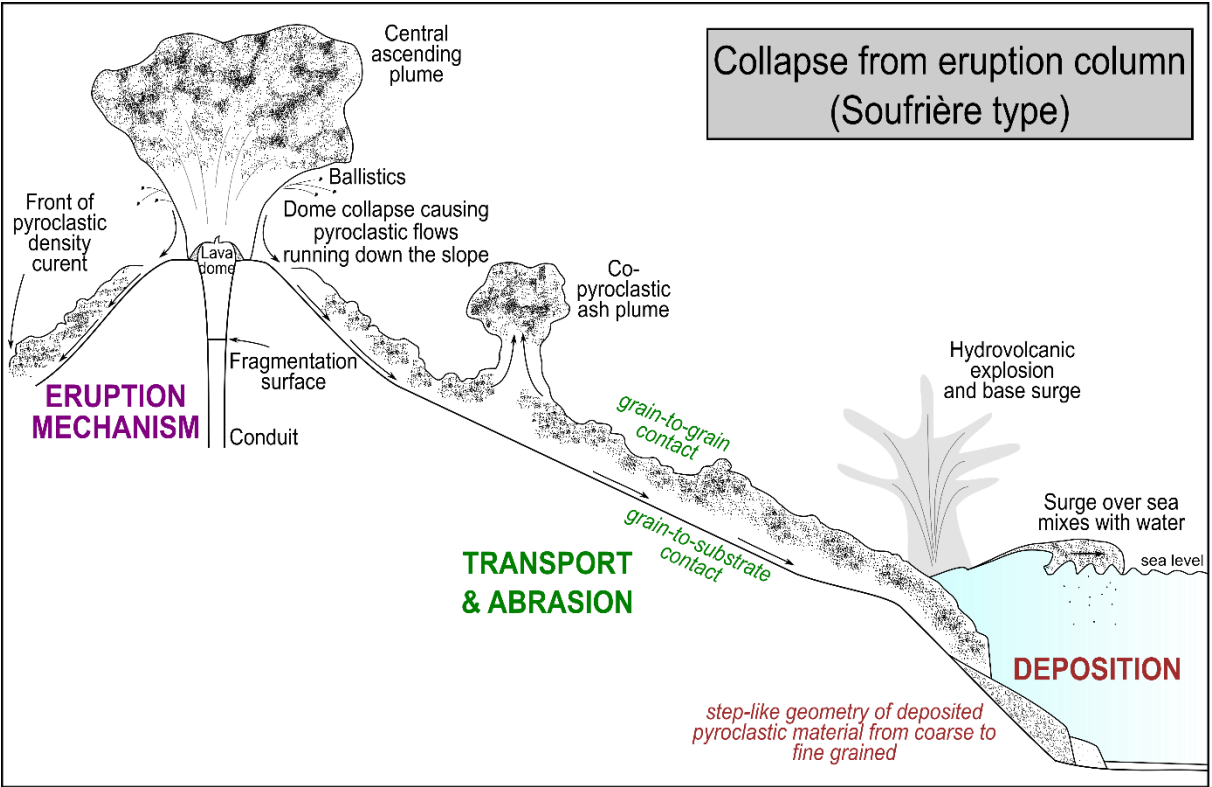


Figure 4: Schematic profile shows a typical Soufrière type Vulcanian eruption on Montserrat characterized by the collapse from the eruption column. The ejected material moves downhill as surges and block-and-ash flows towards the sea to be deposited there. Various processes influence the shape and morphology of the pyroclastic material, such as eruption mechanisms, transport, and deposition both offshore and onshore, compiled from and modified after CLARKE ET AL. (2002), FRANCIS & OPPENHEIMER (2004), EDMONDS & HERD (2005) and TROFIMOV ET AL. (2008).

sea (Soufrière type; FRANCIS & OPPENHEIMER, 2004). During transport of the hot pyroclastic material, abrasion and breakage of the particles occur through grain-to-substrate and grain-to-grain contacts. Interaction with seawater leads to phreatic explosions at the contact zone when the tephra temperature is higher than 200 °C; it may result in base surges expanding semi-radially away from the source (FREUNDT, 2003; EDMONDS & HERD, 2005; TROFIMOV ET AL., 2008). The pyroclastic flow can transform into a cool, water supported gravity flow evolving into turbidity currents (TROFIMOV ET AL., 2008). During transport as a turbidity current the material is being sorted and physically differentiated as it is typical for water-laden submarine mass flows and a step-like deposit geometry developed (TROFIMOV ET AL., 2008). First, coarse pyroclastic material was deposited with steep slopes. In front of the coarse material massive sand deposits are following that are intersected by gravel and silt. Finally, very fine and widespread sand and ash deposits form the turbidity currents (TROFIMOV ET AL., 2008)

2.5 Granulometry and microtextures – Previous studies

Research on sediment grains using SEM analysis began in the early 1960s. Since then, numerous scientists have used SEM to study and interpret the surfaces of the particles (mainly quartz). Thereby, they considered the shape of the grain as well as the microtextures which are located on the grain surface. In addition, they have analysed various formation conditions and influences that have led to mechanical or chemical changes on the grain surfaces and associated the sediments with certain environments (BIEDERMAN, 1962; KRINSLEY & TAKAHASHI, 1962 a,b,c; PORTER, 1962; KRINSLEY & FUNNELL, 1965; SOUTENDAM, 1967; KRINSLEY & DONAHUE, 1968; MARGOLIS, 1968; MARGOLIS & KRINSLEY, 1971; SETLOW & KARPOVICH, 1972; KRINSLEY & DOORNKAMP, 1973; WHALLEY & KRINSLEY, 1974; LE RIBAUT, 1977; HIGGS, 1979; MAHANEY & KALM, 2000; MAHANEY ET AL., 2001; MAHANEY, 2002; VOS ET AL., 2014). Hereby the focus was concentrated on quartz, due to its weather resistance and only a few studies referred to grains of heavy minerals (SETLOW & KARPOVICH, 1972; MAHANEY, 2002; MORAL CARDONA, 2005). The most important studies that name and describe different microtextures of quartz grains are the standard atlases of KRINSLEY & DOORNKAMP (1973), LE RIBAUT (1977) and MAHANEY (2002). Since these studies deal predominantly with microtextures of quartz grains, only individual sources (MAHANEY, 2002; VOS ET AL., 2014) and their terms for the morphological properties are used for this study.

The specimens analysed are pyroclastic deposits of the active Soufrière Hills volcano in Montserrat. The Soufrière Hills volcano is characterized by dome growth and collapse and the associated mass movements of the ejected material down the steep slopes. A remarkable aspect is the explosive interaction of the pyroclastic flows and surges with sea water and the subsequent deposition on the seafloor. Throughout these processes, the particles are affected by a variety of factors that can significantly modify the morphology and texture of the grain surface. Some fundamental studies dealing with textural surface features of pyroclasts were published by WOHLETZ (1983), HEIKEN & WOHLETZ (1985) and MARSHALL (1987). HEIKEN & WOHLETZ (1985) dealt with the description of surface textures and the characterization of volcanic ashes in general and MARSHALL (1987) published a book on the shape analysis of sedimentary and volcanic clasts. Table 1 demonstrates morphological and structural characteristics according to WOHLETZ (1983). In this study, surface structures were analysed seen on pyroclasts generated by hydrovolcanic eruptions. WOHLETZ (1983) described the increasing number of vesicles and broken, planar surfaces. Furthermore, the grains experience a higher abrasion in the course of movement, as the medium in which the particles are transported densifies. Other studies dealing with microtextures on pyroclasts caused by different eruption mechanisms are HEIKEN

(1972), WALKER & CROASDALE (1972), SHERIDAN & WOHLTZ (1983), and CIONI ET AL. (1992). Related to the activities at Soufrière Hills in the mid-90s, BONADONNA (2002) described fallout tephra generated by magmatic explosive eruptions, dome-collapse pyroclastic flows and rockfalls, ash-venting and phreatic explosions. Furthermore, the study contains a characterization of the morphology of the fallout tephra with associated pictures of the surface textures.

Table 1: Classification of the morphology and texture of pyroclasts from hydrovolcanic eruptions after WOHLTZ (1983).

Eruptive Mechanism (Grain Shape)	Transport (Edge Modification)	Alteration (Palagonitization)
Blocky, curvi-planar surfaces	Grain rounding	Vesicle fillings
Vesicularity	Grooves and scratches	Skin cracks
Droplike or fused skin	Steplike fractures	Solution and precipitation
Deformation planes	Dish-shaped fractures	Microcrystalline encrustation
Adhering particles	Chipped edges	
Platy	Cracks	
Mosslike	Upturned plated	
	V-shape depressions	

3. MATERIAL AND METHODS

This chapter deals with the samples and the applied methods used for this project. On 18 samples, grain size analysis, reflected-light microscopy, polarising microscopy, and SEM were accomplished. In addition, a grain shape analysis and point counting on strewn slides were carried out to better describe and quantify the samples.

3.1 Samples

Eighteen samples from different environments were available for this study. A list with the samples and their location is provided in Table 2; their location is illustrated on a map in Figure 5. Seven specimens have been supplied by Prof. S. Sparks from the University of Bristol. These are mainly fallout tephra's from vulcanian explosions or co-flow ashes from dome collapses in September to October 1997. Thereby, trays were placed around the volcano to collect the ashes since the high intensity impeded manual collection (BONADONNA ET AL., 2002). Another nine samples were provided by Dr. A. Stinton and the staff of the MVO. They were collected in coastal areas of the Belham Valley (BV), Plymouth (Plym), Trant's and Spanish Point. The material reached the sea as pyroclastic flows, block-and-ash flows, or surges and it was influenced by different repositioning processes. Two samples comprise reworked offshore deposits provided by the BOSCORF; the formation of these offshore deposits was related to the andesite lava dome collapse on 12 to 13 July 2003 and the associated

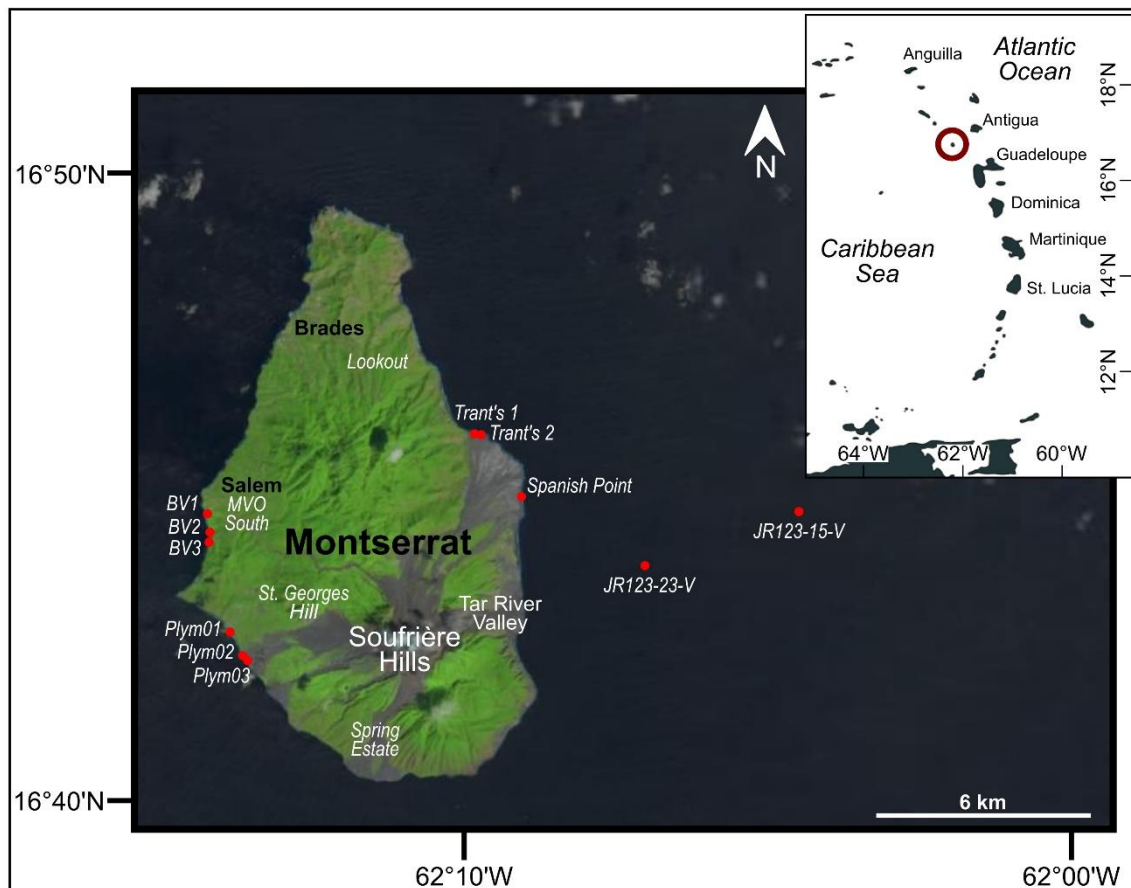


Figure 5: Location map of the analysed samples (red points) with an overview of the Lesser Antilles island arc. Some samples have no coordinates, they are described by location names (Lookout, MVO South, St. Georges Hill, Spring Estate).

pyroclastic flows that reached the sea. The samples JR123-15-V and JR123-23-V (see Figure 6) were taken in 2005 during a research voyage of the RRS James Clark Ross at depths of 683 m and 939 m off the east coast of Montserrat using a Vibrocore System developed by the British Geological Survey (TROFIMOVS ET AL., 2008). They are part of a set of 52 samples that were taken along the longitudinal flow axis of the deposits from July 2003 dome collapse. Vibrocore JR123-23-V is the only sample that was taken from the pyroclastic lobe due to large lava blocks that made coring impossible. The sample JR123-15-V, on the other hand, originates from the elutriated fines of a dense, granular sediment density current (TROFIMOVS ET AL., 2008). The profiles of both Vibrocores can be seen in Appendix 1.

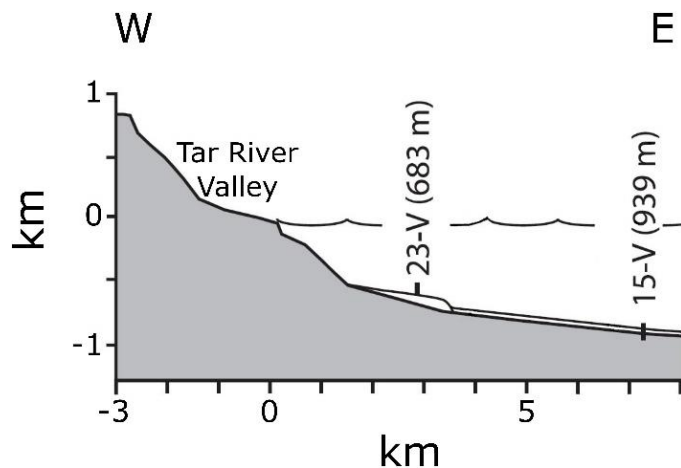


Figure 6: Detail of the topographic W-E profile of Montserrat from Soufrière Hills Volcano peak down to the Tar River Valley and the area offshore with the water depth of the samples JR123-15-V and JR123-23-V (modified after TROFIMOVS ET AL., 2008).

Table 2: Source type and setting of the samples provided by BOSCORF (JR123-15-V and JR123-15-V), S. Sparks (MVO290, MVO1700, MVO1701, MVO1702, MVO1703, MVO1704 and MVO1705) and A. Stinton (BV1, BV2, BV3, Plym01, Plym02, Plym03, Trant's 1, Trant's 2 and Spanish Point).

Sample	Source	Setting	Type of deposition*	Grid Reference (WGS84 Zone 20Q)
JR123-15-V	Piston coring – offshore samples (sampling in 2005)	Offshore	1	-
JR123-23-V		Offshore	1	-
MVO1701	Vulcanian explosion ashfall deposit (sampling in Sept-Oct 1997)	Onshore – MVO South	2	-
MVO1702		Onshore – Lookout	2	-
MVO1703		Onshore – Lookout	2	-
MVO1700	Co-pyroclastic flow ashfall deposit (sampling in Sept 1997 and MVO1704 is from Boxing Day pdc → Dec ²⁷ 1997)	Onshore – St. Georges Hill	2	-
MVO1704		Onshore – Spring estate	2	-
MVO1705		Onshore – MVO South	2	-
MVO290		Onshore – St. Georges Hill (solar panel site)	2	-
BV1	Influenced by any event (pyroclastic flow or Lahar activity) from 1995 until sampling day	Onshore – Belham Valley	1	581685 1851431
BV2		Onshore – Belham Valley	1	581800 1850921
BV3		Onshore – Belham Valley	1	581762 1850594
Plym01		Onshore – Plymouth	1	582805 1847235
Plym02		Onshore – Plymouth	1	583040 1846912
Plym03		Onshore – Plymouth	1	583178 1846776
Trant's 1	Related to large partial dome collapse (11.02.2010) → created a large area of new coast	Onshore – Trant's	1	589513 1853711
Trant's 2		Onshore – Trant's	1	589448 1853754
Spanish Point		Onshore – Trant's	1	590774 1851883

* 1 – reworked deposit, 2 – primary deposit

3.2 Laboratory analysis

For each of the 18 samples, wet sieving and grain size analysis has been carried out, the results of which has been interpreted with the programs *GRADISTAT* and *Microsoft Excel*. The granulometric analysis is a standardized procedure treating all samples without special consideration.

The grain size fractions 200-250 μm and 250-500 μm were selected to choose individual grains and examine them under the SEM for surface microtextures. After sample splitting, thin sections of the particle size fractions 250-500 μm were produced to get an overview of the composition of the samples. The individual methods are briefly introduced below, and the preparation of the samples is described shortly.

3.2.1 Sieving

Before sieving, all samples were tested for their salinity in water to guarantee that no salt crusts impair the following analyses. This was done with a digital conductivity meter *GMH 3430* of the *Greisinger electronic GmbH*. Furthermore, the samples were placed in a beaker and treated in an ultrasonic bath to disintegrate particles sticking together. Afterwards the samples were dried at 60°C in an oven and then weighed out with an analytical *Mettler Toledo* scale (*AB204*). Each sample was carefully wet sieved by hand to avoid artificial grain damage. The sieve set consisted of the following fractions: 2 mm, 1mm, 630 μm , 500 μm , 250 μm , 200 μm , 125 μm , 100 μm , 63 μm (DIN 4188 and ISO 3310/1). These were selected since they correspond to a standard sieve set. After sieving, the various fractions were accurately weighed to four decimals. The mass percentages of the grain size fractions were plotted, and particle-size distribution curves drawn. Programs used for the interpretation of the data were *GRADISTAT* and *Microsoft Excel*.

3.2.2 Grain size analysis

After sieving the samples, statistic parameters (mean, median, sorting, skewness, kurtosis) were calculated. The classification of the grain sizes was adopted by BLOTT & PYE (2001), following the studies of UDDEN (1914), WENTWORTH (1922) and FRIEDMAN & SANDERS (1978).

A logarithmic scale is used to represent the grain sizes to ensure that the large and small grains are not over- or underemphasized (TUCKER, 1996). In this study the logarithmic Udden-Wentworth grade scale, which is based on a logarithmic classification to base 2, was used for calculating the statistic parameters. Since the sieve fractions do not completely correspond to the Phi scale, the values had to be converted from metric data in integers using the following equation after KRUMBEIN (1934):

$$\phi = -\log_2 d, \quad (1)$$

with d being the grain diameter in millimetres (TUCKER, 1996; BLOTT & PYE, 2001). The 'log-normal' scale can now be used to calculate statistical parameters for a more detailed examination of the samples (TUCKER, 1996). Different mathematical or graphical methods can be used for the evaluation. The most precise is the mathematical 'method of moments' after KRUMBEIN & PETTIJOHN (1938) since it applies the complete population. Nevertheless, the distribution of a sample should be completely known, because outliers can highly affect the statistics of a population (BLOTT & PYE, 2001). The graphical method after FOLK & WARD (1957) neglects the outliers and is therefore better applicable for open-ended distributions (BLOTT & PYE, 2001). The author of this study is aware of effects on these parameters (mean and sorting) due to density variation of the volcanic material (SMITH & SMITH, 1985).

Median and mean represent the average size of the grains, whereas the median is derived from the 50%-mark of the cumulative curve and the mean is calculated from three values, which are sufficient to generate a reliable average (TUCKER, 1996). Sorting and skewness describe the spread of the sizes around the average and the symmetry to the right or the left side of the average (BLOTT & PYE, 2001). The concentration level of the grains in relation to the average is called kurtosis (BLOTT & PYE, 2001). The statistic parameters were calculated after FOLK & WARD (1957):

$$\text{Median} \quad Md = \phi_{50} \quad (2)$$

$$\text{Mean} \quad M_z = \frac{\phi_{16} + \phi_{50} + \phi_{84}}{3} \quad (3)$$

$$\text{Sorting} \quad \sigma_1 = \frac{\phi_{84} - \phi_{16}}{4} + \frac{\phi_{95} - \phi_5}{6,6} \quad (4)$$

$$\text{Skewness} \quad SK_1 = \frac{\phi_{16} + \phi_{84} + 2\phi_{50}}{2(\phi_{84} - \phi_{16})} + \frac{\phi_5 + \phi_{95} - 2\phi_{50}}{2(\phi_{95} - \phi_5)} \quad (5)$$

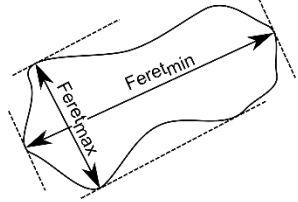
$$\text{Kurtosis} \quad K_G = \frac{\phi_{95} - \phi_5}{2.44(\phi_{75} - \phi_{25})} \quad (6)$$

The classification according to Folk & Ward (1957) can be found in Appendix 2.

3.2.3 Grain Shape Analysis

In addition to the calculation of the statistical parameters above, parameters of the grain shape, including area, perimeter, ferret diameter, aspect ratio, compactness and circularity of a particle, were also considered. The shape descriptors (Table 3) were calculated after DIN ISO 9276-6.

Table 3: Selected grain shape descriptors after DIN ISO 9276-6.

Symbol	Description	Equation
A	Area of the particle	
P	Perimeter of the particle	
$Feret_{max}, Feret_{min}$	Distance between two parallel tangents: → $Feret_{max}$ – maximal diameter; particle length → $Feret_{min}$ – minimal diameter; particle breadth	
<i>Aspect ratio</i>	Ratio of $Feret_{min}$ diameter to $Feret_{max}$ diameter	$\frac{Feret_{min}}{Feret_{max}} \quad (7)$
<i>Compactness</i>	Degree of similarity between the particle (or its projection surface) and a circle, considering the overall shape of the particle <i>Roundness</i> : square of compactness	$\sqrt{\frac{4 \cdot A}{\pi \cdot Feret_{max}^2}} \quad (8)$
<i>Circularity C</i>	Degree of similarity between the particle (or its projection surface) and a circle, considering the smoothness of its perimeter (term below the root is the so-called <i>form factor</i>)	$\sqrt{\frac{4 \cdot \pi \cdot A}{P^2}} \quad (9)$

A method to display the grain shape of the particles is based on the roundness of POWERS (1953; see Appendix 3). He distinguished between six roundness classes with an interval of 1.00 to 0.12. These are well rounded (1.00-0.70), rounded (0.70-0.49), subrounded (0.49-0.35), subangular (0.35-0.25), angular (0.25-0.17) and very angular (0.17-0.12). This was chosen because smaller values were hardly observed in sediments, only crystals can have a lower value. The calculated grain shape parameters of each sample are given in the electronic appendix.

3.2.4 Sample preparation

After sieving, grain size analysis and quartering of specimens by a sample splitter a part of the grain fraction 250 - 500 μm was used to prepare strewn slides (thin sections) in the preparation laboratory of the TU Freiberg, which were later examined for their composition with the polarisation microscope and the SEM. The strewn slides of the second series of samples (from the MVO) were prepared with blue epoxy resin in order to display vesicles in the individual particles.

The major objective was to pick out individual grains (50-70 per sample) for more detailed observation under the SEM. Particles of the grain fractions 200 - 250 μm and 250 - 500 μm were selected to document microtextures on the grain surfaces. The selection consists of single crystals on the one hand and lava fragments on the other hand. However, it should be mentioned that mainly crystals were selected to identify microtextures on the surfaces. The lava fragments were selected to provide information about the grain shape. Afterwards, the grains were glued to a mount and carbon coated.

3.3 Microscopic examination methods

A SEM was used to display microtextures on the grain surfaces. For this purpose, approximately 50 grains, mainly crystals with a smooth surface, of the fractions 200-250 μm and 250-500 μm were selected from each sample with a stereomicroscope. To round off the investigations on the volcanic grains, the strewn slides were analysed with a transmitted-light microscope and a point counting procedure.

3.3.1 Optical Microscopy

A stereomicroscope *Motic SMZ-168 SERIES* of the Sedimentological Laboratory was used to receive an initial overview of the composition of the samples and to select suitable grains for scanning electron microscopy. Care was taken to examine individual crystals of different minerals, since those had an appropriate surface to identify specific microtextures. Rock fragments and glomerophytic mineral structures were selected to get an impression of the grain shape, as the surfaces were not appropriate for the investigation of microtextures.

In addition, the strewn slides were examined with a polarisation microscope *Axiolab A* from Carl Zeiss in the CVT (Centre of Volcanic Textures) of the Geological Institute to get an insight into the petrographic composition of the samples. To display any special features, images were taken with the camera *AxioCamERc 5s*.

Nevertheless, each sample was quantified by point counting (within the grains) with the free software *JMicroVision 1.2.7* and categorized into groups. This method is intended to give a general overview of the component frequency. The selected groups are the mineral phases plagioclase, amphibole,

pyroxene, the opaque phase and accessory minerals as well as rock fragments and biogenic fragments. All juvenile lava fragments, glomerophytic and andesitic clasts were summarized to the group rock fragments. The phenocrysts (e.g. plagioclase and amphibole) are part of the group rock fragments and not included in the individual mineral phase's plagioclase and amphibole to which only single crystals were counted.

3.3.2 Scanning Electron Microscopy (SEM)

As major part of this master thesis, SE images of the single grains, mainly crystals with a smooth surface, were taken using the *JEOL JSM-7001F* SEM at the Institute of Geology (Figure 7). However, rock fragments and rugged particles were also selected to cover a broad spectrum of surface microtextures. In addition, detailed pictures of single grains were taken to better distinguish and describe the microtextures.

SEM is used for high resolution imaging and enlargement of three-dimensional bodies and two-dimensional objects. The electron beam scans the entire sample and the result is a strongly enlarged image of the scanned object (NIEDERAUER & SCHÄFER, 1985). Secondary electrons are emitted when electrons are discharged from the sample by the impacting electron beam. This process is very low-energetic and generates only a few SE. However, if the beam is refracted at one edge, more SE can be observed by the detectors and the generated image develops a very specific depth of field. Therefore, three-dimensional objects appear particularly lively. (NIEDERAUER & SCHÄFER, 1985).

With the EDX-system *Bruker Esprit 1.9.3* of the Geological Institute selected grains were examined for their element contents to identify the associated mineral name.

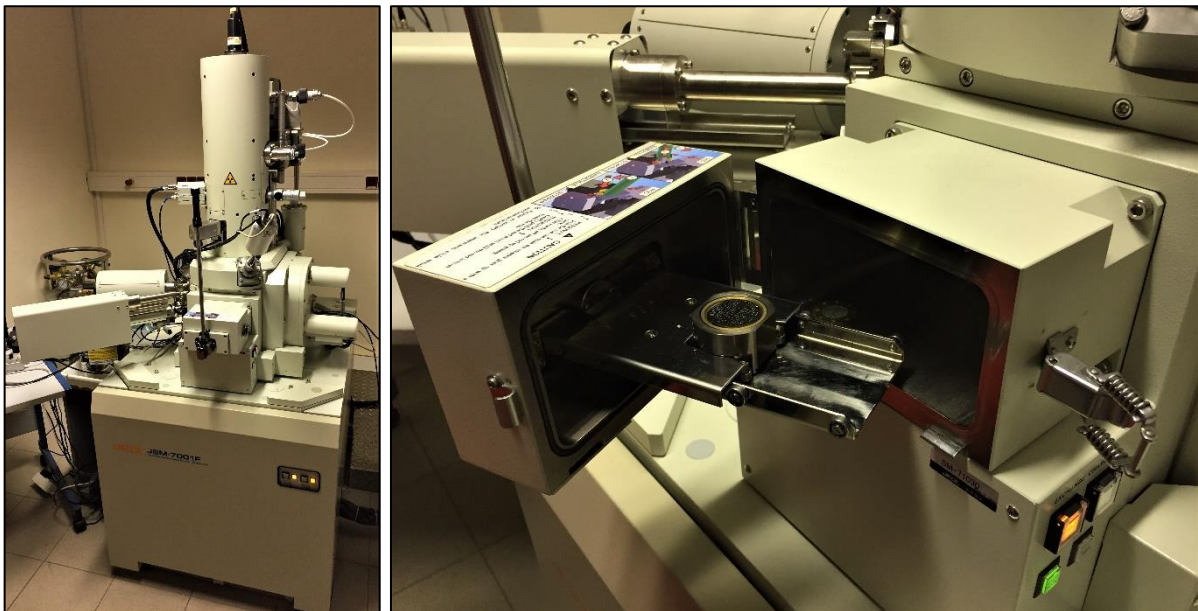


Figure 7: Scanning electron microscope *JEOL JSM-7001F* at the Institute of Geology in Freiberg (left). The right image shows the opened sample chamber with carbon coated mount.

4. RESULTS

This section presents the results of the analysed samples, which are described below concerning special characteristics and features. First, the grain size analysis is evaluated, followed by the examination of the thin sections. Also included are the results of point counting and grain shape analysis. Finally, the microtextures found on selected grains are described in detail.

4.1 Grain size analysis and statistic parameters

After sieving the samples, a particle size analysis of each sample was accomplished with the *GRADISTAT* software and *MS Excel*. Not only the particle size distribution was determined, but also the individual statistical parameters (mean value, sorting, skewness and kurtosis) were calculated. In Figure 8, the particle size distributions of individual samples are summarized as histograms. Note that very coarse, coarse and medium silt were summarized to one group. The individual cumulative frequency curves are given in the Appendix 4 and a summary of the statistical parameters is given in Table 4.

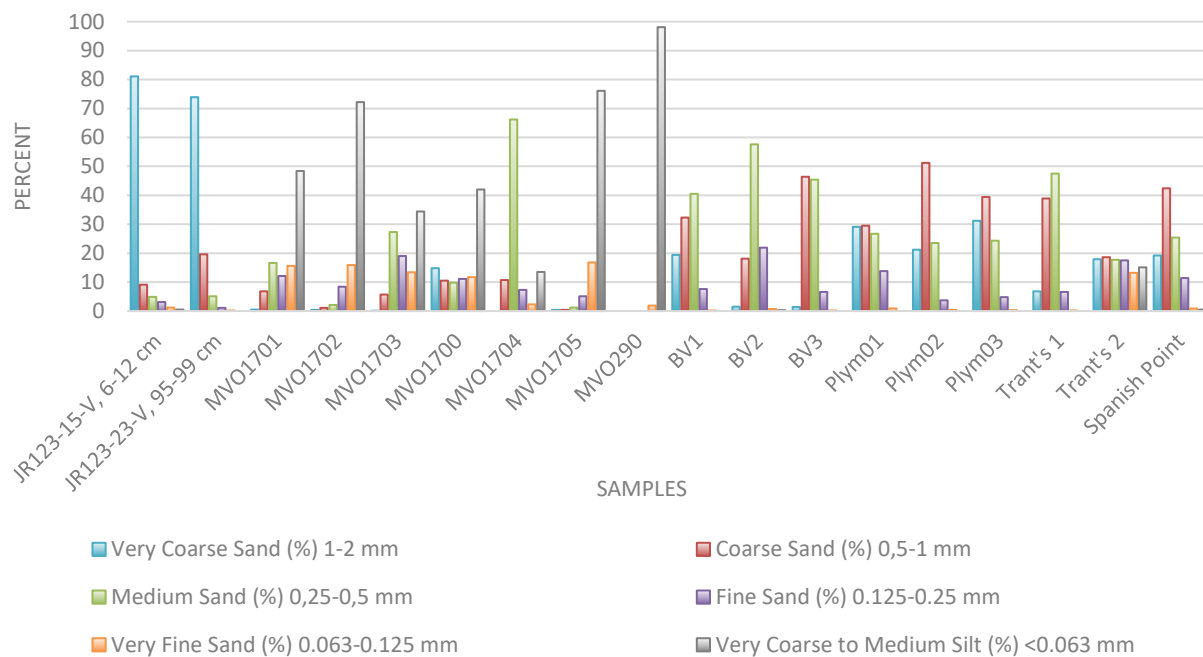


Figure 8: Comparison of grain size frequency histograms of the analysed samples; the classification of the grain sizes was adopted from BLOTT & PYE (2001).

From the data in Figure 8 and Table 4 we can see that mean and sorting of all samples vary significantly. The offshore samples JR123-15-V and JR123-23-V consist mainly of very coarse sand and they show a good sorting. The ashfall deposits (MVO290, MVO1700 - MVO1705) are composed of coarse silt up to medium sand and are poorly sorted. In turn, the samples BV1, BV2, BV3, Plym02, Plym03 and Trant's 1 are moderate to moderately well sorted and they comprise medium to coarse sand. Lastly, the samples Plym01, Trant's 2 and Spanish Point are poor to very poorly sorted.

Furthermore, the distribution types and the results of the statistical parameter calculations derived from *GRADISTAT* software are summarized in Table 4. With a few exceptions (four samples are bimodal, trimodal, or polymodal; 22%), most of the samples are unimodal (14 out of 18; 78%), whereby the highest variability is obtained in the ash fall deposits.

Table 4: Distribution type and statistics summary (values of Φ) after FOLK & WARD (1957) calculated by GRADISTAT. The classification of Folk & Ward (1957) can be seen in Appendix 2. The color code is used in the following figures and tables.

Sample	Distribution type	Mean (M_z) in Φ	Sorting (σ_1) in Φ	Skewness (Sk_1)	Kurtosis (K_G)
JR123-15-V, 6-12 cm	unimodal	-0.229	0.448	2.269	-17.464
JR123-23-V, 95-99 cm	unimodal	-0.237	0.417	2.052	0.937
MVO1701	unimodal	4.712	1.339	-0.163	0.914
MVO1702	trimodal	3.209	1.820	0.279	0.722
MVO1703	unimodal	1.866	1.196	0.560	2.635
MVO1700	bimodal	3.728	1.902	-0.113	0.711
MVO1704	unimodal	4.859	1.207	-0.121	0.904
MVO1705	unimodal	5.296	0.826	0.000	0.738
MVO290	polymodal	2.991	2.472	-0.130	0.721
BV1	unimodal	0.841	0.982	-0.198	0.936
BV2	unimodal	1.530	0.650	0.006	0.111
BV3	unimodal	1.113	0.629	0.111	0.926
Plym01	unimodal	0.708	1.144	0.010	0.781
Plym02	unimodal	0.609	0.860	0.010	1.100
Plym03	unimodal	0.489	0.988	0.001	0.870
Trant's 1	unimodal	1.077	0.730	-0.840	1.029
Trant's 2	bimodal	1.840	2.032	0.125	0.991
Spanish Point	unimodal	0.807	1.035	0.080	1.005

The distribution of grain sizes covers a wide range from very finely to coarsely skewed, with 39% (7 out of 18) showing a symmetrical distribution around the mean grain size. Nearly all samples show a platycurtic to mesocurtic-shaped curve, indicating that the tails of the curves are better sorted than the central part. Table 5 provides an overview of the statistical parameters and their sample counts.

Table 5: Summary statistics of the grain size data

Mean	Sample count	Sorting	Sample count	Skewness	Sample count	Distribution	Sample count
coarse silt	1	very poorly sorted	2	coarse skewed	5	very leptokurtic	1
very coarse silt	2	poorly sorted	7	symmetrical	7	leptokurtic	0
very fine sand	2	moderately sorted	5	fine skewed	3	mesokurtic	10
fine sand	1	moderately well sorted	2	very fine skewed	3	platykurtic	6
medium sand	5	well sorted	2			very platykurtic	1
coarse sand	5						
very coarse sand	2						

Figure 9 depicts a plot with median diameters versus sorting coefficients of all 18 analysed samples. The offshore samples JR123-15-V and JR123-23-V (blue) show the best sorting for the largest grain sizes, as can be expected from the extended distance of transportation. Furthermore, the Belham Valley and Plymouth samples (yellow) are mainly moderately sorted and are tending to be better sorted with smaller grain sizes. However, no tendency is visible for the Vulcanian explosion ashfall

deposits (red). As already mentioned, they are well dispersed from medium sand to very coarse silt and poorly sorted. The best trend is represented by the co-pyroclastic ashfall deposits (green), resulting in a significantly better grading with smaller grain size. For the samples from Trant's and Spanish Point (grey), one sample is very much out of line (Trant's 2), which was probably sampled from a block-and-ash flow deposit unlike the other two samples.

WALKER (1971) distinguished between two different pyroclastic deposits (pyroclastic fall and flow) based on a mean(Φ)/sorting (Φ) plot, whereby the overlapping area is defined by rain-washed deposits (see Figure 9). Only the vulcanian ashfall (red) and co-pyroclastic ashfall (green) deposits are plotted in the relevant area of the pyroclastic fall deposits. The remaining samples, which are mainly flow deposits, show better sorting compared to Walker's pyroclastic flow data.

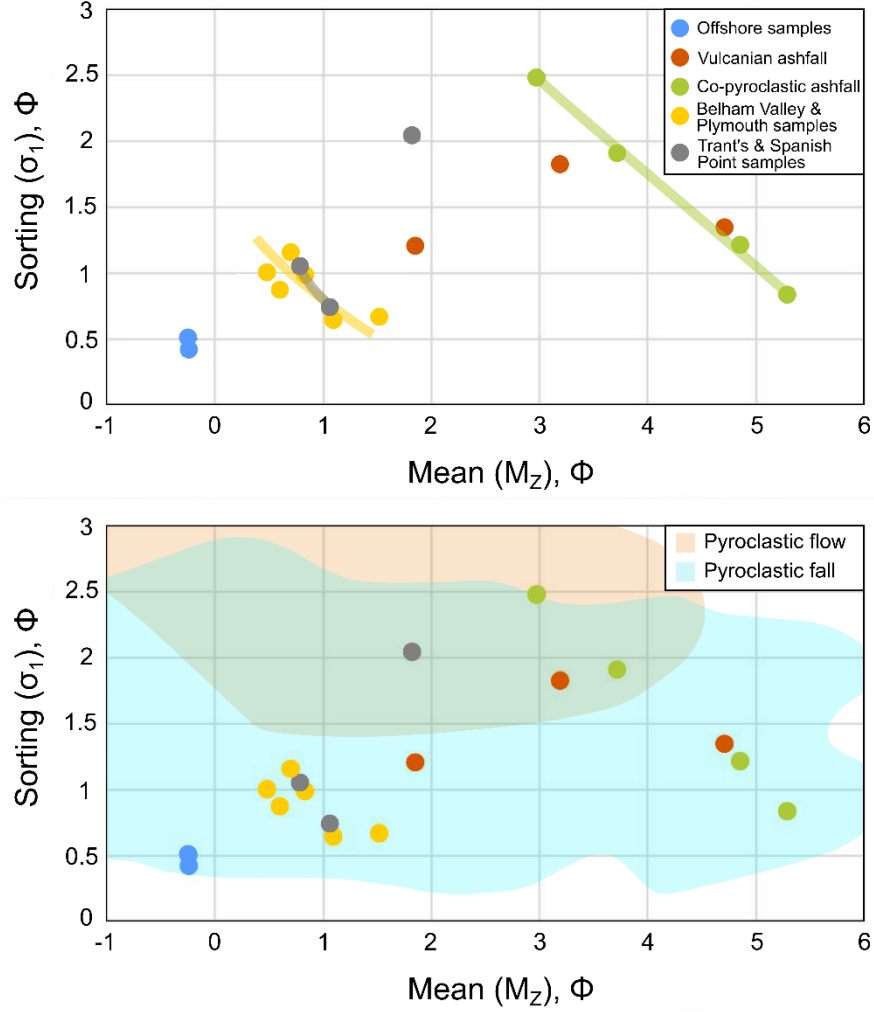


Figure 9: Median diameters vs. sorting coefficients of the 18 samples. The color code is adopted from Table 4. The upper diagram shows that a better sorting can be observed with decreasing grain size (trend lines). However, this is not comprehensible for every environment. The orange and blue fields resemble the areas of pyroclastic flow and fall deposits after WALKER (1971).

4.2 Grain shape analysis

Figure 10 illustrates the rounding classes as cumulative weight percentages according to POWERS (1953). Conspicuously, the majority of grains in each sample is subangular to rounded, with the most represented rounding classes subrounded and rounded. However, only a small part of the grains is very angular, angular, or well rounded. In addition, each sample has a residual portion with a rounding of less than 0.12, which according to POWERS (1953) only occurs on crystal fragments. It should also be noted that the sample MVO1705 could not be taken into account for the grain shape analysis because the amount of the selected grain size for the preparation of the thin sections was not sufficient.

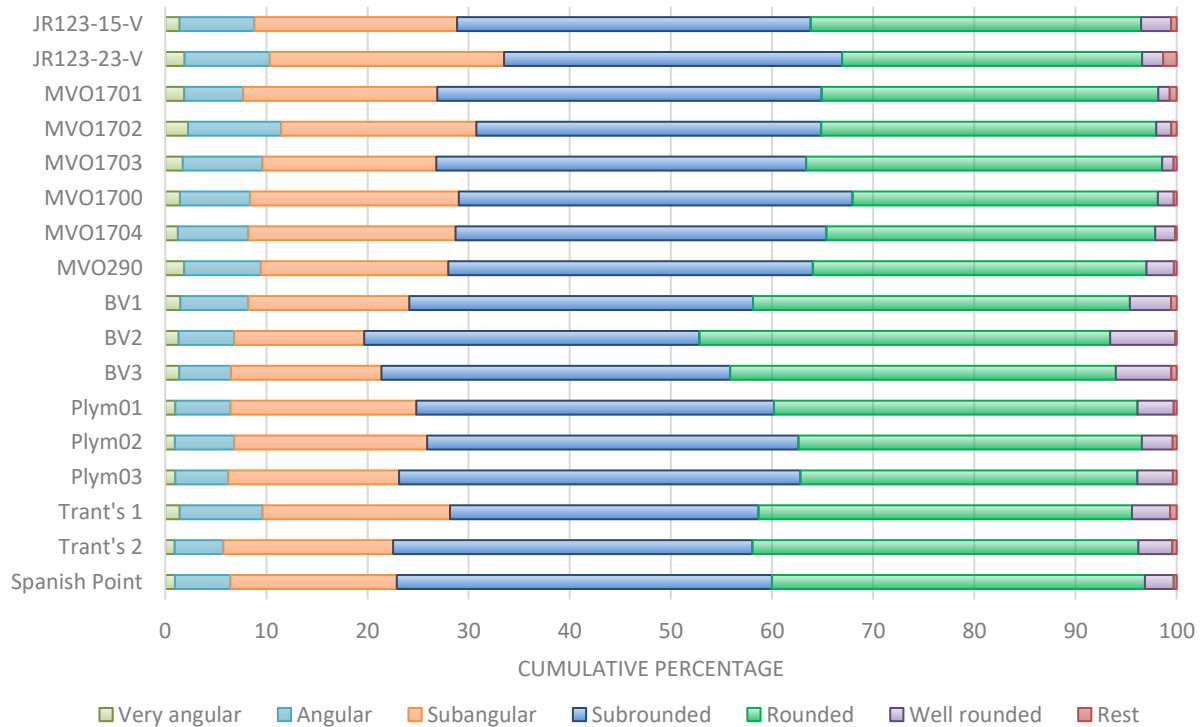


Figure 10: Overview of the cumulative percentage of the roundness classes after POWERS (1953) calculated for each sample.

4.3 Microscopy

The results of the microscopical analysis are presented in the following. Information from both reflected-light and transmitted light microscopy are included. The abbreviations of the mineral names in the thin sections were selected after WHITNEY & EVANS (2010).

4.3.1 Offshore samples

JR123-15-V and JR123-23-V are located about 3–7.5 km offshore the eastern coast of Montserrat. Nevertheless, both samples have a strong similarity and consist mainly of broken plagioclase crystals and different types of clasts (see Figure 11). Firstly, these are plagioclase-phyric and hornblende-phyric juvenile andesitic lava clasts with a microcrystalline groundmass and, less abundant, dark grey to black, primarily vitreous clasts with a low vesicularity. TROFIMOV ET AL. (2008) have published similar observations. Moreover, broken crystals of ortho- and clinopyroxenes as well as hornblende is present, with increasing abundance with smaller grain size. According to TROFIMOV ET AL. (2008), the marine deposit also contains hydrothermally altered porphyritic andesite clasts coated with iron and sulphur compounds, a feature hereby verifiable. Furthermore, biogenic fragments could be identified. It is noticeable that grains of the offshore samples are affected by greater alteration than other samples. This could be caused by the entrainment of older grains by mass movement processes.

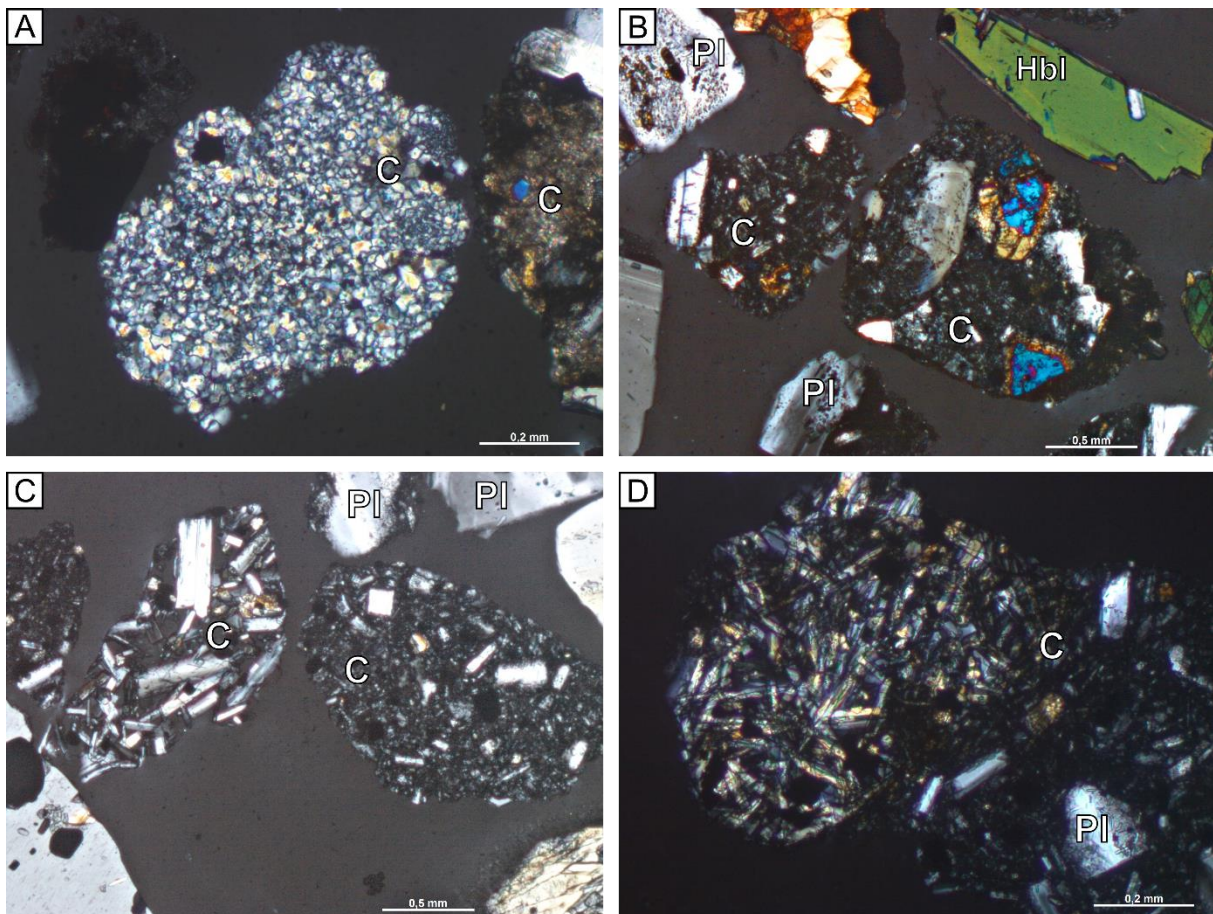


Figure 11: **A** –Lithic clast (C) with granular groundmass of plagioclase and pyroxene (centre). JR123-23-V. **B** – Porphyritic clasts (C) with plagioclase and clinopyroxene phenocrysts in a vitric matrix surrounded by hornblende (Hbl) and plagioclase (Pl) crystal fragments. JR123-15-V. **C** –Overview of porphyritic clasts (C) and broken plagioclase (Pl) crystals. JR123-23-V. **D** – Plagioclase and pyroxene crystals are irregularly distributed in the vitric matrix of a clast (C). JR123-23-V. All images were taken under crossed nicols.

4.3.2 Vulcanian ashfall samples

The Vulcanian ashfall samples (MVO1701, MVO1702 and MVO1703) were collected in Lookout and MVO South in September and October 1997 after heavy Vulcanian explosions of Soufrière Hills Volcano.

They consist mainly of juvenile andesitic lava clasts (Figure 12). These clasts are highly porphyritic with plagioclase and pyroxene crystals and they have a glassy groundmass. Another type of clast has a glassy groundmass with enclosed phenocrysts of plagioclase and the opaque phase. There are also glomerophyric structures, with crystal aggregates of plagioclase, amphibole and pyroxene. Moreover, broken plagioclase, ortho- and clinopyroxene as well as amphibole (mainly hornblende) crystals can be found in these samples. There are lava fragments with elongated vesicles imitating a flow foliation (see Figure 12 C and D). Plagioclase shows oscillating zonation as can be seen on the aligned plagioclase prisms.

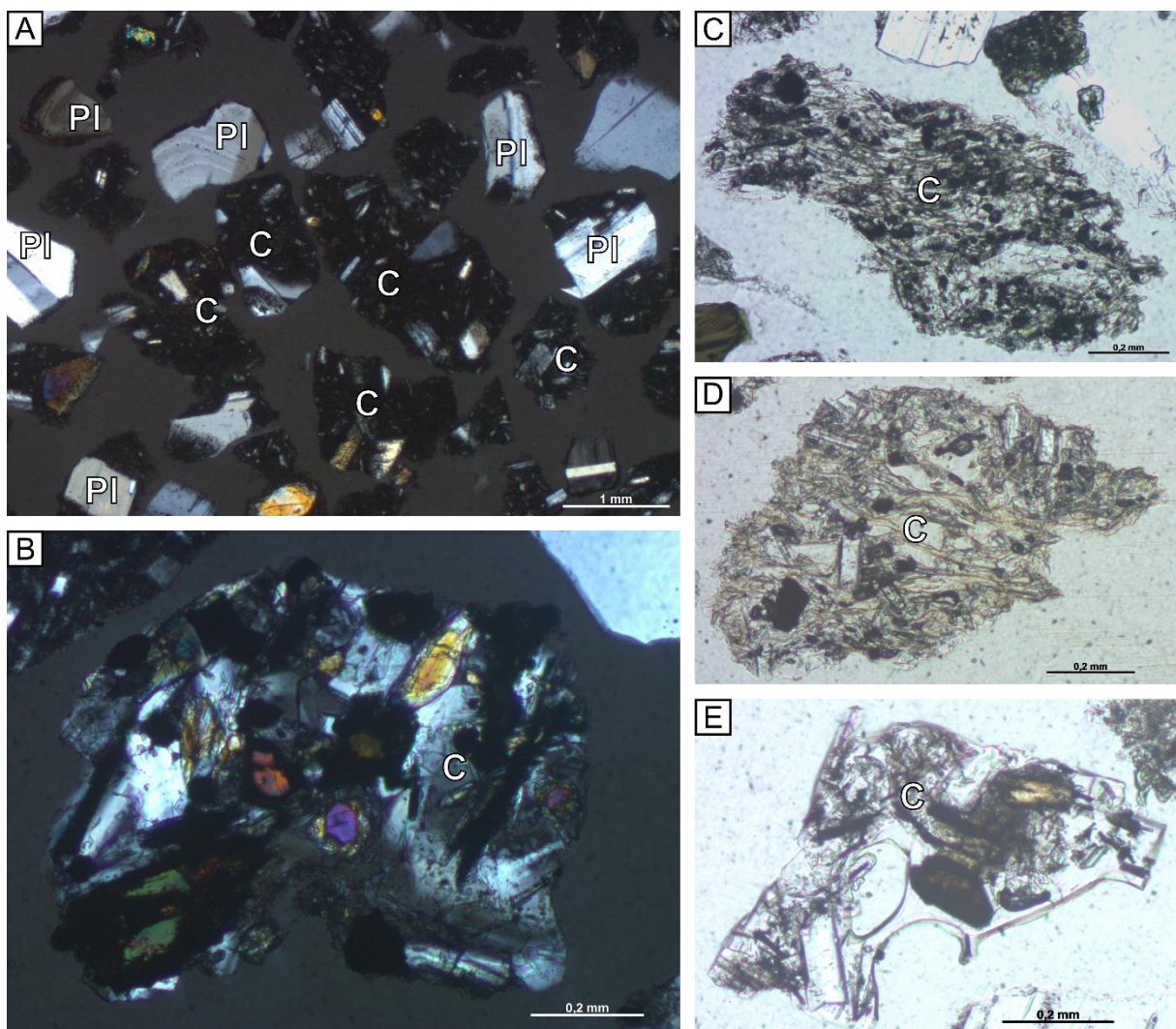


Figure 12: **A** – Overview of sample MVO1703 with juvenile andesite lava fragments (C) and broken plagioclase (PI) crystals. Crossed nicols. **B** – Glomerophyric clast (C) consisting of plagioclase, hornblende and pyroxene crystals. MVO1701. Crossed nicols. **C** – Vitric pumice with plagioclase and opaque mineral phenocrysts showing flow foliation. MVO1702. **D** – Pumice with elongated vesicles, plagioclase and opaque minerals as phenocrysts in the matrix. MVO1701. **E** – Glass shard with a single large vesicle and with amphibole phenocrysts. MVO1701.

4.3.3 Co-pyroclastic flow ashfall samples

The samples of the co-pyroclastic ash fall deposits (MVO1700, MVO1704, MVO1705 and MVO290) were mainly taken in the southern to western part of Montserrat and can be assigned to various volcanic events in 1997.

In terms of composition, there is no difference compared to the other samples and they are mainly composed of single plagioclase crystal fragments and various clast types (Figure 13). These are, for example, juvenile lava fragments with a significant percentage of vesicles and highly porphyric andesitic clasts, mainly comprising plagioclase and orthopyroxene in a glassy groundmass. Amphibole (mainly hornblende), pyroxene and an opaque mineral phase which is probably magnetite are also present. Plagioclases often have a glassy rim around the crystal with a flame-like structure in the thin section.

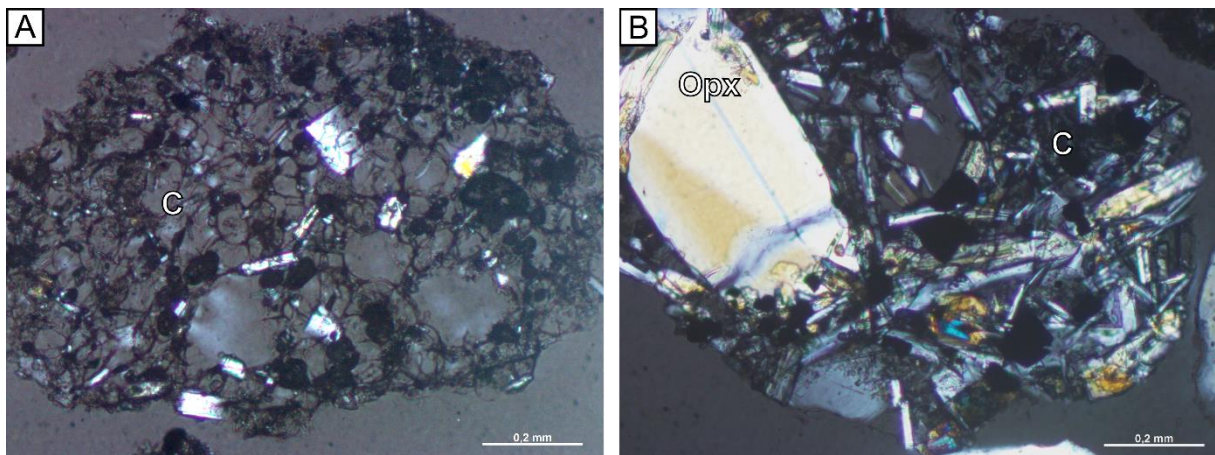


Figure 13: **A** – Highly vesicular lava fragment (C) with plagioclase and phenocrysts in the groundmass. MVO290. Crossed nicols. **B** – Juvenile clast (C) with orthopyroxene crystals in a coarse-grained vitreous groundmass rich in plagioclase, orthopyroxene (Opx) and opaques. MVO290. Crossed nicols.

4.3.4 Belham Valley (BV) & Plymouth (Plym) samples

The specimens BV1, BV2, BV3, Plym01, Plym 02 and Plym 03 were collected from Belham Valley and Plymouth in the western part of the island. They are nearshore deposits which have been influenced by various reworking events (e.g. lahars, ash falls and coastal relocation processes).

Plagioclase, amphibole (hornblende) and pyroxene (orthopyroxene and clinopyroxene) crystals as well as different types of clasts dominate the composition of these samples. Often the juvenile andesite lava fragments are characterized by a considerable number of vesicles, which can be easily identified by the blue epoxy resin (Figure 14). In addition, etching structures occur on pyroxene in sample BV1, shown in Figure 14 by comparison with an SE image of the same sample. Furthermore, individual crystals often occur enclosed by highly vesicular glass (see Figure 14 E). Plagioclases is characterized by polysynthetic twinning, oscillating zonal structure and melt inclusions. As in the previous samples, there is a considerable amount of an opaque mineral phase which is probably magnetite. This statement is supported by the fact that the loose grains reacted strongly to a magnet.

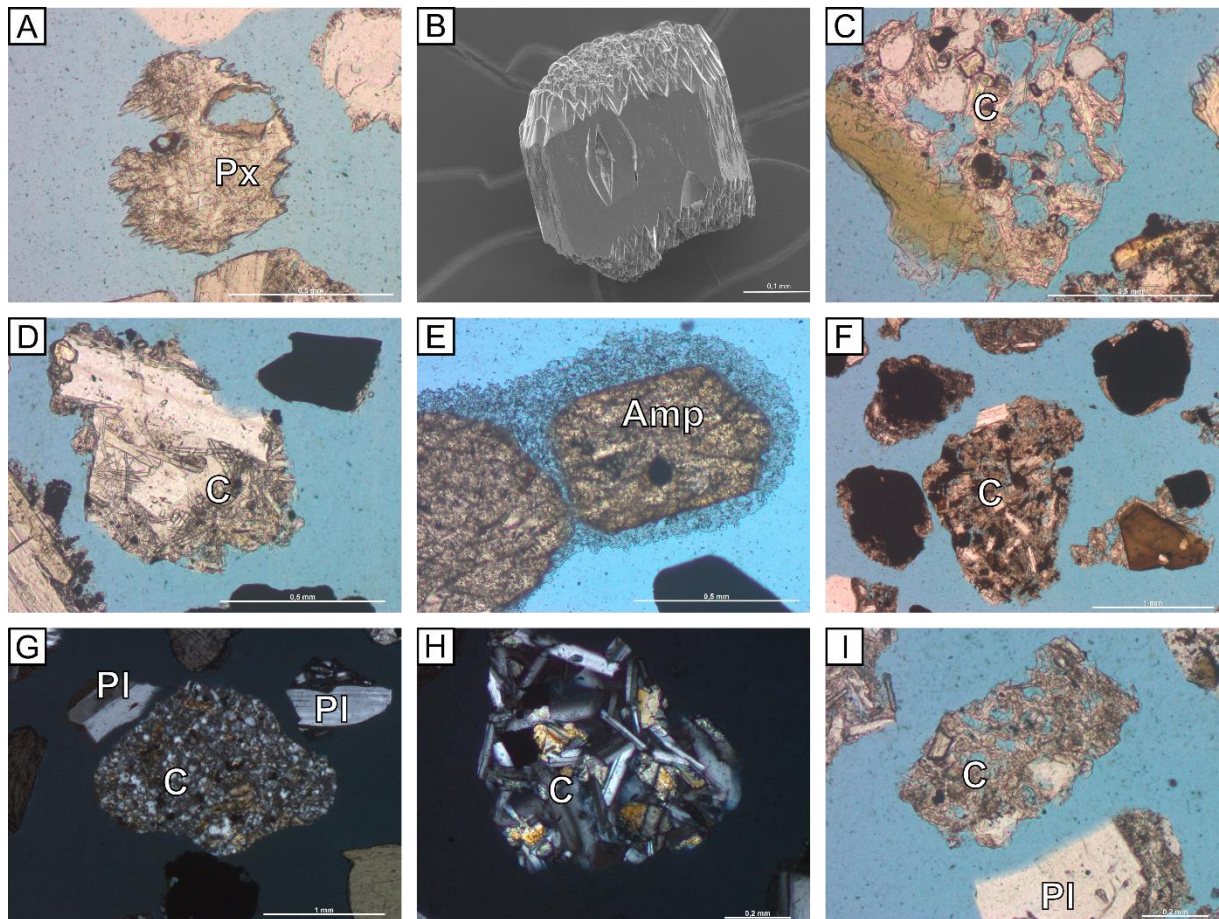


Figure 14: **A** – Etched pyroxene crystal with characteristic needle-like endings. BV1. **B** – SEM picture of an etched pyroxene grain of BV1. **C** – Highly vesicular clast with plagioclase, hornblende and opaque mineral phenocrysts. BV1. **D** – Twinned plagioclase crystals in a glassy groundmass. BV2. **E** – Amphiboles with a striking foamy glass rim. BV2. **F** – Overview of a porphyritic andesite clast and an opaque mineral phase. BV2. **G** – Clast with a homogeneous groundmass of plagioclase, pyroxene and the opaque mineral phase identified as magnetite. BV3. Crossed nicols. **H** – Glomerophytic texture of plagioclase and pyroxene. Plym01. Crossed nicols. **I** – Juvenile lava fragment with a medium vesicularity. Plym01.

4.3.5 Trant's and Spanish Point Samples

The samples from Trant's and Spanish Point (Figure 15) are located in the eastern part of Montserrat and were taken close to the beach with one of the samples (Trant's 2) coming from a block-and-ash flow deposit.

Trant's 1 consists mainly of the opaque phase magnetite and has less plagioclase compared to the previous samples. As before, different types of clasts can be distinguished. On the one hand there are juvenile andesite clasts with a high vesicularity, on the other hand there are porphyritic clasts in which plagioclase and pyroxene are embedded as phenocrysts in a very fine-grained microcrystalline matrix. In addition, glomerophytic textures with plagioclase, amphiboles, pyroxenes and the opaque minerals also occur. The composition of the samples Trant's 2 and Spanish Point changes only due to the fact that Trant's 2 apparently contains more lava clasts and Spanish Point has a higher plagioclase content. All samples include amphibole and some biogenic fragments (shell and coral fragments). Figure 15 (D and E) shows the glassy coating, which is described in Chapter 4.5.3, on a plagioclase in the thin section as well as in a BSE image.

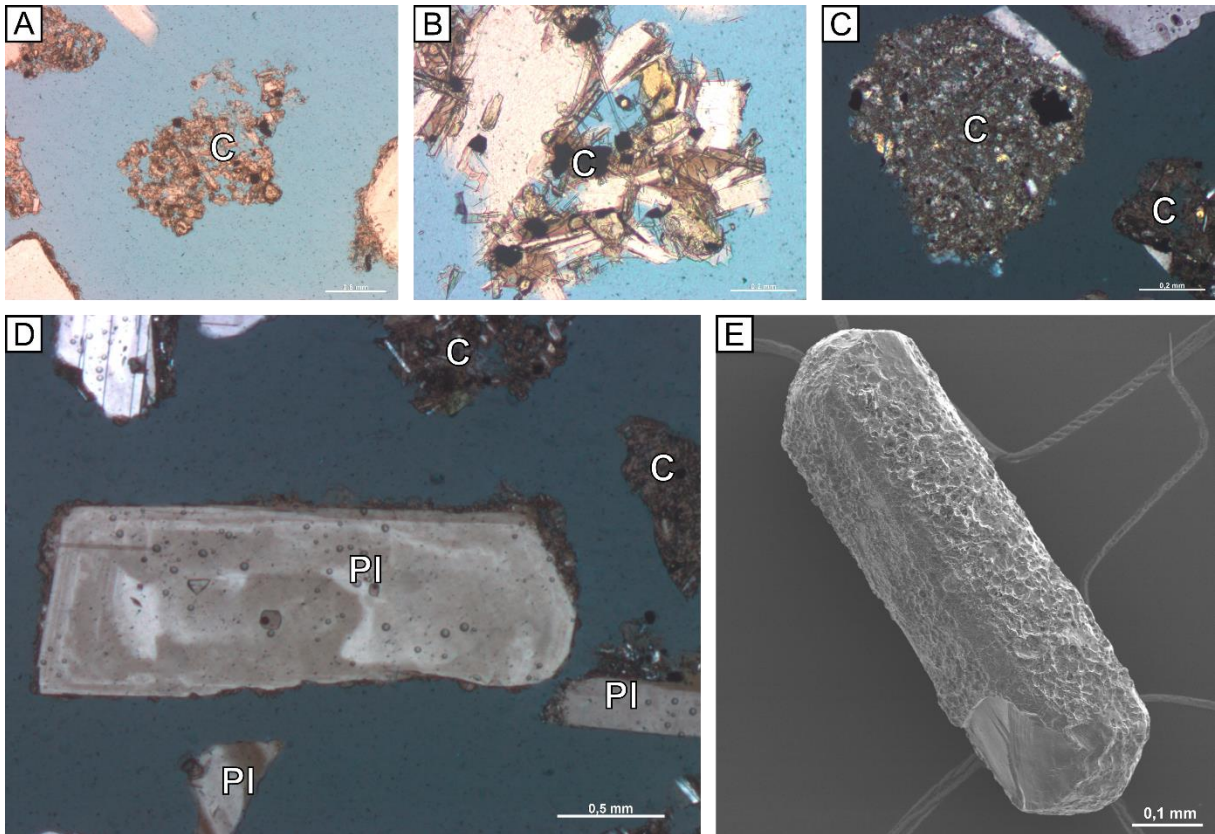


Figure 15: **A** – Highly vesicular juvenile lava fragment. Spanish Point. **B** – Glomerophytic texture of plagioclase and pyroxenes. Trant's 1. **C** – Fine-grained andesite clast with phenocrysts of plagioclase and opaque minerals. Spanish Point. Crossed nicols. **D** – Plagioclase with oscillating zonation and a flame-like wall. Spanish Point. **E** – SEM picture of a plagioclase crystal with a bubble-wall texture for comparison with the thin section. Spanish Point.

4.4 Point Counting

Using the *JMicroVision* program, all samples (except MVO1705) were point counted (leaving out the embedding epoxy) and divided into different phases (plagioclase, rock fragments, amphibole, pyroxene, opaque phase, biogenic fragments and accessory minerals). Thereby it was obvious that in most samples a large part consists of plagioclase and rock fragments (Figure 16). Amphibole, pyroxene and accessory minerals are of minor importance. However, there are 3 samples (BV1, BV2 and Trant's 1) in which amphibole, pyroxene and especially the opaque phase (probably magnetite) represent a significant part. Biogenic fragments (such as shell or coral fragments) could only be detected in the offshore samples and in parts of the Belham Valley and Plymouth specimens. The accessory minerals include those that have been overprinted by transformation processes (such as opacitization).

The different types of the rock fragments as mentioned before were not distinguished here, whereas the phenocrysts and the groundmass were considered as separated categories to provide a general overview of the crystallinity range of the rock fragments. The crystallinity range varies from 14 % (MVO1702) to around 37 % (BV3) with most samples ranging between 21 and 33 %. A table with the amounts of groundmass and phenocrysts is given in Appendix 5. It is noticeable that only a few samples are different to the rest. This includes the samples BV2, BV3 and Trant's 1. They show a larger amount of the opaque mineral phase, amphibole and pyroxene, but they consist of less plagioclase and rock fragments. Furthermore, the amount of rock fragments in the offshore samples JR123-15-V and JR123-23-V is smaller, whereby the fraction of biogenic fragments is the highest of all specimens.

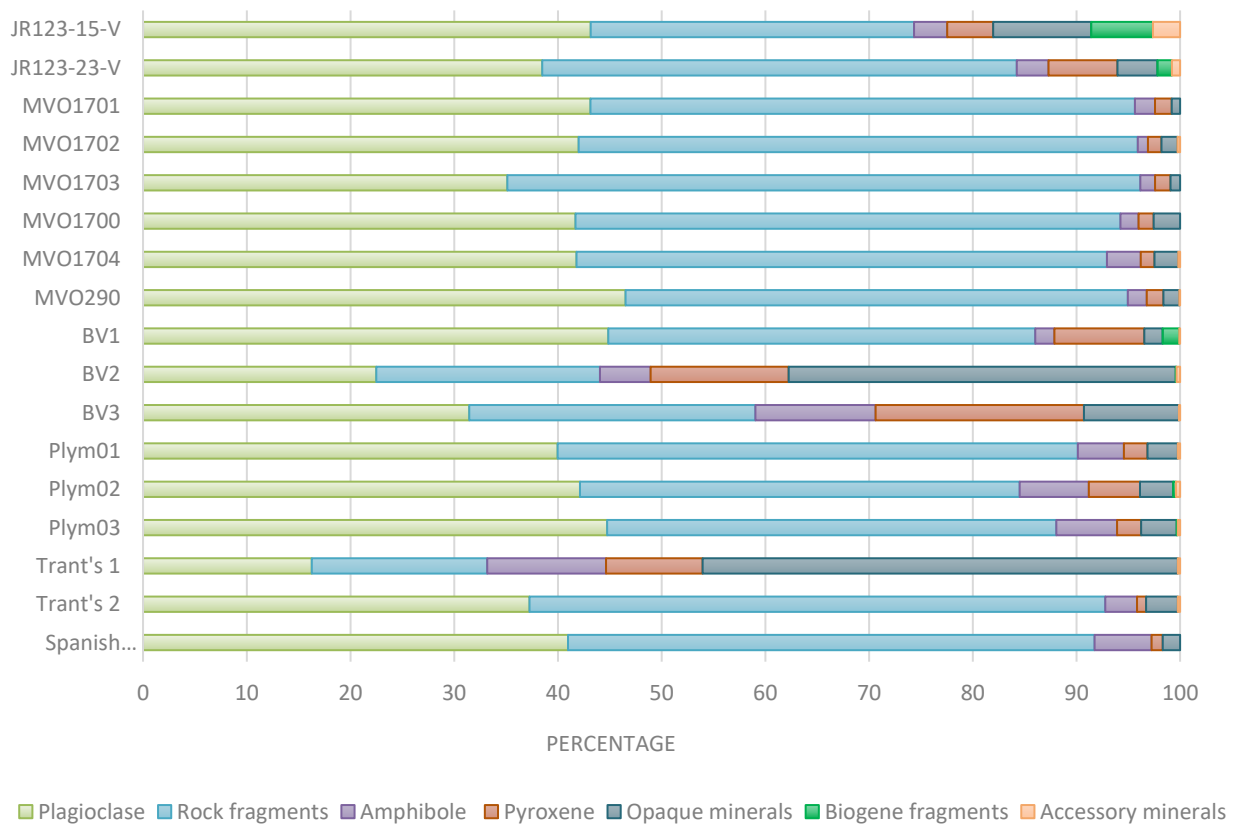


Figure 16: Cumulative percentage of rock fragments and phenocrysts estimated by point counting.

4.5 Microtextures

In the following paragraph 36 microtextures, which could be identified on the surface of grains, are introduced and described. Furthermore, SEM pictures provide an insight into the spectrum of microtextures. They were selected, combined and described following the definitions of WOHLETZ & KRINSLEY (1982), HEIKEN & WOHLETZ (1985), MAHANEY (2002) and VOS ET AL. (2014). The different textures are associated with possible formation processes. From each of the 18 samples, 50 grains were selected (3 samples with 70 grains) and observed using a SEM. An image was taken of each grain and, in the case of conspicuous microtextures, a detailed image as well. All images taken of the grains and their surfaces can be found in the electronic appendix. In addition to the description of the individual microtextures and their illustration in picture panels, the corresponding data table with the quantified textures of the examined grains can be found in Appendix 6 and 7.

4.5.1 Grain outline and relief

The first step was to classify the grains according to their shape, which means that a visual evaluation of the relief and the grain outline (rounding) was attempted (Figure 18). While the grain outline describes the roundness or angularity of a grain, the relief defines the surface, which ranges from smooth to rough. The shape of a grain is influenced by external environmental influences and can therefore be altered by mechanical or chemical processes. The grains were divided into low, medium and high in both categories, whereby a low grain outline is synonymous with rounded grains and a low relief shows smooth surfaces. Rounded grains are very limited, and the majority of grains display a high grain outline, which means they are angular (see Figure 17). There is no clear trend among the different deposit types. The same can be observed for the relief, whereas the lower type is more prominent. Apparently, the reason for this is the common presence of fresh fractures and fissures, weathering apparently had little influence yet. Another important fact is the short period of time in which the volcanic material was erupted, transported and deposited.

Grain outline

- #1 Low: Rounded grains with smooth edges.
- #2 Medium: Subangular grains with slightly blunted edges.
- #3 High: Angular grains with sharp edges.

Relief

- #4 Low: Smooth to nearly smooth surfaces without topographic irregularities.
- #5 Medium: Semi-smooth surfaces with topographic irregularities.
- #6 High: Topographically irregular surface with pronounced swells and swales.

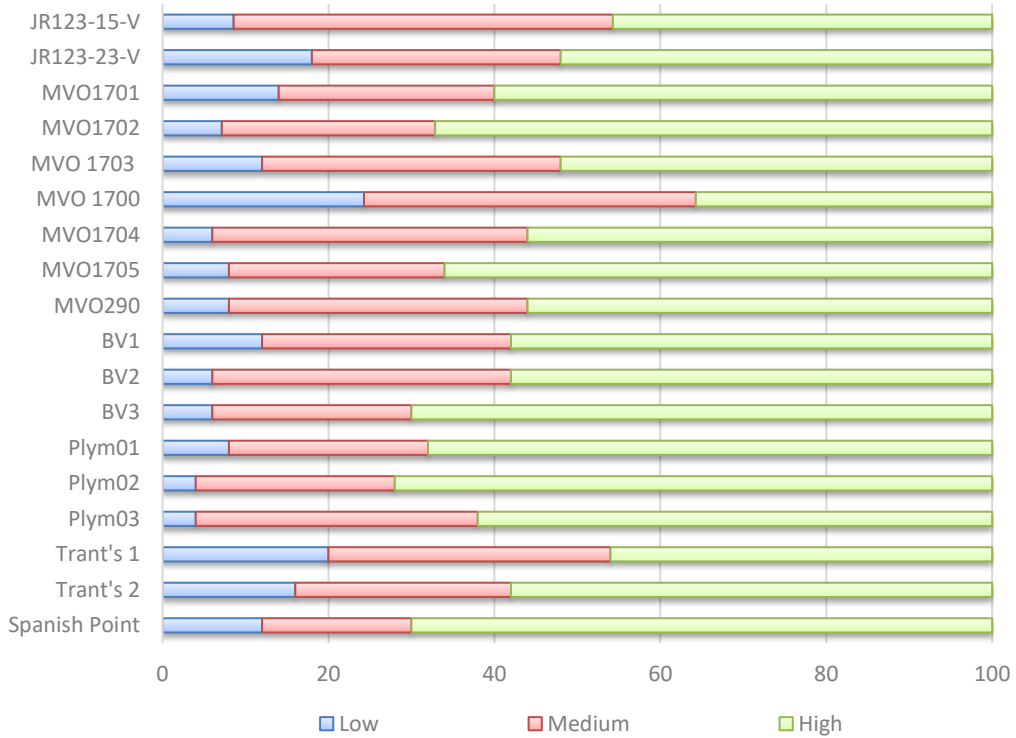
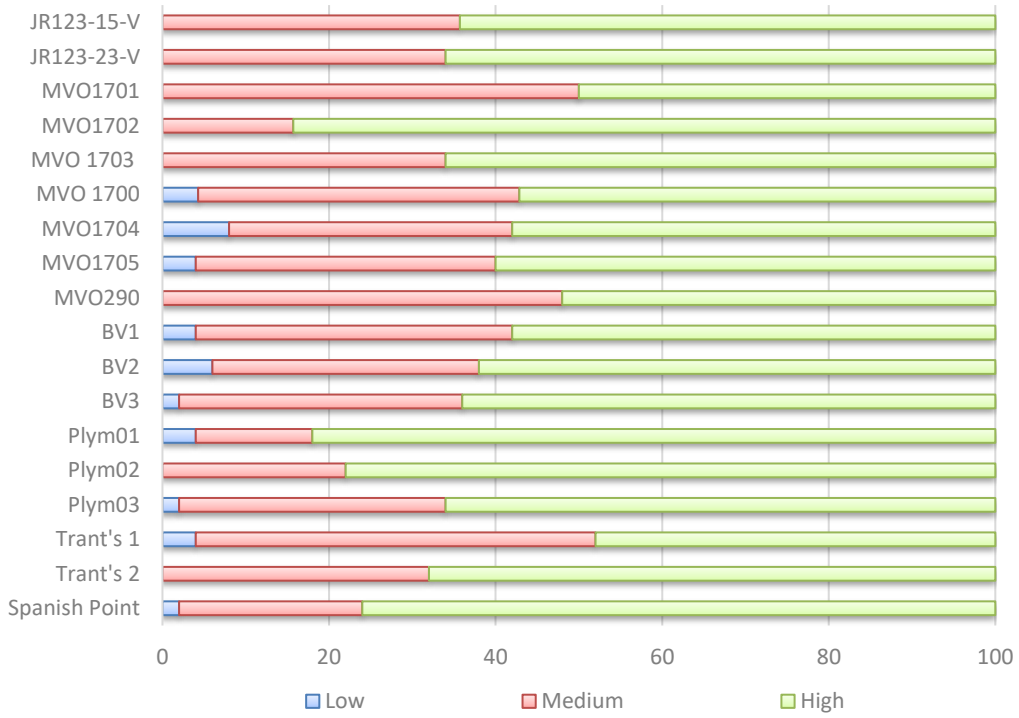


Figure 17: The upper diagram shows the grain outline of the analysed grains and their association to low (rounded), medium (subangular) and high (angular). The lower diagram depicts the relief regarding to the classification low (smooth), medium (semi-smooth) and high (irregular).

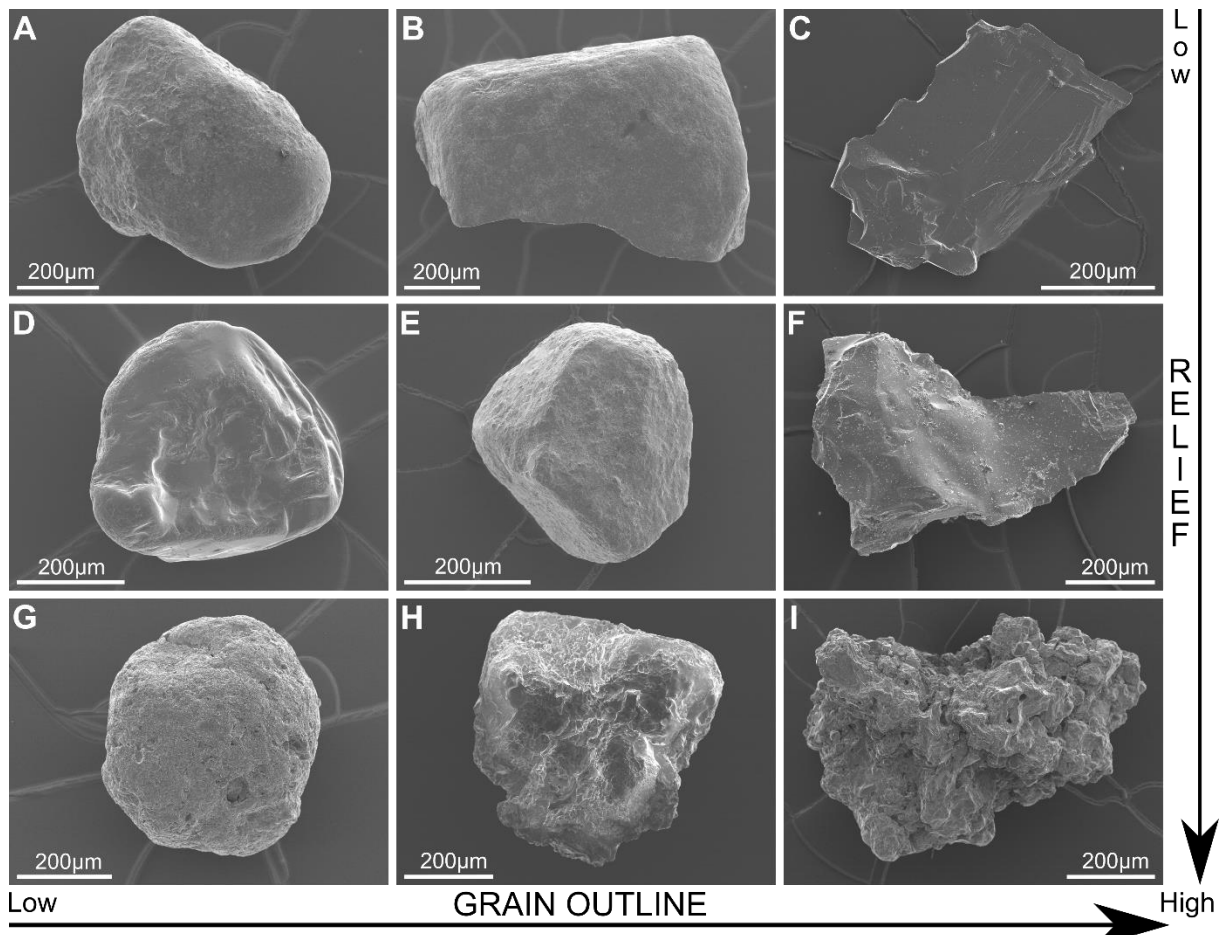


Figure 18: SEM micrographs of the different types of grain outline and relief. The grains are shown from top left to bottom right with increasing grain outline and relief. **A** – Amphibole with smooth edges and low relief. BV2. **B** – Plagioclase with semi-smooth edges and low relief. Trant's 1. **C** – Glass with sharp edges and low relief. JR123-15-V. **D** – Amphibole with smooth edges and medium relief. BV2. **E** – Pyroxene with medium grain outline and relief. Plym02. **F** – Glass with sharp edges and medium relief. JR123-15-V. **G** – Plagioclase with a smooth grain outline and a high relief caused by weathering. BV1. **H** – Plagioclase with semi-smooth edges and a high relief. JR123-23-V. **I** – Clast with a high grain outline and relief. Plym01.

4.5.2 Mechanical features

A differentiation was made between 18 microtextures, which were generated by mechanical forces on the grains. The description of the surface structures and images can be seen below.

#7 Flat cleavage surface

Site of fractures caused by mechanical stress along the cleavage surfaces of the minerals. Mainly seen on plagioclase (see Figure 19 A, B, Figure 20 E and Figure 23 E), but generally minerals with good cleavage properties are appropriate for this texture. They appear frequently in offshore samples.

#8 Fresh surface

Surfaces (Figure 19 B, Figure 20 A, Figure 21 B and Figure 22 E) without any influence of weathering (e.g. etching or dissolution), however, they can be affected by mechanical influences during transport. Many of the fresh surfaces are represented in the offshore samples.

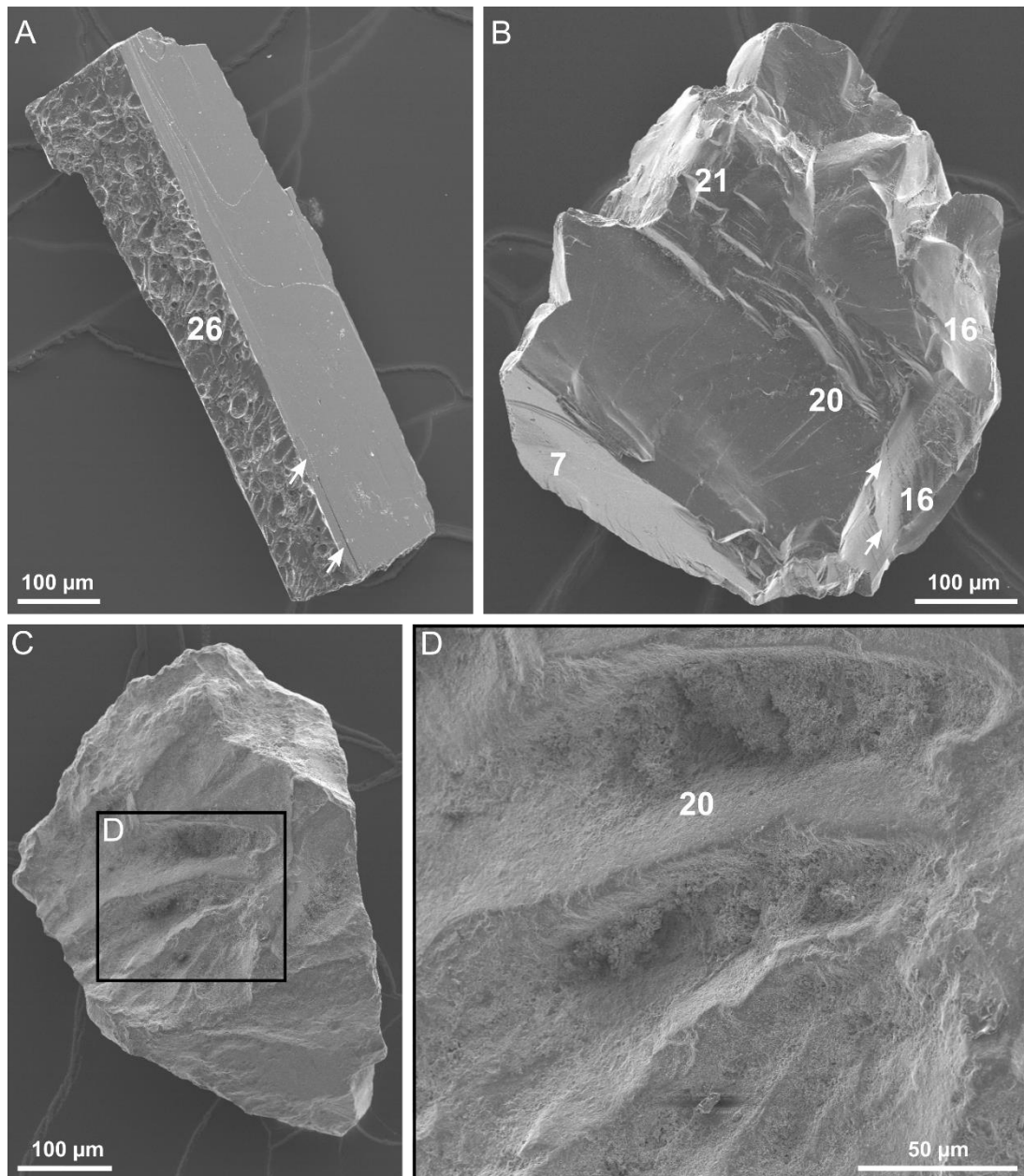


Figure 19: SEM micrographs of surface textures on grains to compare flat cleavage, fresh and weathered surfaces. **A** – Plagioclase with a flat cleavage surface and a glassy coating (26) showing vesicularity. JR123-15-V. **B** – Plagioclase with a fresh surface and a flat cleavage (7). Note straight (21) and arcuate (20) steps as well as conchoidal fractures (16). BV1. **C** – Weathered surface of a magnetite with high grain outline and relief. Furthermore, arcuate (20) steps can be seen in the centre of the grain. Plym02. **D** – Enlargement of the arcuate steps and the weathered surface of the grain in picture C. Plym02. The numbers represent the microtextures in the text.

#9 Crater

Any type of depression that can vary in shape and size caused by impact like grain-grain or grain-substrate contact (see Figure 20 A, E, Figure 21 A, B, Figure 25 F and Figure 27 C). Craters are well represented in each sample and in the ash fall deposits they are not as common as in the others.

#10 Sawtooth structure

As the name suggests, this texture looks like the teeth of a saw (see Figure 20 B). The origin is accompanied by an expended effort of energy, like high compressional stress (MAHANEY, 2002). Sawtooth fractures are rarely found in the samples.

#11 Microcracks

A distinction is made between microcracks (Figure 20 F, Figure 21 B, C, Figure 22 E, F and Figure 23 A, B) caused by mechanical or chemical processes and hydration cracks (Figure 20 C) caused by volume changes during hydration (HEIKEN & WOHLLETZ, 1985). The former is triggered by heavy impacts and can cause the grain to partially or completely break apart and gradually turn into adhering particles. Microcracks can vary in size, width and depth. Whereas the hydration cracks are caused by desiccation of the vitreous skin covering the pyroclast. In the ashfall samples they are more common.

#12 Abrasion features

Microtextures that have a worn surface due to grinding processes caused by wind, water, ice or gravity (MAHANEY, 2002; see Figure 20 D or Figure 26 A). They are rarely present in the offshore samples and scarcely or not present in all other samples.

#13 Parallel ridges

Parallel ridges (Figure 20 B and F) or striations can appear on the whole grain but are often associated with smooth surfaces. However, they have been found more frequently on grains of the offshore samples as well as on grains of ash fall deposits. A possible cause could be colliding sharp-edged grains generated during transport. They can be found in the offshore as well as in the ashfall samples.

#14 Grain rounding

Grain rounding (Figure 21 A, Figure 24 E, Figure 26 E and Figure 27 C) or edge rounding (MAHANEY, 2002) is associated with the smooth abrasion of the edges of the grain up to nearly round individuals (see grain outline). There is no trend favoring a particular deposition type.

#15 Chipped edges

Dish-shaped, v-shaped or uneven fractures occur orientated along the edges of a grain (see Figure 21 C, D and Figure 22 C). This textural feature is caused by edge rounding as a consequence of abrasion (HEIKEN & WOHLLETZ, 1985). Chipped edges are present in all samples without a tendency to a depositional type.

#16 Conchoidal fractures

In the examined specimens, the conchoidal fractures (see Figure 19 B, Figure 20 A, B, Figure 21 C, Figure 22, Figure 23 A, C, E and Figure 24 C) appear on almost every crystal, including plagioclase, amphibole and glass without restriction to a certain depositional type. They have a shell-like appearance and can vary significantly in size. Varying from a few tens of micrometers to a several hundred micrometers, all diameters are represented, and the texture can cover up to 50% of the surface of a grain. The formation of conchoidal fractures can be traced back to strong impacts or high pressures exerted on the crystal lattice (VOS ET AL., 2014). WOHLLETZ & KRINSLEY (1982) associated these strong mechanical impacts with transport conditions after magma fragmentation and quenching. Moreover, it should be mentioned that arcuate and straight steps can be associated with conchoidal fractures.

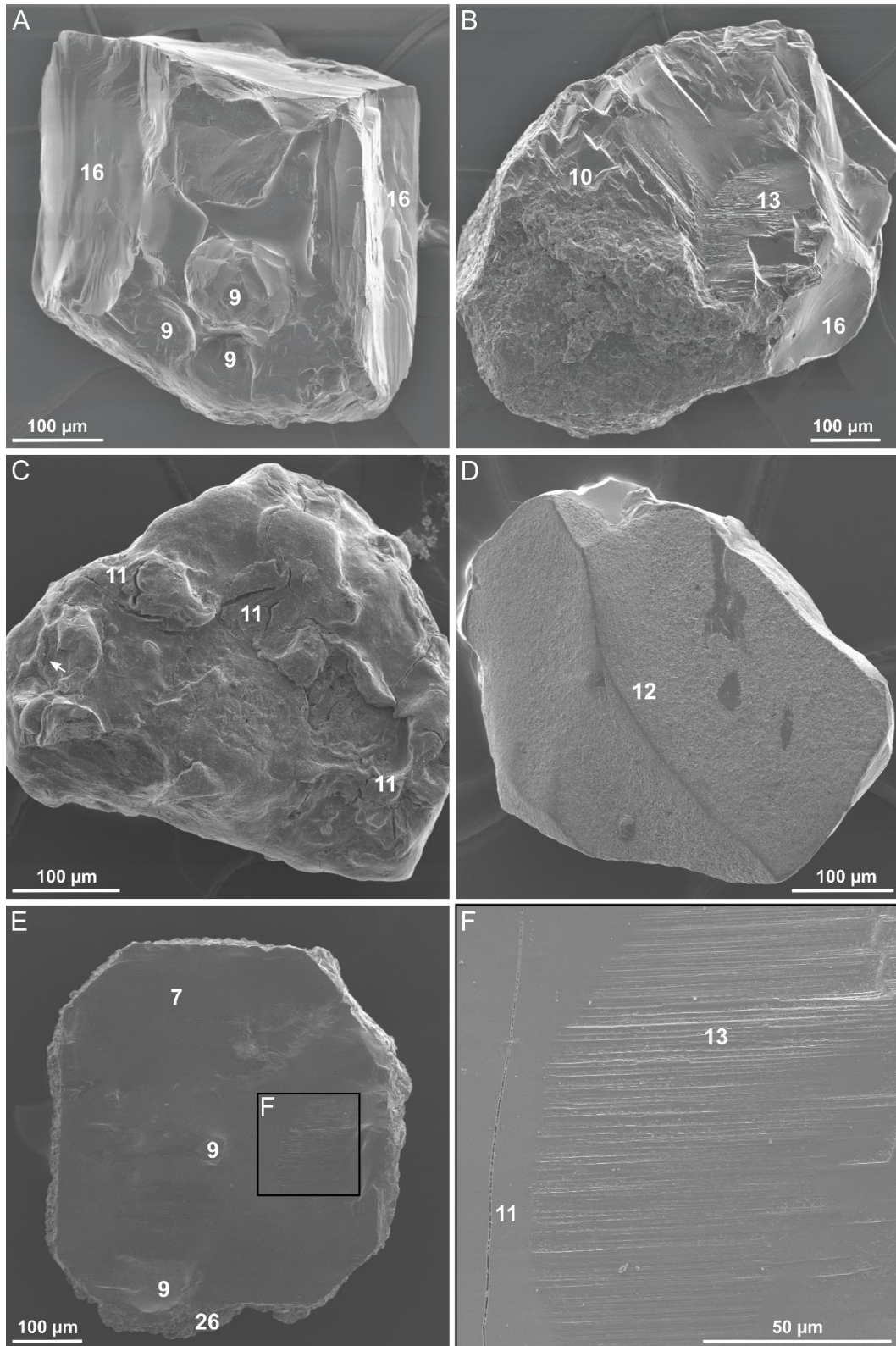


Figure 20: SEM micrographs of surface textures on grains. **A** – Amphibole with a blocky shape. The fresh surface is covered with craters (9) and conchoidal fractures (16). The grain probably has experienced strong mechanical stress. JR123-15-V. **B** – Grain with sawtooth fractures (10), parallel striations (13) and conchoidal fractures (16). The right part appears to be fresh and the lower left part is weathered. JR123-23-V. **C** – Epidote revealing grain rounding, a weathered surface and microcracks (11). In this case they are hydration cracks. MVO1701. **D** – A grain with ferrous coating and abrasion features (12). BV1. **E** – A pyroxene in cross section with a flat cleavage surface, crater (9) and glassy overgrowth (26) surrounding the crystal. The black box marks the enlargement of picture F. JR123-23-V. **F** – Enlargement of picture E showing parallel striations (13) and a small microcrack (11). JR123-23-V. The numbers represent the microtextures in the text.

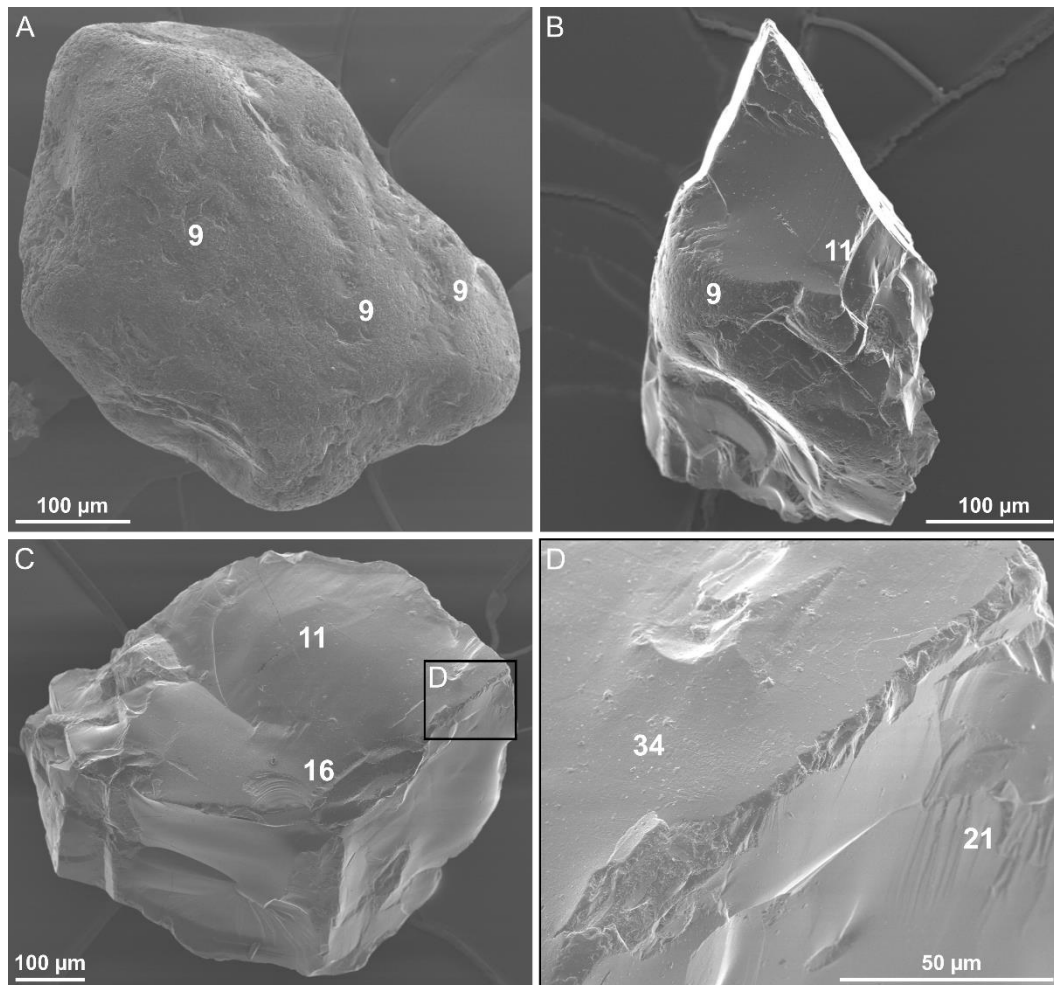


Figure 21: SEM micrographs of surface textures on grains. **A** – A well rounded, weathered plagioclase its surface scattered with impact craters (9). MVO1705. **B** – See the opposite: a sharp-edged plagioclase with fresh surfaces, microcracks (11) and small craters (9). JR123-15-V. **C** – Amphibole with a blocky shape, covered by conchoidal fractures (16) with arcuate steps, microcracks (11) and chipped edges. The black box marks the enlargement in picture D. JR123-23-V. **D** – Enlargement of picture C showing a chipped edge, adhering particles (34) and straight steps (21). JR123-23-V. The numbers represent the microtextures in the text.

#17 Grooves and scratches

Both, grooves and scratches (Figure 22 D) can be curved or straight and vary in size and length. They can occur either individually or in groups of scratches with a specific orientation direction. Most of them are found on grains from the offshore and coastal samples, which have been influenced by various volcanic events, transportation and relocation processes. MAHANEY (2002) described the occurrence of grooves in mass waste debris.

#18 Radial fractures

Radial fractures were created by impact and radially move away from the crater (Figure 22 F). The degree of fracture propagation depends on the strength of the impact (MAHANEY, 2012). They are rarely found on the grains.

#19 Sharp angular features

It includes any kind of sharp-edged texture on the grain surfaces (see Figure 21 B, Figure 22 A and Figure 23 B). They occur on grains in the offshore samples, the ashfall products as well as in the coastal specimens.

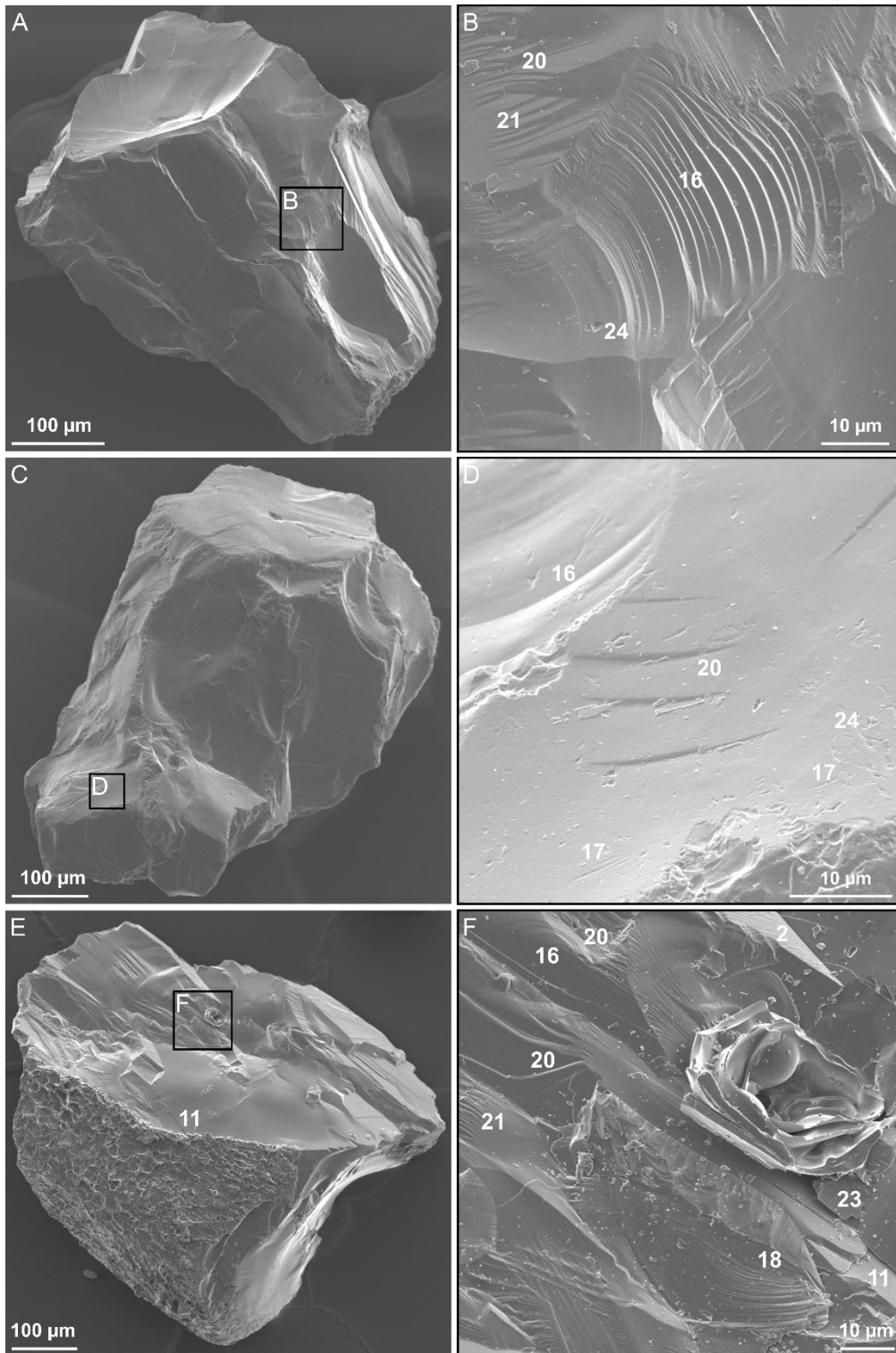


Figure 22: Micrographs of some surface textures on grains. **A** – Angular plagioclase with several conchoidal fractures. A detailed view can be seen in the enlargement in picture **B** (black box). JR123-15-V. **B** – Enlargement of the conchoidal fracture (16) of picture **A** with straight (21) and arcuate (20) steps. Note the V-shaped percussion crack (24). JR123-15-V. **C** – Another blocky plagioclase showing conchoidal fractures and chipped edges. The black box is representing the enlargement in **D**. JR123-15-V. **D** – Enlargement of the surface of a plagioclase with a part of a conchoidal fracture (16), widely diverging parallel arcuate steps (20), some V-shaped percussion cracks (24) and small (up to 5 μm) scratches (17) orientated in one direction. JR123-15-V. **E** – Vitric clast covered with conchoidal fractures on a fresh surface and partly glassy overgrowth. Number 11 marks a microcrack several hundreds of μm long. MVO1702. **F** – Enlargement marked in picture **E** with the black box. Note the detailed overview of a microcrack (11), a small broken plate (23), a conchoidal fracture (16), straight (21) and arcuate steps (20) as well as the radial structure (18) and the remnant of a broken vesicle. MVO1702. The numbers represent the microtextures in the text.

#20 Arcuate steps and #21 Straight steps

MAHANEY (2002) described them as arc-shaped (Figure 19 B, Figure 21 C, Figure 22 B, D, F, Figure 23 A, Figure 24 C, Figure 25 E and F) and linear steps (Figure 19 B, C, D, Figure 21 D, Figure 22 B, F, Figure 23 A, D, Figure 24 C, Figure 25 E and F), similar to conchoidal fractures, but with deeper breaks in the mineral structure. They are the result of impact and pressure on the mineral structure. According to MARGOLIS & KRINSLEY (1974), they can also be understood as zones of weakness in glass, similar to the cleavage surfaces in crystals, or as products of acoustic wave phenomena (KRAGELSKII, 1965). Since the steplike features are associated with conchoidal fractures, they are equally common on grain surfaces and there are no restrictions regarding the origin of the samples.

#22 Upturned plates

WOHLETZ & KRINSLEY (1982) as well as VOS ET AL. (2014) and references therein described upturned plates as features <10 µm. In this study, however, larger structures (see Figure 23 B and Figure 24 C) with similar or identical characteristics have been observed. These are thin plates protruding from the grain surface and forming some sort of plateau. The plate edges are often smooth and modified by abrasion or chemical alteration (WOHLETZ & KRINSLEY, 1982; VOS ET AL., 2014). They are more frequently found on the grains of ashfall samples.

#23 Broken plates

Grain fragments formed by mechanical processes, which are either separated from the rest of the grain by microcracks or have been completely removed (see Figure 22 F and Figure 23 F). They are rare and were not found in a preferred deposition type.

#24 V-shaped percussion cracks

Depressions with a more or less V-shaped structure that can vary in size and depth and widen in one direction (WOHLETZ & KRINSLEY, 1982; MAHANEY, 2002; see Figure 22 B, D, Figure 23 D and Figure 27 C). According to VOS ET AL. (2014) they cannot reach sizes greater than 5 µm. Furthermore, they can quickly lose their typical shape due to abrasion and chemical influences. They show no specific orientation, as they result from random grain-grain collisions. Another form of formation is chemical solution in the areas of localized order or microlite development (WOHLETZ & KRINSLEY, 1982). According to VOS ET AL. (2014) they occur mainly in subaquatic high-energy regimes. Of course, their transport and depositional environment, like pyroclastic flows and/or surges, are also characterized by high energy.

4.5.3 Chemical features

The eight microtextures caused by chemical alteration are described and depicted below.

#25 Dissolution etching

Solution features may appear disordered or aligned along cleavage surfaces and fractures (MAHANEY, 2002). In addition, they can assume a wide variety of shapes and contribute significantly to changes of the grain surface (see Figure 24 and Figure 26 E). They often occur together with mineral precipitation on a grain surface (WOHLETZ & KRINSLEY, 1982).

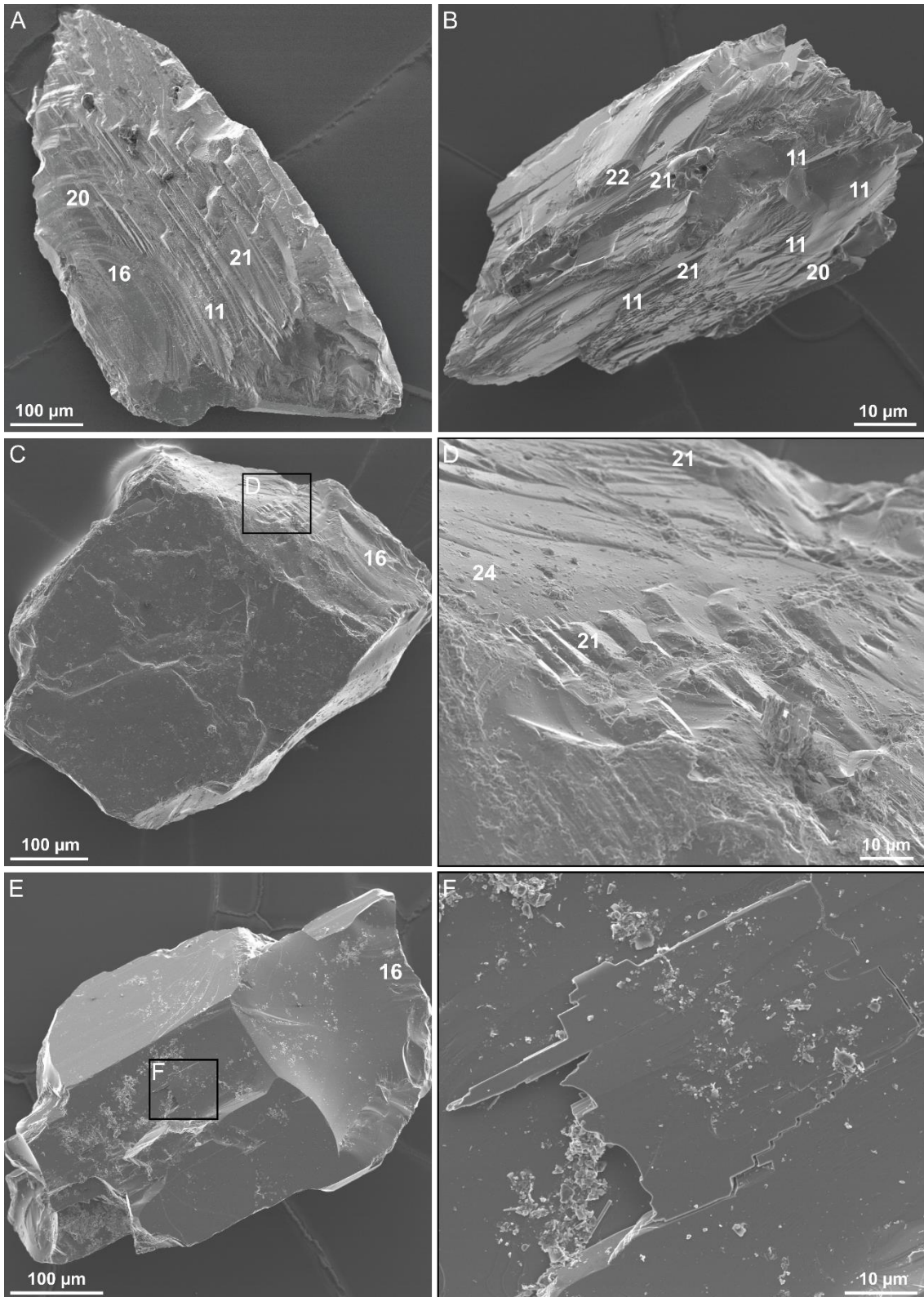


Figure 23: SEM micrographs of surface structures caused by mechanical stress. **A** – Plagioclase with pronounced arcuate (20) and straight steps (21) as well as a conchoidal fracture (16) and microcracks (11). MVO1702. **B** – Sharp angular features on a grain with an upturned plate (22) on top. Several microcracks (11) occur along cleavage surfaces. MVO1702. **C** – Plagioclase with a blocky shape and conchoidal fractures (16). MVO1704. **D** – Enlargement of the black box in photograph C. Note the straight steps (21) and the V-shaped percussion cracks (24). MVO1704. **E** – Blocky, curvy-planar planes show flat cleavage surfaces with conchoidal fractures (16) on a plagioclase. JR123-15-V. **F** – Detail of a broken plate from picture E with adhering particles. JR123-15-V. The numbers represent the microtextures in the text.

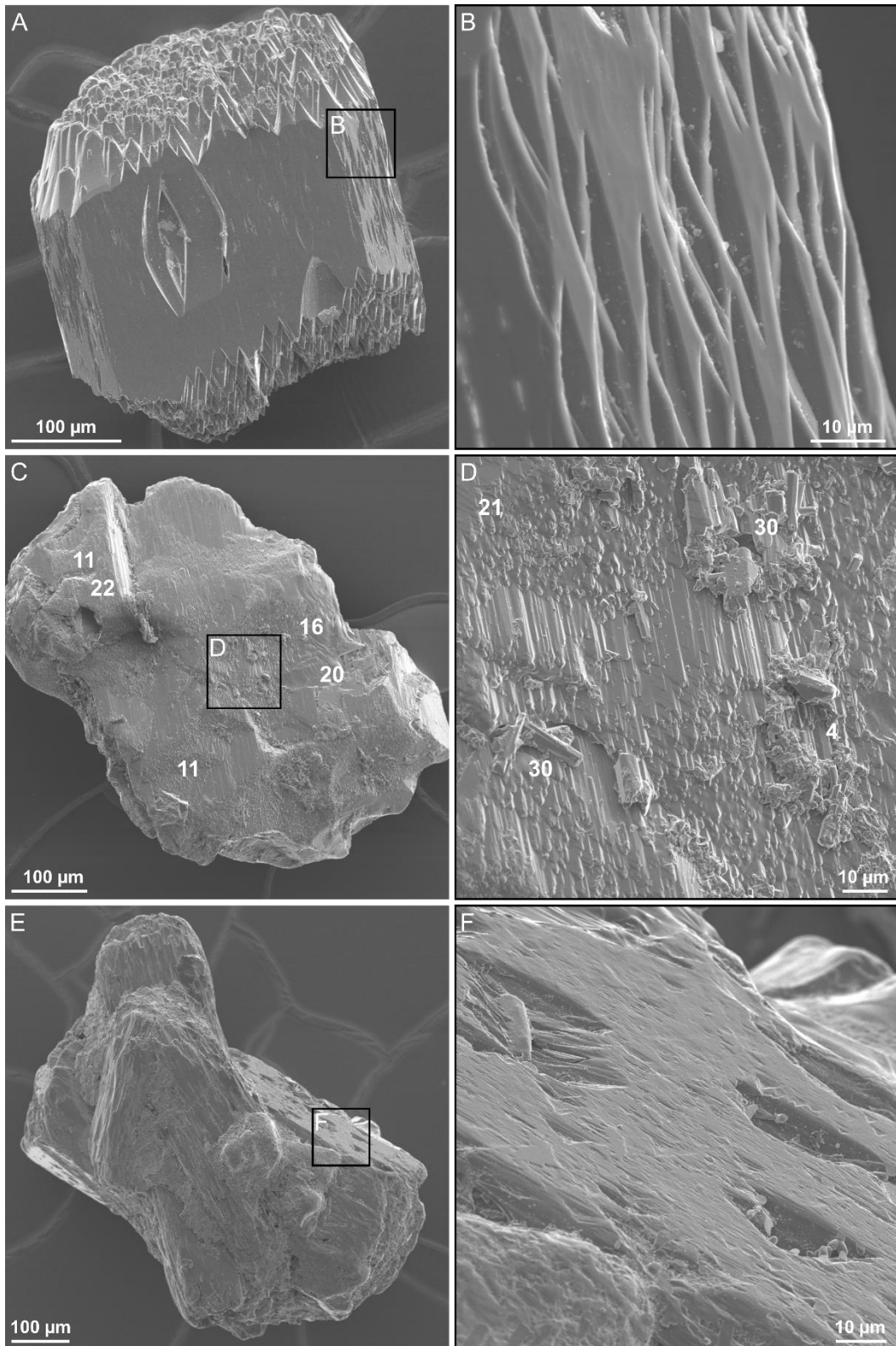


Figure 24: SEM micrographs of dissolution etching on grain surfaces. **A** – Etched pyroxene with typical needle-like features. BV1. **B** – Enlargement of the etched pyroxene surface in picture A. BV1. **C** – Angular grain with a ferrous coating and dissolution etching. Furthermore, there is an upturned plate (22) next to microcracks (11), conchoidal fractures (16), arcuate (20) and straight steps (21), which can be seen in the Enlargement of the grain surface in D. MVO1703. **D** – Enlargement of the etched grain surface and crystal growth (30). MVO1703. **E** – Twinned pyroxene crystals with etched surface features. Note that abrasion and chemical alteration led to grain rounding. BV3. **F** – Enlargement of the etched surface of the grain in picture E. BV3. The numbers represent the microtextures in the text.

#26 Vesicularity (glassy coating)

The surface textures vesicularity and glassy coating comprise all structures that can be associated with bubble clusters, vesicle remnants, secondary bubbles or the fine coating of glass over crystals (Figure 19 A, Figure 20 E, Figure 22 E, F, Figure 25, Figure 26 E, F and Figure 27 B). The vitreous coating, though, is by far the most common. The shape and size of the bubbles varies greatly. They are mostly spherical, but they can also be elongated, which is particularly noticeable in vitreous pyroclasts. The vesicles formed on the crystals have sharp edges and they resemble the wall fragments of bubbles that broke during fragmentation. Usually they are filled with the broken residues of the bubble walls due to agglutination or electrostatic charging (WOHLETZ & KRINSLEY, 1982). FISHER (1963) described the glassy overgrowth on the crystals as bubble-wall texture.

#27 Weathered surface

Weathering is characterized by modification of the surface as a result of chemical alteration (see Figure 19 C, D, Figure 20 B, C, Figure 21 A and Figure 26 C), whereby mainly acids cause typical etching patterns due to the crystal lattice (MAHANEY, 2002).

#28 Precipitation features

Mineral precipitation shows up through frosted, light diffused surfaces, like a ferrous skin formed on crystals by oxidation (see Figure 20 C, Figure 24 C and Figure 26 A).

#29 Dissolved crystals

Remnants of phenocrysts which have been removed from the surfaces of crystals or rock fragments (Figure 26 B). They are less common but occur more often in the offshore samples.

#30 Crystal growth

Crystals that form on the surfaces of clasts (lithic fragments, crystals) within an oversaturated environment (Figure 24 D, Figure 26 C, D, E and F). The type and shape of crystal growth can be very different. A remarkably high formation can be seen in the co-pyroclastic ash fall samples. These crystals were still formed in the magma chamber. An exception, however, are gypsum crystals, which formed especially in sample MVO1704, and can be considered as hydrothermal precipitation.

#31 Scaling

Crumbling of particles caused by disintegration of the grain surface, which in turn is caused by chemical alteration (see Figure 25 F and Figure 27 B).

#32 Pits

Pits vary in shape and size but are usually not larger than 10 μm (see Figure 27 A). These differences are linked to different chemical influences. Furthermore, pits can often be mixed up with remnants of mineral inclusions, which often occur as a linear fluid inclusion trail (VOS ET AL., 2014). They are represented in various forms in all specimens, but most often in Trant's and Spanish Point samples. They differ to #24 regarding to their origin, since the V-shaped percussion cracks are formed only by mechanical impacts.

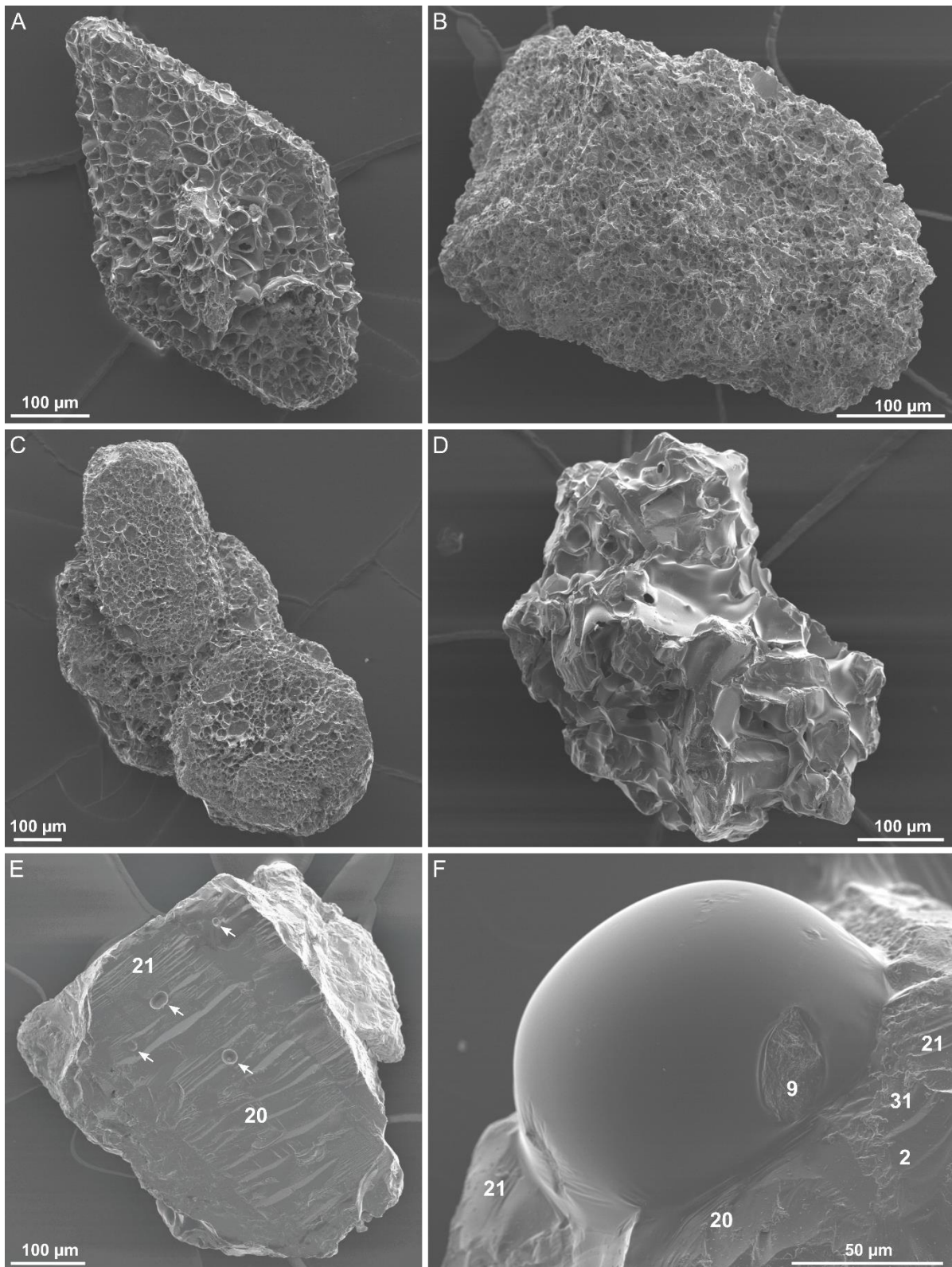


Figure 25: SEM micrographs showing vesicularity and glassy coating. **A** – Rhombic plagioclase with glassy coating. Note the large bubble remnants. MVO1701. **B** – Juvenile pumice pyroclast. MVO1701. **C** – Crystals enclosed in glassy coating. MVO1702. **D** – Juvenile vitric pyroclast enclosing large vesicles and showing in a few places fused skin. MVO1703. **E** – Blocky grain with straight (21) and arcuate steps (20). Note the secondary vesicles (arrows) which are randomly allocated on the grain surface. MVO290. **F** – Enlargement of a vesicle, that is not broken yet. Note the straight (21) and arcuate steps (20), scaling (31) and the impact crater (9) on the vesicle itself. MVO290. The numbers represent the microtextures in the text.

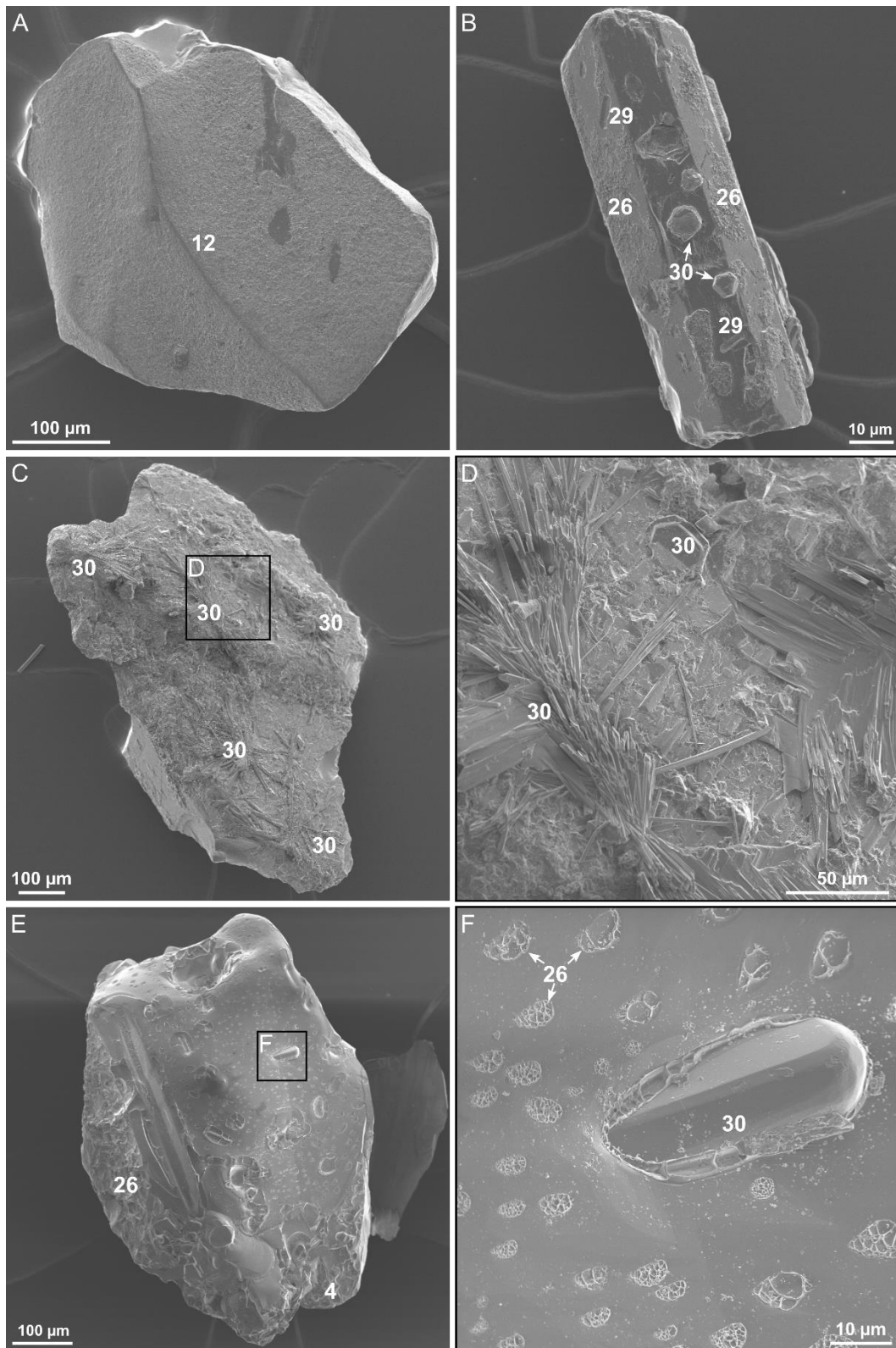


Figure 26: SEM micrographs of some chemical features on grain surfaces. **A** – A grain with ferrous precipitation coating and abrasion features (12). BV1. **B** – Column-shaped pyroxene showing dissolved crystals (29), crystal growth (30) and partly glassy overgrowth (26). **C** – Weathered clast with crystal growth (30). For details see D. MVO1703. **D** – Enlargement of the grain in C. Crystal growth (30) is visible and with the SEM-EDX it could be identified as gypsum. **E** – Rounded grain with dissolution etching and crystal growth as well as partly glassy overgrowth (26). JR123-23-V. **F** – Enlargement of the black box in E. Note the vesicular accumulations (26) distributed homogeneously on the surface. Furthermore, it has a crystal sticking out of the grain (30). JR123-23-V. The numbers represent the microtextures in the text.

4.5.4 Other features

#33 Elongated depressions

Elongated depressions (Figure 27 C) occur mainly in rounded grains and are characterized by elongated to dish shaped depressions. After VOS ET AL. (2014) they can reach dimensions from 20 to 250 μm and can be assigned to high-energetic transport conditions. In this case it can be associated with the deposits of pyroclastic density currents, or surges, as well as submarine turbidites since this type of microtextures is more frequently in the marine samples than in the ash fall deposits.

#34 Adhering particles

Adhering particles (see Figure 21 D, Figure 23 F and Figure 27 A) were observed on almost all examined grains, whereby size and shape are highly diverse. Since the investigated samples originate from a volcanic environment and some of them are volcanic ashes, it can be assumed that the particles are smaller dust particles which adhere to the coarser ash grains (HEIKEN & WOHLTZ, 1985). Furthermore, the particles can either be from the grain itself or stick to it due to collision with other grains. WOHLTZ

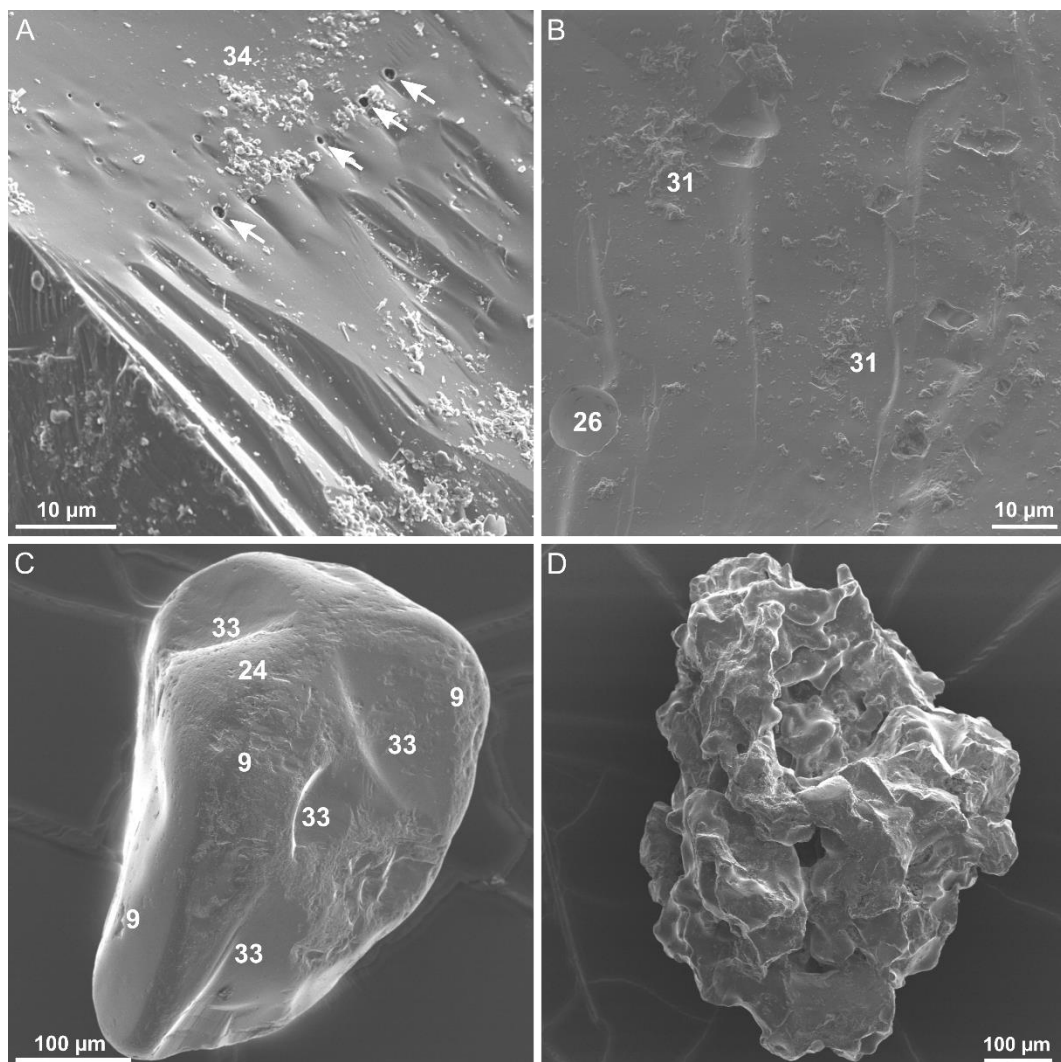


Figure 27: SEM micrographs of other features. **A** – Grain with adhering particles (34) and pits aligned in a row (arrows) which are interpreted as a fluid inclusion trail (Vos et al., 2014). JR123-15-V. **B** – Enlargement of a grain with remnants of secondary vesicles (26) and scaling (31). MVO290. **C** – Elongated depressions (33) on a rounded grain with several V-shaped percussion cracks (24) and craters (9). BV2. **D** – Vitric pyroclast with fused skin. BV1. The numbers represent the microtextures in the text.

& KRINSLEY (1982) mentioned as possible causes cohesiveness of wet surfaces on which small particles adhere and electrostatic charging due to breakage.

#35 Droplike or fused skin

HEIKEN & WOHLTZ (1985) described this surface texture for basaltic ash particles as fluidal texture and WOHLTZ & KRINSLEY (1982) showed melted-fused surfaces or fluidal forms of droplike textures (Figure 25 D and Figure 27 D). The vesicular ash particles have smooth, round surfaces despite having a high relief. HEIKEN & WOHLTZ (1985) suggested that a droplike or fused skin is formed in a liquid droplet by surface tension before it is cooled.

#36 Blocky, curvy-planar surfaces

The grains show planar to curvilinear faces that converge at nearly right angles (Figure 20 A, Figure 21 C, Figure 22 C, Figure 23 C, E and Figure 25 E). They are caused by the breaking of brittle, air-cooled lava, but can also occur in crystals that break along preferred cleavage. Blocky, curvy-planar surfaces are common in every sample.

It should be mentioned that only crystals were examined to identify microtextures on the surfaces. However, juvenile lava fragments were also considered, and the results showed that they were well suited for the estimation of grain shape (Figure 28). Further microtextures which could be recognized are mainly chemical features, whereas mechanical impacts could hardly be found.

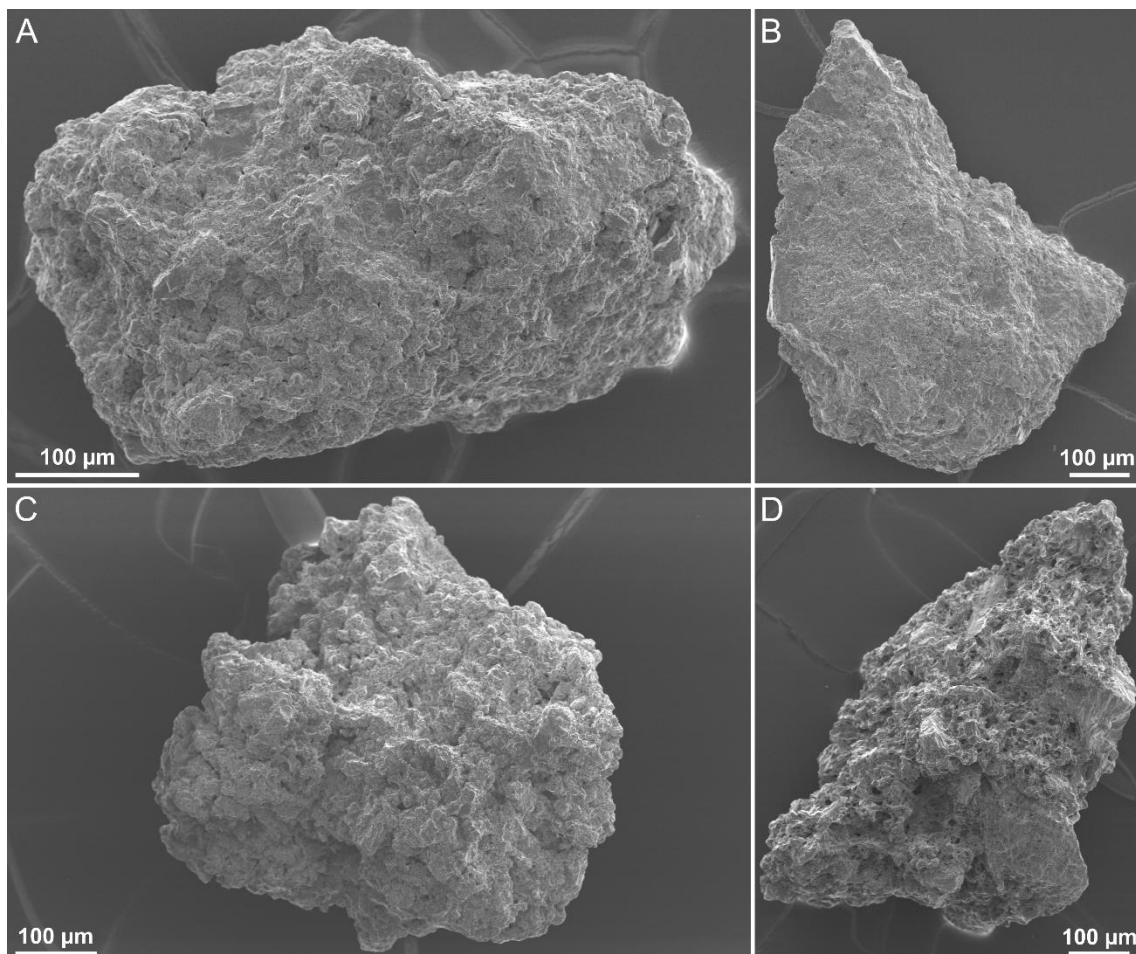


Figure 28: SEM micrographs of juvenile lava fragments. They were mainly used to distinguish the grain shape. **A** – Sample BV1. **B** – Sample Plym01. **C** – Sample Trant’s 1. **D** – Sample MVO1701.

Furthermore, SEM micrographs of the smaller grain sizes 63 – 100 μm and <63 μm were made to distinguish differences or similarities among the fractions (see Figure 29). The most obvious differences refer to the grain shape, which is predominantly angular. In addition, the blocky, curvy-shaped grains are frequently found in offshore samples, whereas in subaerial samples the vesicular grains are more common. The bubbles show shapes from almost roundish to elongated. However, in summary, it can be concluded that blocky, curvi-planar shapes occur more frequently than vesicular grains.

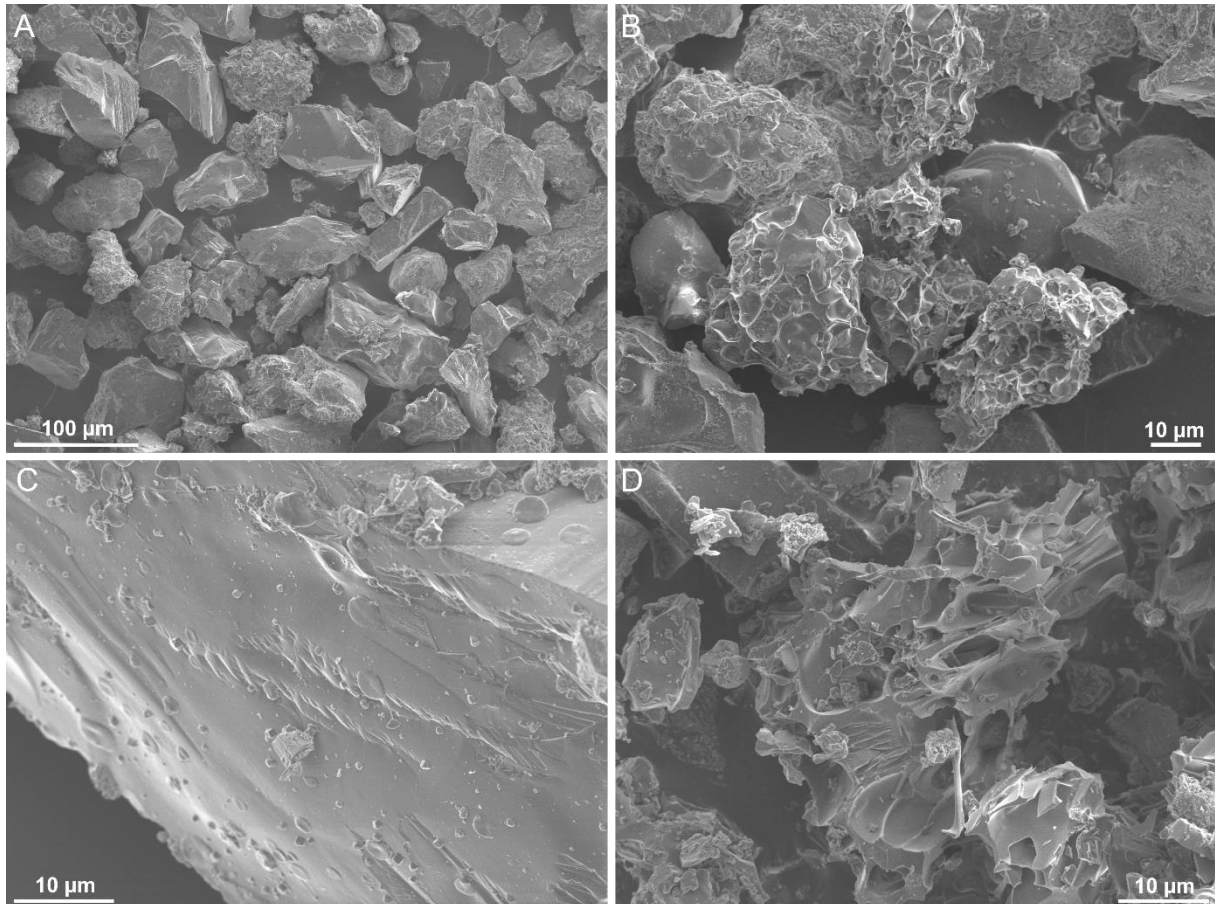


Figure 29: SEM micrographs of the grain size fractions 63 – 100 μm and < 63 μm . **A** – Sample JR123-23-V. **B** – Sample Spanish Point. **C** – Sample JR123-23-V. **D** – Sample MVO290.

The microtextures were subdivided into frequency ranges after BULL ET AL. (1987). This includes abundant (> 75%), common (25-75 %), present (2-25%) and absent (< 2%). Table 6 comprises the results of this frequency categorization. It provides an overview of the distribution of the individual microtextures of the samples. Note that some microtextures occur in almost every sample in a high amount, for example crater, chipped edges, conchoidal fractures, arcuate and straight steps, dissolution etching as well as blocky, curvy-planar surfaces. In addition, it is noticeable that most grains are angular and/or have a high relief. Whereas a low grain outline is especially common in the offshore and vulcanian explosion ashfall samples. In contrast, abrasion features, radial fractures, upturned plates, broken plates, V-shaped percussion cracks, scaling and droplike or fused skin occur only occasionally. Adhering particles are specifically associated with ashfall deposits and the samples from Trant`s and Spanish Point. Apart from that, no significant trend can be seen in the graph.

Table 6: Overview of the microtextures and their frequency subdivision after BULL ET AL. (1987). The offshore samples (blue), vulcanian ashfall samples (orange), co-pyroclastic ashfall samples (green), Belham Valley and Plymouth samples (yellow) and the Trant's and Spanish Point samples (grey) are categorized in abundant (> 75 %), common (25 - 75 %), present (2 - 25 %) and absent (< 2 %). The different colors should visualize the differences between the individual environments and the color code is from Table 4.

	Microtextures	#	Sample Groups													Trant's and Spanish Point				
			JR123-15-V	JR123-23-V	MVO1701	MVO1702	MVO 1703	MVO 1700	MVO1704	MVO1705	MVO290	BV1	BV2	BV3	Plym01	Plym02	Plym03	Trant's 1	Trant's 2	Spanish Point
Grain outline	Low	1	□	□	□	□	□	□	□	□	□	□	□	□	□	□	□	□	□	□
	Medium	2	■	■	■	■	■	■	■	■	■	■	■	■	■	■	■	■	■	■
	High	3	■	■	■	■	■	■	■	■	■	■	■	■	■	■	■	■	■	■
Relief	Low	4	□	□	□	□	□	□	□	□	□	□	□	□	□	□	□	□	□	□
	Medium	5	■	■	■	■	■	■	■	■	■	■	■	■	■	■	■	■	■	■
	High	6	■	■	■	■	■	■	■	■	■	■	■	■	■	■	■	■	■	■
Mechanical features	Flat cleavage surface	7	□	■	□	□	□	■	□	□	□	□	□	□	□	□	□	□	□	□
	Fresh surface	8	■	■	□	□	□	□	□	□	■	□	□	□	□	□	□	□	□	□
	Crater	9	■	■	■	■	■	■	■	■	■	■	■	■	■	■	■	■	■	■
	Sawtooth structure	10	□	□	□	□	□	□	□	□	□	□	□	□	□	□	□	□	□	□
	Microcracks	11	□	■	■	■	■	■	■	■	■	■	■	■	■	■	■	■	■	■
	Abrasion features	12	□	□	□	□	□	□	□	□	□	□	□	□	□	□	□	□	□	□
	Parallel ridges	13	■	■	□	□	□	□	□	□	■	□	□	□	□	□	□	□	□	□
	Grain rounding	14	■	■	■	■	■	■	■	■	■	■	■	■	■	■	■	■	■	■
	Chipped edges	15	■	■	■	■	■	■	■	■	■	■	■	■	■	■	■	■	■	■
	Conchoidal fractures	16	■	■	■	■	■	■	■	■	■	■	■	■	■	■	■	■	■	■
	Grooves/scratches	17	■	□	□	□	□	□	□	□	□	□	□	□	□	□	□	□	□	□
	Radial fractures	18	□	□	□	□	□	□	□	□	□	□	□	□	□	□	□	□	□	□
	Sharp angular features	19	□	□	□	■	□	□	□	□	□	□	□	□	□	□	□	□	□	□
	Arcuate steps	20	■	■	■	■	■	■	■	■	■	■	■	■	■	■	■	■	■	■
	Straight steps	21	■	■	■	■	■	■	■	■	■	■	■	■	■	■	■	■	■	■
	Upturned plates	22	□	□	□	□	□	□	□	□	□	□	□	□	□	□	□	□	□	□
	Broken plates	23	□	□	□	□	□	□	□	□	□	□	□	□	□	□	□	□	□	□
V-shaped percussion cracks	24	□	□	□	□	□	□	□	□	□	□	□	□	□	□	□	□	□	□	
Chemical features	Dissolution etching	25	■	■	■	■	■	■	■	■	■	■	■	■	■	■	■	■	■	■
	Vesicularity (Glassy coating)	26	□	■	■	■	■	■	■	■	■	■	■	■	■	■	■	■	■	■
	Weathered surface	27	■	□	□	□	■	■	■	■	■	■	■	■	■	■	■	■	■	■
	Precipitation features	28	□	□	□	□	□	□	□	□	□	□	□	□	□	□	□	□	□	□
	Dissolved crystals	29	□	□	□	□	□	□	□	□	□	□	□	□	□	□	□	□	□	□
	Crystal growth	30	□	□	□	□	□	□	□	□	□	□	□	□	□	□	□	□	□	□
	Scaling	31	□	□	□	□	□	□	□	□	□	□	□	□	□	□	□	□	□	□
	Pits	32	□	■	■	■	■	■	■	■	■	■	■	■	■	■	■	■	■	■
Other features	Elongated depressions	33	□	□	□	□	□	□	□	□	□	□	□	□	□	□	□	□	□	□
	Adhering particles	34	■	■	■	■	■	■	■	■	■	■	■	■	■	■	■	■	■	■
	Droplike or fused skin	35	□	□	□	□	□	□	□	□	□	□	□	□	□	□	□	□	□	□
	Blocky, curvy-planar surfaces	36	■	■	■	■	■	■	■	■	■	■	■	■	■	■	■	■	■	■

■ Abundant (> 75%) ■ Common (25 - 75%) □ Present (2 - 25%) □ Absent (< 2%)

5. DISCUSSION

In this chapter the results will be summarized and interpreted. In addition, the identified microtextures will be attributed to their formation mechanisms. These include eruption mechanisms, transport processes as well as deposition and weathering features (see Table 7). According to HEIKEN (1972), ash morphology is primarily related to vesicle shapes evolving in the magma. Furthermore, it is said that andesitic ashes may consist to a large extent of rock and crystalline fragments and in this case the appearance of the particles depends on the mechanical rock properties (HEIKEN, 1972). The description of the ashes of andesitic composition according to HEIKEN & WOHLTZ (1985) coincides with the results of this work. During the eruption, phenocrysts break out of the rock fragment due to high energies. However, this confirms the fact that a large part of the samples consists of isolated crystals. Furthermore, angular crystals are common, whereby the surface structures relate to the cleavage patterns of the individual minerals. The variety of rock fragments results from the different products which were ejected and deposited, and they are mostly round to angular. The majority of the rock composition is andesitic, as reflected in the samples.

5.1 Granulometry

The particle size analysis can be used to identify some significant differences between the individual sample groups (Figure 30). First and foremost, it should be mentioned that the offshore samples JR123-15-V and JR123-23-V show the best sorting of all samples and they consist of the highest amount of very coarse sand due to the sampling location in the coarser areas of the pyroclastic flow deposits offshore Montserrat. Sample JR123-23-V is part of the pyroclastic lobe and JR123-15-V is assigned to the finer grained granular sediment density current considering the step-like geometry of the deposits

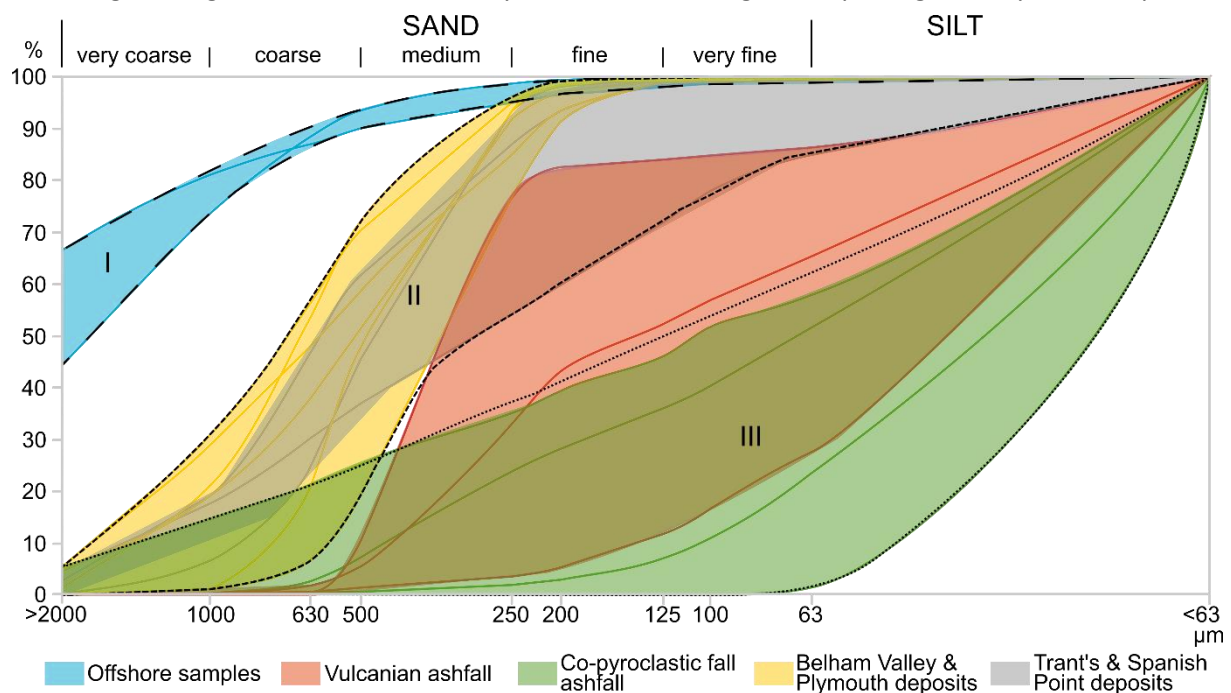


Figure 30: The grain size distribution of all samples is depicted and a clear differentiation between the individual sample groups can be achieved. Zone I (coarse dashed line) denotes the offshore samples, zone II (fine dashed line) comprises the beach samples of Belham Valley, Plymouth, Trant's and Spanish Point and zone III (dotted line) includes the Vulcanian and co-pyroclastic ashfall samples. The ranges were partially generalized and an outlier of the ashfall samples is not included. The colour code is adopted from Table 4.

(see chapter 3.1). They were summarized in zone I. Zone II comprises the samples of Belham Valley, Plymouth, Trant's and Spanish Point that were collected near the beach and have been affected by various volcanic and weather events (yellow and grey areas Figure 30). Sample Trant's 2 was sampled from a block-and-ash flow deposit. The different volcanic and climatic influences lead to a wide spectrum of sorting in the specimens, which ranges from moderately well sorted to very poorly sorted. In contrast to this, almost all ashfall samples (MVO290 and MVO1700-1705; see the red and green areas in Figure 30) are concentrated in the smaller grain size fractions (< 0.125 mm) and are poorly sorted. An exception is sample MVO1703, which represents the upper grading curve in Figure 30. All samples are summarized to zone III except sample MVO1703 that is interpreted as an outlier.

5.2 Microtextures

By describing the microtextures in chapter 4.5, they could be assigned to certain characteristics, which were based on the classification of VOS ET AL. (2014). These were relief, grain outline, mechanical, chemical and other features. Figure 30 provides information on the occurrence and frequency of the microtextures in the different sample groups. Some of the surface structures (like crater, conchoidal fractures with arcuate and straight steps and blocky, curvi-planar grain shapes) are particularly common and are caused by mechanical influences. Furthermore, dissolution etching and vesicularity form the grain surface significantly. By assigning the microtextures to a process of formation, the classification according to WOHLLETZ (1983) was applied, which consists of eruption mechanisms, transport and deposition characteristics (Table 7).

5.2.1 Eruption mechanisms

CIONI ET AL. (1992) summarized some chemical parameters occurring in the volcanic vent that can influence morphological characteristics greatly. These include the chemical composition as well as temperature, viscosity, volatile content and the ascent rate of the magma. Furthermore, external water and transport mechanisms like dense or diluted flow together with the movement in convective systems can have a large impact on the eruption dynamics (CIONI ET AL., 1992). Some surface structures, like drop-like or fused skin and blocky shapes, that are related to hydrovolcanism also occur in some of the analysed samples. Blocky shapes generate after rapid chilling of the quenching magma and the resulting thermal contraction (HEIKEN & WOHLLETZ, 1985; CIONI ET AL., 1992). By the investigation of grain sizes smaller 125 μm it could be determined that the blocky-shaped grains increase with smaller grain size and the amount of vesicular grains decreases.

According to FISHER (1963), abrasion on glass and crystals already occurs inside the vent after solidification and fragmentation. Furthermore, he suggested that the cushioning effect of air reduces abrasion due to less grain-to-grain impacts. FISHER (1963) also described bubble-wall textures for the first time on completely or partially glass enclosed crystals.

5.2.2 Transport processes

The majority of microtextures, caused by mechanical stress, are generated during transport. MANGA ET AL. (2011) described the abrasion and comminution of particles during the transport in pyroclastic density currents due to grain-to-grain and grain-to-substrate contacts. It is important to differentiate between abrasion and breakup, as one results in rounding and the other in angularity (MANGA ET AL., 2011). Furthermore, it is expected that with greater distance the particles become constantly rounder

in density currents, however, the material of the offshore samples which was transported furthest does not show the expected effect. According to MANGA ET AL. (2011) it can be a result of different genetic processes and transport dynamics. But not only the shape of a clast can provide information about abrasion, also the amount of single crystals is an indicator (FREUND & SCHMINCKE, 1992; MANGA ET AL., 2011). They represent the particles that were broken out of the rock fragment during mechanical stress. This can happen both during the ascent of the magma in the vent and through grain-grain and grain-substrate contact in a pyroclastic flow or surge. The analysed samples contained a large amount of single crystals or crystal fragments (especially plagioclase).

The majority of the grains show medium to high grain outline, what is caused by the transport of the particles in pyroclastic falls, block-and-ash flows, surges, and submarine mass flows. Other microtextures that may have been caused by mechanical processes during transport are for example grooves and scratches, steplike features (arcuate and straight steps), microcracks, chipped edges, conchoidal fractures, sharp angular features and V-shaped percussion cracks. Specific microtextures caused by the interaction of hot pyroclastic currents with seawater could not be identified as expected.

5.2.3 Deposition

A well-established example of the deposition of mass movements due to volcanic activity in the sea is the dome collapse in July 2003 on Montserrat, which has been intensively studied by TROFIMOV ET AL. (2006, 2008). According to their research a stepped deposition geometry of the mass flow could be identified. This in turn implies that first the coarse particles were deposited, followed by slightly finer particles consisting of sand and granules and the finest particles forming a wide fan of sandy turbidites (TROFIMOV ET AL., 2008). The samples JR123-15-V and JR123-23-V are collected from different parts of the mass flow as described before. Expected variations on grain surfaces of the subaquatic samples compared to the subaerial deposits in terms of weathering susceptibility due to subaquatic deposition are scarcely detectable. There are only a few grains, which were affected more strongly by chemical weathering. As a result, the mass movements carry along grains of older eruptions, which have already been influenced by alteration, during their transport and deposit them together with the juvenile material.

Not only the submarine but also the subaerial samples can be affected by chemical influences, hydrothermal activity, alteration and weathering processes. The surfaces of the grains become increasingly rough and the relief higher. Table 6 shows that most of the grains are altered by dissolution effects. Crystals can be dissolved by etching but can also grow on the grains as secondary formations. Due to breakage and abrasion of the glassy coated crystals during transport, the vesicles can be filled with the remnants of the bubble walls. These adhering particles are glued to the grains as a result of adhesive forces.

Since the deposits are quite recent, the mechanical effects have a greater impact on the surface modifications of the grains than the weathering processes. Furthermore, no significant differences between subaerial and submarine deposits could be identified. However, a possible explanation could be that the explosions occurring after the collision of the pyroclastic flow with the seawater has no great effect on the individual grains. Grains with fused skin, which would be conceivable as a result of such a phenomenon, also occur in the subaerial samples. However, it should be mentioned that in both offshore samples the blocky shaped grains, which are typical for hydrovolcanism, are by far the most common. To round off the results of this study, the data were summarized according to WOHLTZ (1983)

in Table 7. Furthermore, an overview of all microtextures with the best representing image of each surface structure is given in Appendix 8.

Table 7: Overview of the microtextures observed in the studied samples, modified after the classification of WOHLTZ (1983). Vesicle fillings and hydration cracks were not considered as single microtextures but are assigned to the group of vesicularity and microcracks. Note that most of the features form during transport. The features marked in light grey were not distinguished as individual microtextures but occur on the grains, and the surface textures marked in blue may originate from different processes (see Table 6).

Eruptive Mechanism	Transport	Deposition & Alteration
Blocky, curvi-planar surfaces	Grain rounding	Vesicle fillings
Vesicularity (glassy coating)	Grooves, scratches & ridges	Hydration cracks
Droplike or fused skin	Arcuate & straight steps	Dissolution etching
Adhering particles	Conchoidal fractures	Precipitation features
	Chipped edges	Weathered surface
	Microcracks	Crystal growth
	Upturned plates	Dissolved crystals
	Flat cleavage surface	Pits
	V-shape percussion cracks	Scaling
	Elongated depressions	Abrasion features
	Broken plates	
	Fresh surface	
	Crater	
	Sawtooth structure	
	Radial fractures	
	Sharp angular features	

6. CONCLUSION

Montserrat is a small island of the Lesser Antilles in the Caribbean Sea that became a scientific hotspot during volcanic activity in the 90s and 2000s. One objective of this study was to investigate microtextures on grains of different types of pyroclastic deposits. Further, there was to find out whether differences can be detected when volcanically generated grains are deposited as ash fall or by mass movements such as pyroclastic flows, block-and-ash flows, surges or submarine mass movements. It had to be clarified whether the collision of a pyroclastic flow with seawater and the resulting explosion caused specific surface structures. To round off the investigations of the microtextures, a grain size and grain shape analysis as well as microscopy and a point counting measurement were realized.

Differences could be identified in the grain size analysis, whereby the offshore samples showed the best sorting, presumably due to the submarine transport. All other samples were only moderately to poorly sorted. It was possible to divide the samples into three zones, differentiating the different sample groups (offshore samples, ashfall samples, reworked beach samples) according to grain size distributions. Grain shape analysis did not reveal any differences between the individual sample groups. But it demonstrated that most of the grains were rounded to subrounded due to the calculations on the thin sections. However, the visual impression on the individual grains suggests a larger number of angular grains. In the mineralogical composition, as well, differences were scarcely noticeable. Only three samples (BV2, BV3 and Trant's 2) showed a varying content of plagioclase, pyroxenes and the opaque phase magnetite. Apart from that, the samples consist mainly of plagioclase and various types of rock fragments. These can be divided into juvenile lava fragments (crystalline or vesicular) and slightly altered rock fragments that were carried along during eruption and transport. Further mineral phases are amphibole, especially hornblende, orthopyroxene and clinopyroxene. The offshore samples and some nearshore specimens also contain biogenic fragments.

All 36 microtextures identified on the grains could be compared with previous studies and classified into distinct formation processes. These include eruption mechanisms, transport processes and deposition phenomena. Thus, it could be shown that the majority of the microtextures were formed by mechanical features caused by eruption or transport processes, which can be explained by the high energies released thereby. After deposition, the pyroclasts can be altered by weathering and chemical imprinting. The greatest impact is probably associated with hydrothermal activity in the active areas of Soufriere Hills. Chemically overprinted grains can be transported downhill by pyroclastic flows and surges, block-and-ash flows, or lahars and mixed with juvenile components. Furthermore, it should be mentioned that the Lesser Antilles are also affected by extreme weather events (e.g. hurricanes) and that sediment repositioning and changes in grain surface textures can occur anytime.

Since in this work mainly single grains (50 per sample) were considered for analysis, a larger number of grains could give more significant results. Furthermore, more samples (especially submarine) and sample groups as well as a more precise subdivision into different deposition types (for example pyroclastic flows, surges, lahars, block-and-ash flows) can provide stronger variations in the results.

7. REFERENCES

- ALLEN, C.D. (2017): Landscapes and Landforms of the Lesser Antilles, Springer International Publishing AG, x + 321 pp.
- BAXTER, P.J.; SEARL, A.S.; COWIE, H.A.; JARVIS, D. & HORWELL, C.J. (2014): Chapter 22 Evaluating the respiratory health risks of volcanic ash at the eruption of the Soufrière Hills Volcano, Montserrat, 1995 to 2010, *In*: WADGE, G.; ROBERTSON, G.E.A. & VOIGHT, B. (Eds.) (2014): The Eruption of Soufriere Hills Volcano, Montserrat from 2000 to 2010, Geological Society, London, Memoirs 39, pp. 407–425
- BIEDERMAN, M.W. (1962): Destruction of shoreline environments in New Jersey, *In*: Journal of Sedimentary Research 32, pp. 181–200
- BLOTT, S.J. & PYE, K. (2001): GRADISTAT: a grain size distribution and statistics package for the analysis of unconsolidated sediments, *In*: Earth Surface Processes and Landforms 26, pp. 1237–1248
- Bonadonna, C.; Mayberry, G. C.; Calder, E. S.; Sparks, R.S.J.; Choux, C.; Jackson, P. Lejeune, A. M.; Loughlin, S. C.; Norton, G. E.; Rose, W.I., Ryan, G. & Young, S.R. (2002): Tephra fallout in the eruption of Soufrière Hills Volcano, Montserrat, *In*: DRUITT, T.H. & KOKELAAR, B.P. (Eds.) (2002): The Eruption of Soufrière Hills Volcano, Montserrat, from 1995 to 1999, Geological Society, London, Memoirs 21, pp. 483-516
- BOUYSE, P. (1984): The Lesser Antilles Island arc: structure and geodynamic evolution (DSDP, Leg 78A), *In*: Initial reports DSDP, Leg 78A, from San Juan, Puerto Rico, pp. 83–103
- BULL, G.W.; GOUDIE, A.S.; PRICE WILLIAMS, D. & WATSON, A. (1987): Chapter 1-2 Colluvium: A scanning electron microscope analysis of a neglected sediment type. *In*: MARSHALL, J. R. (1987): Clastic Particles. Scanning electron microscopy and shape analysis of sedimentary and volcanic clasts, New York, Berkshire, Victoria, Ontario, Van Nostrand Reinhold Company Inc, pp. 16–35
- BURNS, F.A.; BONADONNA, C.; PIOLI, L.; COLE, P.D. & STINTON, A. (2017): Ash aggregation during the 11 February 2010 partial dome collapse of the Soufrière Hills Volcano, Montserrat, *In*: Journal of Volcanology and Geothermal Research 335, pp. 92–112
- CHRISTOPHER, T.E.; HUMPHREYS, M.C.S.; BARCLAY, J.; GENAREAU, K.; DE ANGELIS, S.M.H.; PLAIL, M. & DONOVAN, A. (2014): Chapter 17 Petrological and geochemical variation during the Soufrière Hills eruption, 1995 to 2010, *In*: WADGE, G.; ROBERTSON, G.E.A. & VOIGHT, B. (Eds.) (2014): The Eruption of Soufriere Hills Volcano, Montserrat from 2000 to 2010, Geological Society, London, Memoirs 39, pp. 317–342
- CIONI, R.; SBRANA, A. & VECCI, R. (1992): Morphologic features of juvenile pyroclasts from magmatic and phreatomagmatic deposits of Vesuvius, *In*: Journal of Volcanology and Geothermal Research 51 (1-2), pp. 61–78
- CLARKE, A.B.; NERI, A.; VOIGHT, B.; MACEDONIO, G. & DRUITT, T.H. (2002): Computational modelling of the transient dynamics of the August 1997 Vulcanian explosions at Soufrière Hills Volcano, Montserrat: influence of initial conduit conditions on near-vent pyroclastic dispersal, *In*: DRUITT, T. H. & KOKELAAR, B.P. (Eds.) (2002): The Eruption of Soufrière Hills Volcano, Montserrat, from 1995 to 1999, Geological Society, London, Memoirs 21, pp. 319-348
- CLARKE, A.B; ESPOSTI ONGARO, T. & BELOUSOV, A. (2015): Chapter 28 Vulcanian Eruptions. *In*: The Encyclopedia of Volcanoes, 2nd revised edition, San Diego: Elsevier Science Publishing Co Inc, pp. 505–518
- COLE, R.B. & DeCELLES, P.G. (1991): Subaerial to submarine transitions in early Miocene pyroclastic flow deposits, southern San Joaquin basin, California, *In*: Geological Society of America Bulletin 103, pp. 221–236

- COLE, P.D.; CALDER, E.S.; DRUITT, T.H.; HOBLITT, R.; ROBERTSON, R.; SPARKS, R.S.J. & YOUNG, S.R. (1998): Pyroclastic flows generated by gravitational instability of the 1996-97 lava dome of Soufrière Hills Volcano, Montserrat, *In: Geophysical Research Letters* 25 (18), pp. 3425–3428
- d-maps.com (2018): Landkarte Zentralamerika, online: https://d-maps.com/carte.php?num_car=1389&lang=de
last checked: 16.11.2018
- DEPLUS, C.; LE FRIANT, A.; BOUDON, G.; KOMOROWSKI, J.-C.; VILLEMANT, B.; HARFORD, C.; SÉGOUFIN, J.; CHEMINÉE, J.-L. (2001): Submarine evidence for large-scale debris avalanches in the Lesser Antilles Arc, *In: Earth and Planetary Science Letters* 192 (2), pp. 145–157
- DEVINE, J.D.; MURPHY, M.D.; RUTHERFORD, M.J.; BARCLAY, J.; SPARKS, R.S.J.; CARROLL, M.R.; YOUNG, S.R. & GARDNER, J.E. (1998): Petrologic evidence for pressure-temperature conditions, and recent reheating, of andesitic magma erupting at the Soufriere Hills Volcano, Montserrat, W.I, *In: Geophysical Research Letters* 25 (19), pp. 3669–3672
- DRUITT, T.H. & KOKELAAR, B.P. (Eds.) (2002): The Eruption of Soufrière Hills Volcano, Montserrat, from 1995 to 1999, Geological Society, London, Memoirs 21
- DRUITT, T.H.; YOUNG, S.R.; BAPTIE, B.; BONADONNA, C.; CALDER, E.S.; CLARKE, A.B.; COLE, P.D.; HARFORD, C.L.; HERD, R.A.; LUCKETT, R.; RYAN, G. & VOIGHT, B (2002): Episodes of cyclic Vulcanian explosive activity with fountain collapse at Soufrière Hills Volcano, Montserrat, *In: DRUITT, T.H. & KOKELAAR, B.P. (Eds.) (2002): The Eruption of Soufrière Hills Volcano, Montserrat, from 1995 to 1999, Geological Society, London, Memoirs 21, pp. 281–306*
- EDMONDS, M. & HERD, R.A. (2005): Inland-directed base surge generated by the explosive interaction of pyroclastic flows and seawater at Soufrière Hills volcano, Montserrat, *In: Geology* 33 (4), pp. 245–248
- EDMONDS, M.; KOHN, S. C.; HAURI, E.H.; HUMPHREYS, M.C.S. & CASSIDY, M. (2016): Extensive, water-rich magma reservoir beneath southern Montserrat, *In: Lithos* 252-253, pp. 216–233
- FISHER, R.V. (1963): Maximum Size, Median Diameter, and Sorting of Tephra, *In: Journal of Geophysical Research* 69 (2), pp. 341–355
- FOLK, R.L. & WARD, W.C. (1957): Brazos River bar: a study in the significance of grain size parameters, *In: Journal of Sedimentary Petrology* 27 (1), pp. 3–26
- FRANCIS, P. & OPPENHEIMER, C. (Eds.) (2004): *Volcanoes*, 2nd edition, Oxford, Oxford University Press, 536 pp.
- FREUNDT, A. (2003): Entrance of hot pyroclastic flows into the sea: experimental observations, *In: Bulletin of Volcanology* 65, pp. 144–164
- FREUNDT, A.; SCHMINCKE, H.-U. (1992): Abrasion in pyroclastic flows, *In: Geologische Rundschau* 81 (2), pp. 383–389
- FRIEDMAN, G.M. & SANDERS, J.E. (1978): *Principles of Sedimentology*, New York, Wiley, 792 pp.
- HARFORD, C.L.; PRINGLE, M.S., SPARKS, R.S.J. & YOUNG, S.R. (2002): The volcanic evolution of Montserrat using ⁴⁰Ar/³⁹Ar geochronology, *In: DRUITT, T.H. & KOKELAAR, B.P. (Eds.) (2002): The Eruption of Soufrière Hills Volcano, Montserrat, from 1995 to 1999, Geological Society, London, Memoirs 21, pp. 93–113*
- HART, K.; CAREY, S.; SIGURDSSON, H.; SPARKS, R.S.J. & ROBERTSON, R.E.A. (2004): Discharge of pyroclastic flows into the sea during the 1996-1998 eruptions of the Soufrière Hills volcano, Montserrat, *In: Bulletin of Volcanology* 66 (7), pp. 599–614
- HATTER, S.J.; PALMER, M.R.; GERON, T.M.; TAYLOR, R.N.; COLE, P.D.; BARFOD, D.N. & COUSSENS, M. (2018): The Evolution of the Silver Hills Volcanic Center, and Revised ⁴⁰Ar/³⁹Ar Geochronology of Montserrat, Lesser Antilles, With Implications for Island Arc Volcanism, *In: Geochemistry, Geophysics, Geosystems* 19 (2), pp. 427–452

- HAUTMANN, S.; GOTSMANN, J.; CAMACHO, A.G.; VAN CAMP, M. & FOURNIER, N. (2014): Chapter 14 Continuous and campaign-style gravimetric investigations on Montserrat 2006 to 2009, *In: Geological Society, London, Memoirs* 39 (1), pp. 241–251
- HEIKEN, G. (1972): Morphology and Petrography of Volcanic Ashes, *In: Geological Society of America Bulletin* 83, pp. 1961–1988
- HEIKEN, G. & WOHLETT, K. (1985): *Volcanic Ash*, Berkeley, Los Angeles, London: University of California Press, x + 246 pp.
- HIGGS, R. (1979): Quartz-Grain Surface Features of Mesozoic-Cenozoic Sands from the Labrador and Western Greenland Continental Margins, *In: Journal of Sedimentary Research* 49 (2), pp. 599–610
- INMAN, D.L. (1949): Sorting of sediments in the light of fluid mechanics, *In: Journal of Sedimentary Petrology* 19 (2), pp. 51–70
- KARSTENS, J.; CRUTCHLEY, G.J.; BERNDT, C.; TALLING, P.J.; WATT, S.F.L.; HÜHNERBACH, V.; LEFRIANT, A.; LEBAS, E. & TROFIMOV, J. (2013): Emplacement of pyroclastic deposits offshore Montserrat: Insights from 3D seismic data, *In: Journal of Volcanology and Geothermal Research* 257, pp. 1–11
- KOKELAAR, B.P. (2002): Setting, chronology and consequences of the eruption of Soufrière Hills Volcano, Montserrat (1995–1999), *In: DRUITT, T.H. & KOKELAAR, B.P. (Eds.) (2002): The Eruption of Soufrière Hills Volcano, Montserrat, from 1995 to 1999*, Geological Society, London, Memoirs 21, pp. 1–43
- KRAGELSKII, I.V. (1965): *Friciton and Wear*, London: Butterworths, 225 pp.
- KRINSLEY, D.H. & DONAHUE, J. (1968): Environmental interpretation of sand grain surface textures by electron microscopy, *In: Geological Society of America Bulletin* 79 (6), pp. 743–748
- KRINSLEY, D.H. & DOORNKAMP, J.C. (1973): *Atlas of Quartz Sand Surface Textures*, Cambridge: Cambridge University Press, 102 pp.
- KRINSLEY, D.H. & FUNNELL, B.M. (1965): Environmental history of quartz sand grains from the Lower and Middle Pleistocene of Norfolk, England, *In: Quarterly Journal of the Geological Society* 121 (1–4), pp. 435–456
- KRINSLEY, D.H. & TAKAHASHI, T. (1962a): Applications of electron microscopy to geology, *In: Transactions of the New York Academy of Sciences* 25, pp. 3–22
- KRINSLEY, D.H. & TAKAHASHI, T. (1962b): Surface textures of sand grains: an application of electron microscopy, *In: Science* (135), pp. 923–925
- KRINSLEY, D.H. & TAKAHASHI, T. (1962c): Surface textures of sand grains - an application of electron microscopy: Glaciation, *In: Science* 138, pp. 1262–1264
- KRUMBEIN, W.C. (1934): Size frequency distributions of sediments, *In: Journal of Sedimentary Petrography* 4 (2), pp. 65–77
- KRUMBEIN, W.C. & PETTIJOHN, F.J. (1938): *Manual of sedimentary petrography*, New York: D. Appleton-Century Company
- LE FRIANT, A.; HARFORD, C. L.; DEPLUS, C.; BOUDON, G.; SPARKS, R.S.J.; HERD, R.A. & KOMOROWSKI, J.C. (2004): Geomorphological evolution of Montserrat (West Indies): importance of flank collapse and erosional processes, *In: Journal of the Geological Society* 161 (1), pp. 147–160
- LE FRIANT, A.; ISHIZUKA, O.; BOUDON, G.; PALMER, M. R.; TALLING, P. J.; VILLEMANT, B.; ADACHI, T.; ALJAHDALI, M.; BREITKREUZ, C.; BRUNET, M.; CARON, B.; COUSSENS, M.; DEPLUS, C.; ENDO, D.; FEUILLET, N.; FRAAS, A.J.; FUJINAWA, A.; HART, M.B.; HATFIELD, R.G.; HORNBAACH, M.; JUTZELER, M.; KATAOKA, K.S.; KOMOROWSKI, J.-C.; LEBAS, E.; LAFUERZA, S.; MAENO, F.; MANGA, M.; MARTÍNEZ-COLÓN, M.; MCCANTA, M.; MORGAN, S.; SAITO, T.; SLAGLE, A.; SPARKS, S.; STINTON, A.; STRONCIK, N.; SUBRAMANYAM, K.S.V.;

- TAMURA, Y.; TROFIMOV, J.; VOIGHT, B.; WALL-PALMER, D.; WANG, F. & WATT, S.F.L. (2015): Submarine record of volcanic island construction and collapse in the Lesser Antilles arc: First scientific drilling of submarine volcanic island landslides by IODP Expedition 340, *In: Geochemistry, Geophysics, Geosystems* 16 (2), pp. 420–442
- LE RIBAUT, L. (1977): *L'exoscopie des quartz*, Masson, Paris, 150 pp.
- LOUGHLIN, S.C.; LUCKETT, R.; RYAN, G.; CHRISTOPHER, T.; HARDS, V.; ANGELIS, S. DE; JONES, L. & STRUTT, M. (2010): An overview of lava dome evolution, dome collapse and cyclicity at Soufrière Hills Volcano, Montserrat, 2005-2007, *In: Geophysical Research Letters* 37 (19), L00E16
- MACDONALD, R.; HAWKESWORTH, C.J. & HEATH, E. (2000): The Lesser Antilles volcanic chain: a study in arc magmatism, *In: Earth-Science Reviews* 49 (1-4), pp. 1–76
- MAHANEY, W.C. (2002): *Atlas of Sand Grain Surface Textures and Applications*, New York, Oxford University Press, 256 pp.
- MAHANEY, W.C. & KALM, V. (2000): Comparative scanning electron microscopy study of oriented till blocks, glacial grains and Devonian sands in Estonia and Latvia, *In: Boreas* 29 (1), pp. 35–51
- MAHANEY, W.C.; STEWART, A. & KALM, V. (2001): Quantification of SEM microtextures useful in sedimentary environmental discrimination, *In: Boreas* 30 (2), pp. 165–171
- MANGA, M.; PATEL, A. & DUFEK, J. (2011): Rounding of pumice clasts during transport: field measurements and laboratory studies, *In: Bulletin of Volcanology* 73 (3), pp. 321–333
- MARGOLIS, S. V. (1968): Electron microscopy of chemical solution and mechanical abrasion features on quartz sand grains, *In: Sedimentary Geology* 2 (4), pp. 243–256
- MARGOLIS, S.V. & KRINSLEY, D.H. (1971): Submicroscopic frosting on eolian and subaqueous quartz sand grains, *In: Geological Society of America Bulletin* 82 (12), pp. 3395
- MARSHALL, J. R. (Ed.) (1987): *Clastic Particles. Scanning electron microscopy and shape analysis of sedimentary and volcanic clasts*, New York, Berkshire, Victoria, Ontario, Van Nostrand Reinhold Company Inc, 346 pp.
- MARTIN-KAYE, P.H.A. (1969): A summary of the geology of the Lesser Antilles, *In: Overseas Geological Mineral Resources* 10 (2), pp. 176–206
- MORAL CARDONA, J.P.; GUTIÉRREZ MAS, J.M.; SÁNCHEZ BELLÓN, A.; DOMÍNGUEZ-BELLA, S. & MARTÍNEZ LÓPEZ, J. (2005): Surface textures of heavy-mineral grains: a new contribution to provenance studies, *In: Sedimentary Geology* 174 (3-4), pp. 223–235
- MURPHY, M.D.; SPARKS, R.S.J.; BARCLAY, J.; CARROLL, M.R. & BREWER, T.S. (2000): Remobilization of Andesite Magma by Intrusion of Mafic Magma at the Soufriere Hills Volcano, Montserrat, West Indies, *In: Journal of Petrology* 41 (1), pp. 21–42
- NAGLE, F.; STIPP, J.J.; FISHER, D.E. (1976): K-Ar geochronology of the Limestone Caribbees and Martinique, Lesser Antilles, West Indies, *In: Earth and Planetary Science Letters* 29 (2), pp. 401–412
- NIEDERAUER, K. & SCHÄFER, W. (1985): Das Rasterelektronenmikroskop, *In: Physik in unserer Zeit* 16 (6), pp. 180–190
- PORTER, J.J. (1962): Electron microscopy of sand surface texture, *In: Journal of Sedimentary Research* 32, pp. 124–135
- POWERS, M.C. (1953): A new roundness scale for sedimentary particles, *In: Journal of Sedimentary Petrology* 23 (2), pp. 117–119
- REA, W.J. (1974): The volcanic geology and petrology of Montserrat, West Indies, *In: Journal of the Geological Society* 130 (4), pp. 341–366

- RODGERS, M.; SMITH, P.J.; MATHER, T.A. & PYLE, D.M. (2016): Quiescent-explosive transitions during dome-forming volcanic eruptions: Using seismicity to probe the volcanic processes leading to the 29 July 2008 vulcanian explosion of Soufrière Hills Volcano, Montserrat, *In: Journal of Geophysical Research: Solid Earth* 121 (12), pp. 8453–8471
- ROOBOL, M.J. & SMITH, A.L. (1998): Pyroclastic stratigraphy of the Soufrière Hills volcano, Montserrat - implications for the present eruption, *In: Geophysical Research Letters* 25 (18), pp. 3393–3396
- SELF, S.; WILSON, L. & NAIRN, I.A. (1979): Vulcanian eruption mechanisms, *In: Nature* 277, pp. 440–443
- SETLOW, L.W. & KARPOVICH, R.P. (1972): "Glacial" micro-textures on quartz and heavy mineral sand grains from the littoral environment, *In: Journal of Sedimentary Research* 42 (4), pp. 864–875
- SHERIDAN, M.F. & WOHLTZ, K. (1983): Hydrovolcanism: basic considerations and review, *In: Journal of Volcanology and Geothermal Research* 17, pp. 1–29
- SIGURDSSON, H. (Ed.) (2015): The Encyclopedia of Volcanoes. 2nd revised edition, San Diego, Elsevier Science Publishing Co Inc, 1456 pp.
- SMITH, R.L. (1960): Ash Flows, *In: Bulletin of the Geological Society of America* 71, pp. 795–842
- SMITH, G. A.; SMITH, R. D. (1985): Specific Gravity Characteristics of Recent Volcaniclastic Sediment: Implications for Sorting and Grain Size Analysis, *In: The Journal of Geology* 93 (5), pp. 619–622
- SMITH, A.L.; ROOBOL, M.J.; SCHELLEKENS, J.H. & MATTIOLI, G.S. (2007): Prehistoric stratigraphy of the Soufrière Hills-South Soufrière Hills volcanic complex, Montserrat, West Indies, *In: Journal of Geology* 115, pp. 115–127
- SOUTENDAM C.J.A. (1967): Some methods to study surface textures of sand grains, *In: Sedimentology* 8 (4), pp. 281–290
- SPARKS, R.S.J.; SIGURDSSON, H. & CAREY, S.N. (1980): The entrance of pyroclastic flows into the sea, II. Theoretical considerations on subaqueous emplacement and welding, *In: Journal of Volcanology and Geothermal Research* 7, pp. 97–105
- SPARKS, R.S.J. & YOUNG, S.R. (2002): The eruption of Soufrière Hills Volcano, Montserrat (1995-1999): overview of scientific results, *In: DRUITT, T.H. & KOKELAAR, B.P. (Eds.) (2002): The Eruption of Soufrière Hills Volcano, Montserrat, from 1995 to 1999. Geological Society, London, Memoirs* 21, pp. 45–69
- STINTON, A. J.; COLE, P. D.; ODBERT, H. M.; CHRISTOPHER, T.; AVARD, G. & BERNSTEIN, M. (2014): Chapter 6 Dome growth and valley fill during Phase 5 (8 October 2009–11 February 2010) at the Soufrière Hills Volcano, Montserrat, *In: WADGE, G.; ROBERTSON, G.E.A. & VOIGHT, B. (Eds.) (2014): The Eruption of Soufriere Hills Volcano, Montserrat from 2000 to 2010, Geological Society, London, Memoirs* 39, pp. 113–131
- TROFIMOV, J.; AMY, L.; BOUDON, G.; DEPLUS, C.; DOYLE, E.; FOURNIER, N.; HART, M.B.; KOMOROWSKI, J.C.; LE FRIANT, A.; LOCK, E.J.; PUDSEY, C.; RYAN, G.; SPARKS, R.S.J. & TALLING, P.J. (2006): Submarine pyroclastic deposits formed at the Soufrière Hills volcano, Montserrat (1995–2003): What happens when pyroclastic flows enter the ocean?, *In: Geology* 34 (7), pp. 549
- TROFIMOV, J.; SPARKS, R.S.J. & TALLING, P.J. (2008): Anatomy of a submarine pyroclastic flow and associated turbidity current: July 2003 dome collapse, Soufrière Hills volcano, Montserrat, West Indies, *In: Sedimentology* 55 (3), pp. 617–634
- TUCKER, M. (1996): Methoden der Sedimentologie. 223 Abbildungen, 38 Tabellen, Stuttgart: Enke Verlag, 366 pp.
- UDDEN, J.A. (1914): Mechanical Composition of clastic sediments, *In: Bulletin of the Geological Society of America* 25, pp. 655–744

- VOIGHT, B.; KOMOROWSKI, J.-C.; NORTON, G. E.; BELOUSOV, A. B.; BELOUSOVA, M.; BOUDON, G.; FRANCIS, P. W.; FRANZ, W.; HEINRICH, P.; SPARKS, R. S. J.; YOUNG, S. R. (2002): The 26 December (Boxing Day) 1997 sector collapse and debris avalanche at Soufrière Hills Volcano, Montserrat, *In: DRUITT, T.H. & KOKELAAR, B.P. (Eds.) (2002): The Eruption of Soufrière Hills Volcano, Montserrat, from 1995 to 1999*, Geological Society, London, Memoirs 21, pp. 363–407
- VOS, K.; VANDENBERGHE, N. & ELSEN, J. (2014): Surface textural analysis of quartz grains by scanning electron microscopy (SEM): From sample preparation to environmental interpretation, *In: Earth-Science Reviews* 128, pp. 93–104
- WADGE, G. & SHEPHERD, J.B. (1984): Segmentation of the Lesser Antilles subduction zone, *In: Earth and Planetary Science Letters* 71, pp. 197–304
- WADGE, G.; ROBERTSON, G.E.A. & VOIGHT, B. (Eds.) (2014a): The Eruption of Soufriere Hills Volcano, Montserrat from 2000 to 2010, Geological Society, London, Memoirs 39
- WADGE, G.; VOIGHT, B.; SPARKS, R.S.J.; COLE, P.D.; LOUGHLIN, S.C. & ROBERTSON, R.E.A. (2014b): Chapter 1 An overview of the eruption of Soufrière Hills Volcano, Montserrat from 2000 to 2010, *In: WADGE, G.; ROBERTSON, G.E.A. & VOIGHT, B. (Eds.) (2014): The Eruption of Soufriere Hills Volcano, Montserrat from 2000 to 2010*, Geological Society, London, Memoirs 39, pp. 1–39
- WALKER, G.P.L. (1971): Grain-size characteristics of pyroclastic deposits, *In: Journal of Geology* 79, pp. 696–714
- WALKER, G.P.L. & CROASDALE, R. (1972): Characteristics of Some Basaltic Pyroclastics, *In: Bulletin of Volcanology* 35, pp. 303–317
- WENTWORTH, C.K. (1922): A scale of grade and class terms for clastic sediments, *In: Journal of Geology* 30 (5), pp. 377–392
- WESTERCAMP, D. (1988): Magma generation in the Lesser Antilles: geological constraints, *In: Tectonophysics* 149 (1-2), pp. 145–163
- WHALLEY, W.B. & KRINSLEY, D.H. (1974): A scanning electron microscope study of surface textures of quartz grains from glacial environments, *In: Sedimentology* 21, pp. 87–105
- WHITNEY, D.L.; EVANS, B.W. (2010): Abbreviations for names of rock-forming minerals, *In: American Mineralogist* 95 (1), pp. 185–187
- WOHLETZ, K. H. (1983): Chemical and textural surface features of pyroclasts from hydrovolcanic eruption sequences, *In: Los Alamos National Laboratory Report LA-UR 83-250*, 35 pp.
- WOHLETZ, K. H. (1987): Chapter 2-2 Chemical and textural surface features of pyroclasts from hydrovolcanic eruption sequences, *In: MARSHALL, J. R. (Ed.) (1987): Clastic Particles. Scanning electron microscopy and shape analysis of sedimentary and volcanic clasts*, New York, Berkshire, Victoria, Ontario, Van Nostrand Reinhold Company Inc, pp. 79–97
- WOHLETZ, K.H. & KRINSLEY, D. (1982): Scanning electron microscopy of basaltic hydromagmatic ash, *In: Los Alamos National Laboratory Report LA-UR 82-1433*, 43 pp.
- ZELLMER, G.F.; HAWKESWORTH, C.J.; SPARKS, R.S.J.; THOMAS, L.E.; HARFORD, C.L.; BREWER, T.S. & LOUGHLIN, S.C. (2003): Geochemical Evolution of the Soufriere Hills Volcano, Montserrat, Lesser Antilles Volcanic Arc, *In: Journal of Petrology* 44 (8), pp. 1349–1374

APPENDIX

Appendix 1 – Vibrocores JR123-15-V and JR123-23-V adopted from TROFIMOV ET AL. (2008)

Appendix 2 – Calculation and Classification of statistic parameters after FOLK & WARD (1953)

Appendix 3 – Roundness scale after POWERS (1953)

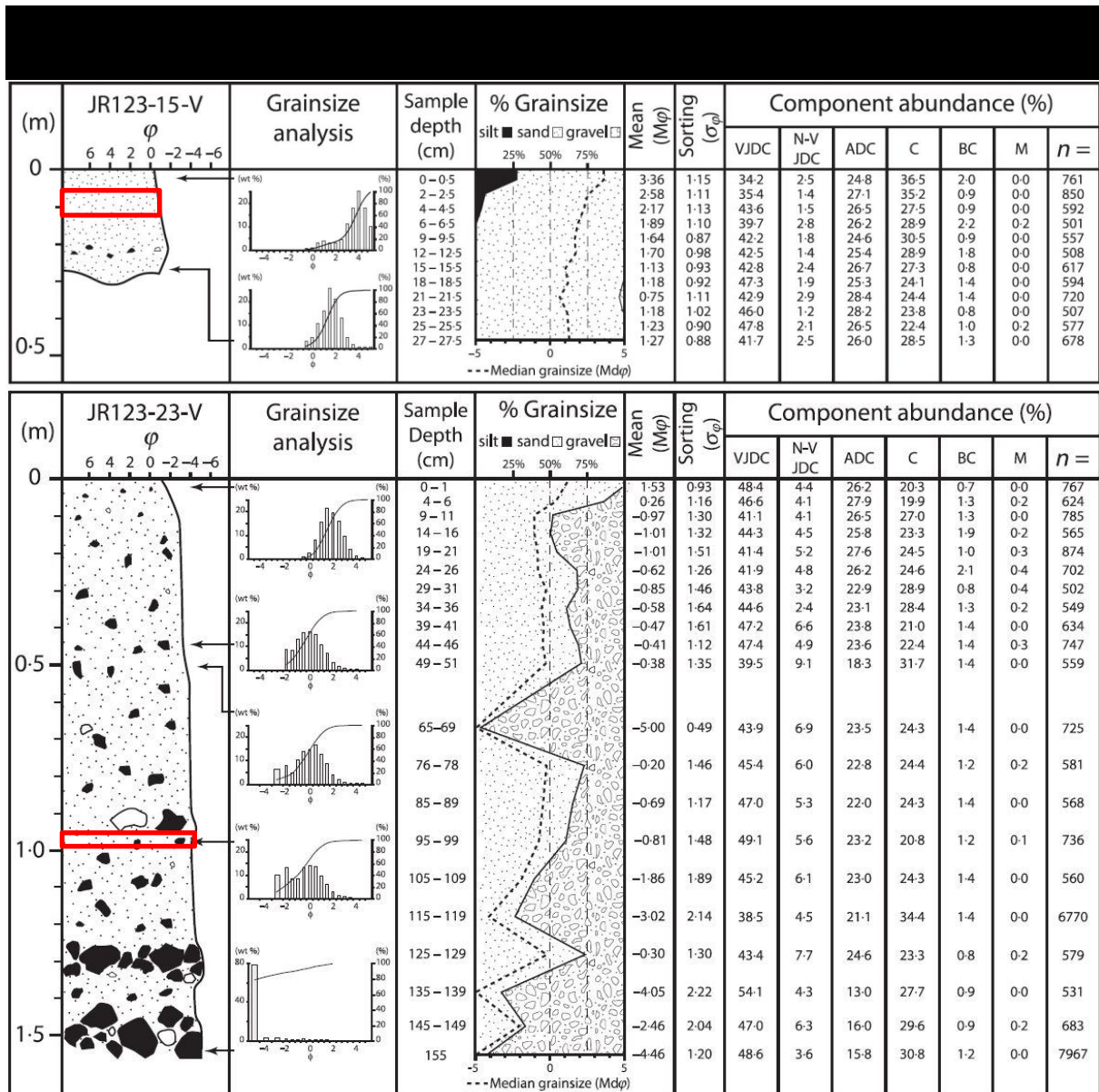
Appendix 4 – Cumulative frequency curves of all samples

Appendix 5 – Overview of the results of the point counting measurements

Appendix 6 – Overview of the microtextures and their amount in each sample

Appendix 7 – Overview of the cumulative weight percentages of the microtextures

Appendix 8 – Overview and best representing images of the microtextures

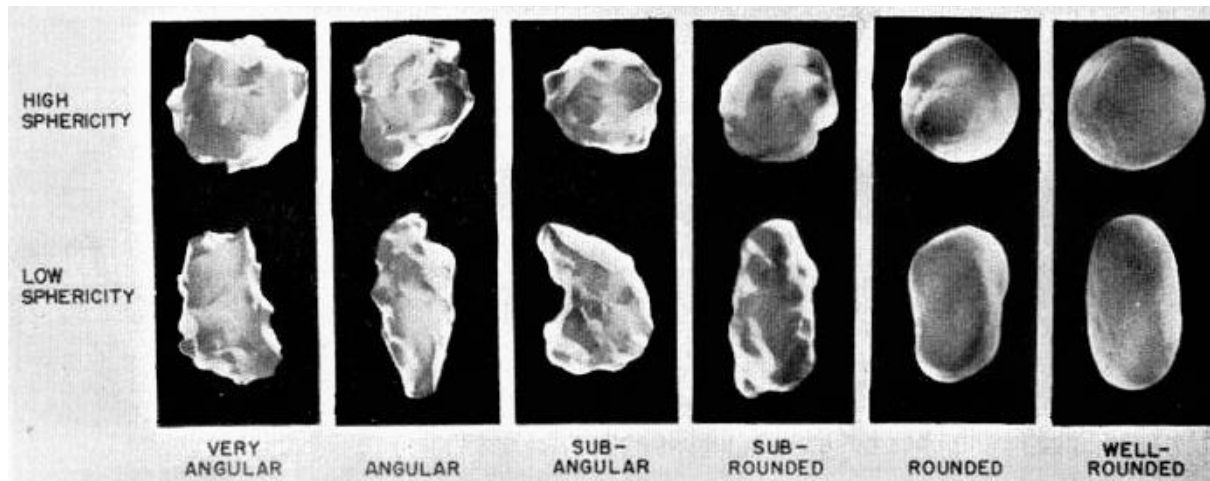


Appendix 2: Calculation and classification of the statistic parameter mean, standard deviation (sorting), skewness and Kurtosis after Folk & Ward (1957)

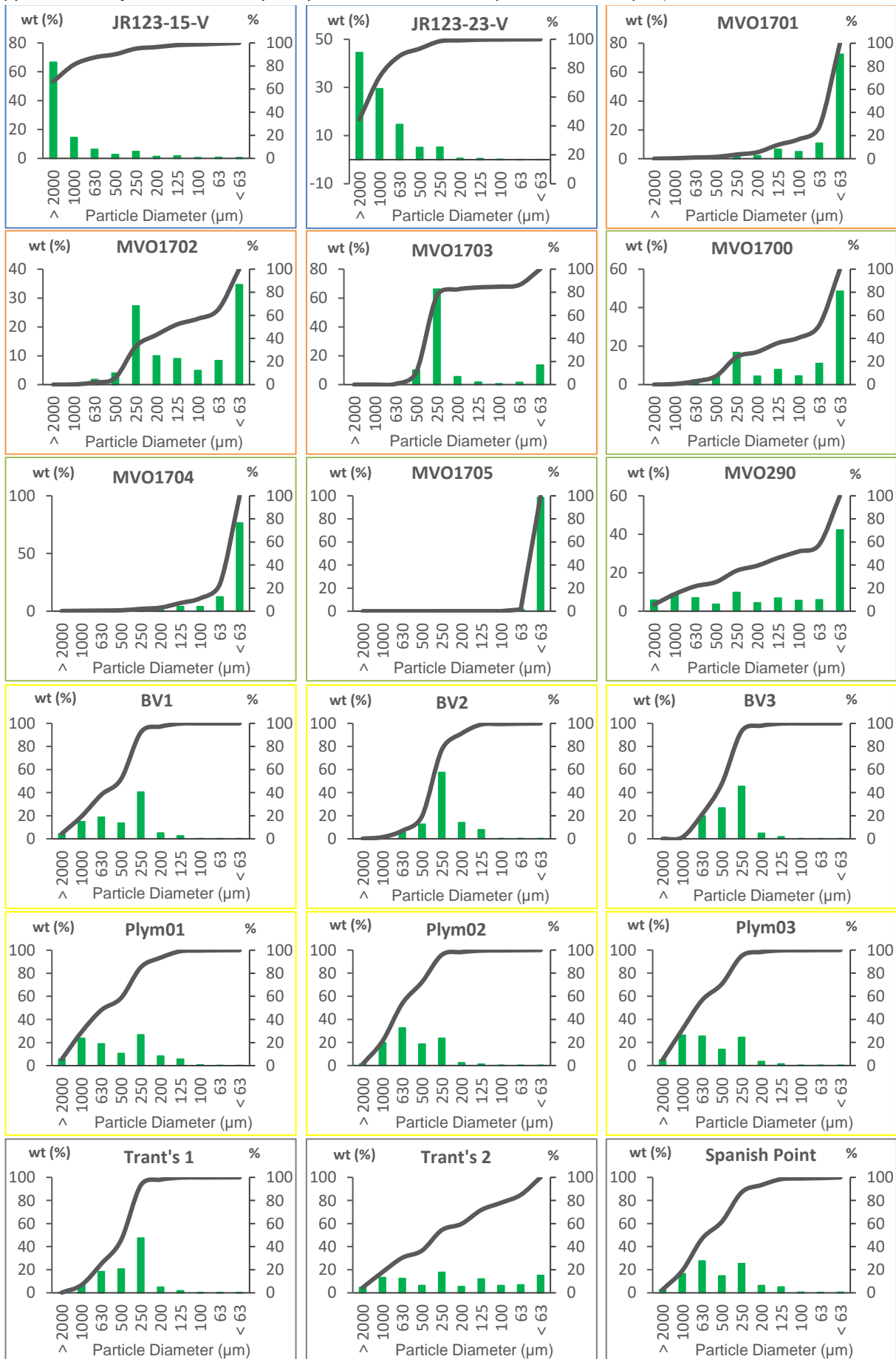
(d) Logarithmic (original) Folk and Ward (1957) graphical measures

Mean	Standard deviation	Skewness	Kurtosis		
$M_Z = \frac{\phi_{16} + \phi_{50} + \phi_{84}}{3}$	$\sigma_I = \frac{\phi_{84} - \phi_{16}}{4} + \frac{\phi_{95} - \phi_5}{6.6}$	$Sk_I = \frac{\phi_{16} + \phi_{84} - 2\phi_{50}}{2(\phi_{84} - \phi_{16})} + \frac{\phi_5 + \phi_{95} - 2\phi_{50}}{2(\phi_{95} - \phi_5)}$	$K_G = \frac{\phi_{95} - \phi_5}{2.44(\phi_{75} - \phi_{25})}$		
Sorting (σ_1)	Skewness (Sk_1)	Kurtosis (K_G)			
Very well sorted	<0.35	Very fine skewed	+0.3 to +1.0	Very platykurtic	<0.67
Well sorted	0.35–0.50	Fine skewed	+0.1 to +0.3	Platykurtic	0.67–0.90
Moderately well sorted	0.50–0.70	Symmetrical	+0.1 to -0.1	Mesokurtic	0.90–1.11
Moderately sorted	0.70–1.00	Coarse skewed	-0.1 to -0.3	Leptokurtic	1.11–1.50
Poorly sorted	1.00–2.00	Very coarse skewed	-0.3 to -1.0	Very leptokurtic	1.50–3.00
Very poorly sorted	2.00–4.00			Extremely leptokurtic	>3.00
Extremely poorly sorted	>4.00				

Appendix 3: Roundness classes after POWERS (1953) used for the grain shape analysis.



Appendix 4: Cumulative frequency curves of all samples sorted after source (offshore, vulcanian ashfall, copyroclastic ashfall, Belham Valley & Plymouth and Trant's & Spanish Point samples). For color code see Table 4.



Appendix 5: Results of the point counting measurement in vol.-%; the group 'rock fragments' (porphyritic lava fragments) comprises groundmass and phenocrysts to get an overview of the crystallinity of the components (see the red boxes). The red box to the right shows the cumulative weight percentage of the phenocrysts and groundmass.

	Plagioclase	Rock fragments	Amphibole	Pyroxene	Opaque minerals	Biogenic fragments	Accessory minerals	Rock fragments groundmass	Rock fragments phenocrysts
JR123-15-V	43.17	31.18	3.20	4.43	9.45	5.96	2.62	78.55	21.45
JR123-23-V	38.50	45.76	3.06	6.65	3.85	1.40	0.79	71.70	28.30
MVO1701	43.15	52.50	1.94	1.61	0.81	0.00	0.00	81.87	18.13
MVO1702	42.01	53.92	0.98	1.31	1.55	0.00	0.24	85.78	14.22
MVO1703	35.13	61.04	1.42	1.49	0.92	0.00	0.00	79.19	20.81
MVO1700	41.70	52.55	1.75	1.46	2.55	0.00	0.00	70.22	29.78
MVO1704	41.80	51.15	3.26	1.32	2.29	0.00	0.18	75.69	24.31
MVO290	46.53	48.43	1.83	1.61	1.53	0.00	0.07	76.02	23.98
BV1	44.86	41.17	1.85	8.67	1.77	1.61	0.08	70.18	29.82
BV2	22.49	21.57	4.89	13.31	37.32	0.08	0.34	67.19	32.81
BV3	31.46	27.59	11.59	20.09	9.16	0.00	0.11	63.20	36.80
Plym01	39.98	50.16	4.44	2.28	2.93	0.00	0.22	69.98	30.02
Plym02	42.13	42.40	6.67	4.93	3.20	0.27	0.40	73.27	26.73
Plym03	44.75	43.31	5.86	2.32	3.43	0.11	0.22	67.35	32.65
Trant's 1	16.27	16.92	11.46	9.31	45.82	0.00	0.21	66.46	33.54
Trant's 2	37.27	55.52	3.06	0.87	3.06	0.00	0.22	72.64	27.36
Spanish Point	40.98	50.78	5.50	1.08	1.67	0.00	0.00	70.12	29.88

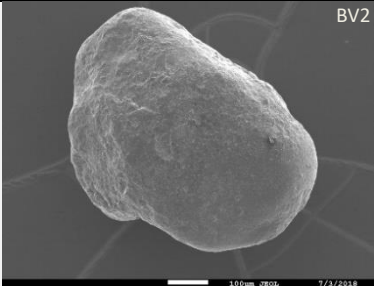
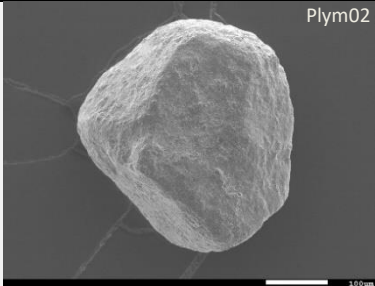
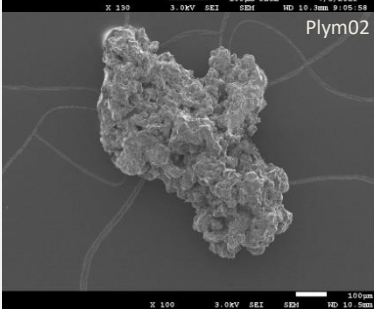
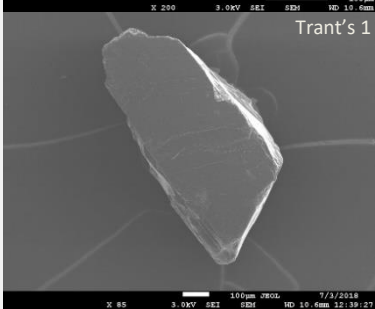
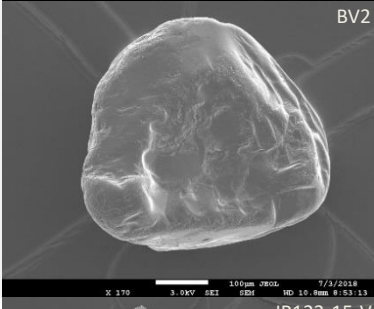
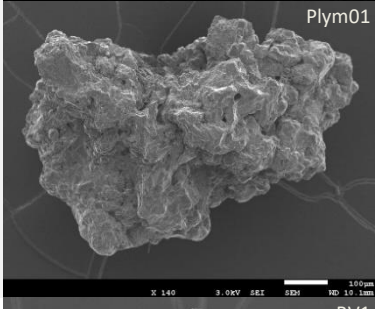
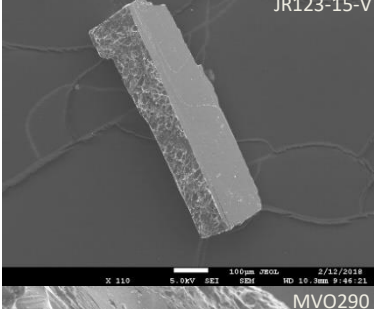
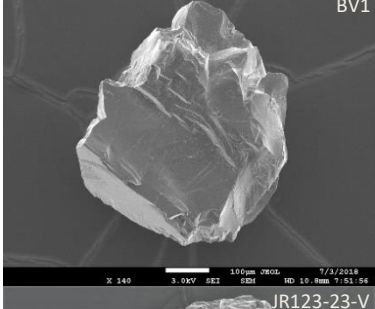
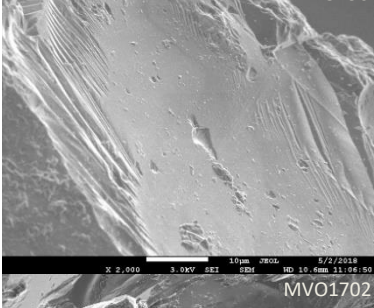
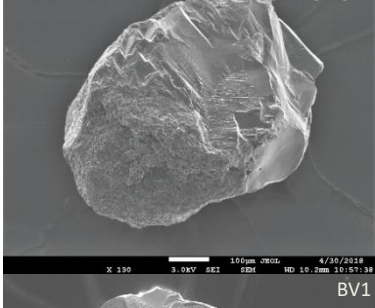
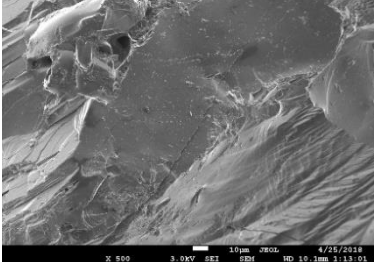
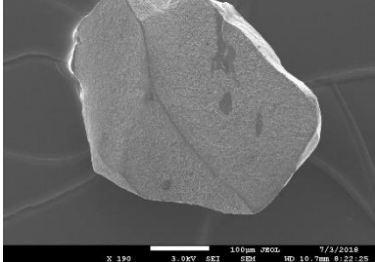
Appendix 6: Counted microtextures on grain surfaces analysed from each sample. For samples JR123-15-V, MVO1700 and MVO1702 70 grains were analysed and for the rest 50 grains per sample. The different colours represent the individual sample groups: blue – offshore samples, red – vulcanian eruption ashfall samples, green – co-pyroclastic flow ashfall samples, yellow – Belham Valley and Plymouth samples and grey – Trant’s and Spanish Point samples. Color code is adopted from Table 4.

Microtextures		#	JR123-15-V	JR123-23-V	MVO1701	MVO1702	MVO 1703	MVO 1700	MVO1704	MVO1705	MVO290	BV1	BV2	BV3	Plym01	Plym02	Plym03	Trant's 1	Trant's 2	Spanish Point
Grain outline	Low	1	0	0	0	0	0	3	4	2	0	2	3	1	2	0	1	2	0	1
	Medium	2	25	17	25	11	17	27	17	18	24	19	16	17	7	11	16	24	16	11
	High	3	45	33	25	59	33	40	29	30	26	29	31	32	41	39	33	24	34	38
Relief	Low	4	6	9	7	5	6	17	3	4	4	6	3	3	4	2	2	10	8	6
	Medium	5	32	15	13	18	18	28	19	13	18	15	18	12	12	12	17	17	13	9
	High	6	32	26	30	47	26	25	28	33	28	29	29	35	34	36	31	23	29	35
Mechanical features	Flat cleavage surface	7	11	13	5	11	4	19	5	1	6	2	4	3	8	4	2	9	4	4
	Fresh surface	8	30	23	11	16	5	14	6	5	15	8	0	0	2	1	4	8	4	5
	Crater	9	42	27	17	21	26	25	41	38	29	35	33	32	40	35	32	37	43	38
	Sawtooth structure	10	2	4	3	10	3	11	2	1	4	5	1	2	4	4	4	6	5	4
	Microcracks	11	10	14	14	25	17	30	25	9	21	5	4	6	13	8	11	4	6	17
	Abrasion features	12	5	1	1	2	3	1	2	0	2	1	0	1	1	1	4	1	0	1
	Parallel ridges	13	19	14	10	11	5	16	6	14	16	2	3	4	4	6	7	3	8	5
	Grain rounding	14	19	19	13	8	13	21	9	13	12	18	7	11	12	8	13	21	9	14
	Chipped edges	15	29	31	15	6	9	21	24	24	18	19	17	27	33	23	26	31	24	15
	Conchoidal fractures	16	41	39	25	40	26	45	36	31	28	21	21	27	27	23	28	32	30	27
	Grooves/scratches	17	25	12	4	2	4	18	7	7	20	12	6	11	6	6	8	11	9	8
	Radial fractures	18	7	2	0	3	4	5	2	1	2	0	2	2	3	1	0	6	4	3
	Sharp angular features	19	9	11	8	18	5	13	5	7	9	3	4	1	10	2	1	2	1	0
	Arcuate steps	20	29	40	30	31	39	47	33	25	24	22	17	18	22	22	21	22	23	22
	Straight steps	21	30	21	25	41	39	42	36	27	27	22	15	16	24	28	25	24	25	27
	Upturned plates	22	1	1	6	4	6	7	6	4	4	3	2	5	1	5	8	2	5	4
Broken plates	23	1	1	1	3	0	0	2	0	1	0	2	0	5	0	0	0	0	2	
V-shaped percussion cracks	24	11	1	1	2	4	1	6	2	4	3	3	2	2	2	3	2	1	2	
Chemical features	Dissolution etching	25	38	16	20	18	21	36	28	28	30	33	24	30	32	28	24	25	28	31
	Vesicularity (Glassy coating)	26	12	19	25	45	16	14	7	5	26	10	14	9	12	10	13	8	9	12
	Weathered surface	27	20	8	12	12	16	27	18	12	16	13	9	9	13	17	14	14	14	14
	Precipitation features	28	5	0	4	0	10	6	18	10	1	6	0	8	2	2	3	0	3	0
	Dissolved crystals	29	13	2	2	4	1	9	6	1	4	2	4	5	2	6	2	2	2	1
	Crystal growth	30	2	3	5	1	2	5	21	11	2	3	1	8	2	8	8	7	9	6
	Scaling	31	2	7	3	8	7	6	10	8	7	2	1	0	2	0	1	2	1	5
Pits	32	17	13	22	16	22	26	27	11	13	13	16	23	38	31	36	40	38	44	
Other features	Elongated depressions	33	13	5	1	0	2	4	4	2	1	4	5	5	7	3	1	3	2	4
	Adhering particles	34	28	23	18	49	20	56	38	38	34	9	9	4	33	40	36	35	45	46
	Droplike or fused skin	35	0	1	3	0	1	2	0	1	0	8	0	0	3	6	0	4	4	3
	Blocky, curvy-planar surfaces	36	59	46	31	37	28	54	39	36	39	32	43	41	34	35	37	32	32	24

Appendix 7: Similar to Appendix 5 but showing the cumulative weight percentages of the microtextures for each sample. Color code is adopted from Table 4.

Microtextures		#	JR123-15-V	JR123-23-V	MVO1701	MVO1702	MVO 1703	MVO 1700	MVO1704	MVO1705	MVO290	BV1	BV2	BV3	Plym01	Plym02	Plym03	Trant's 1	Trant's 2	Spanish Point
Grain outline	Low	1	0	0	0	0	0	4	8	4	0	4	6	2	4	0	2	4	0	2
	Medium	2	36	34	50	16	34	39	34	36	48	38	32	34	14	22	32	48	32	22
	High	3	64	66	50	84	66	57	58	60	52	58	62	64	82	78	66	48	68	76
Relief	Low	4	9	18	14	7	12	24	6	8	8	12	6	6	8	4	4	20	16	12
	Medium	5	46	30	26	26	36	40	38	26	36	30	36	24	24	24	34	34	26	18
	High	6	46	52	60	67	52	36	56	66	56	58	58	70	68	72	62	46	58	70
Mechanical features	Flat cleavage surface	7	16	26	10	16	8	27	10	2	12	4	8	6	16	8	4	18	8	8
	Fresh surface	8	43	46	22	23	10	20	12	10	30	16	0	0	4	2	8	16	8	10
	Crater	9	60	54	34	30	52	36	82	76	58	70	66	64	80	70	64	74	86	76
	Sawtooth structure	10	3	8	6	14	6	16	4	2	8	10	2	4	8	8	8	12	10	8
	Microcracks	11	14	28	28	36	34	43	50	18	42	10	8	12	26	16	22	8	12	34
	Abrasion features	12	7	2	2	3	6	1	4	0	4	2	0	2	2	2	8	2	0	2
	Parallel ridges	13	27	28	20	16	10	23	12	28	32	4	6	8	8	12	14	6	16	10
	Grain rounding	14	27	38	26	11	26	30	18	26	24	36	14	22	24	16	26	42	18	28
	Chipped edges	15	41	62	30	9	18	30	48	48	36	38	34	54	66	46	52	62	48	30
	Conchoidal fractures	16	59	78	50	57	52	64	72	62	56	42	42	54	54	46	56	64	60	54
	Grooves/scratches	17	36	24	8	3	8	26	14	14	40	24	12	22	12	12	16	22	18	16
	Radial fractures	18	10	4	0	4	8	7	4	2	4	0	4	4	6	2	0	12	8	6
	Sharp angular features	19	13	22	16	26	10	19	10	14	18	6	8	2	20	4	2	4	2	0
	Arcuate steps	20	41	80	60	44	78	67	66	50	48	44	34	36	44	44	42	44	46	44
	Straight steps	21	43	42	50	59	78	60	72	54	54	44	30	32	48	56	50	48	50	54
	Upturned plates	22	1	2	12	6	12	10	12	8	8	6	4	10	2	10	16	4	10	8
	Broken plates	23	1	2	2	4	0	0	4	0	2	0	4	0	10	0	0	0	0	4
V-shaped percussion cracks	24	16	2	2	3	8	1	12	4	8	6	6	4	4	4	6	4	2	4	
Chemical features	Dissolution etching	25	54	32	40	26	42	51	56	56	60	66	48	60	64	56	48	50	56	62
	Vesicularity (Glassy coating)	26	17	38	50	64	32	20	14	10	52	20	28	18	24	20	26	16	18	24
	Weathered surface	27	29	16	24	17	32	39	36	24	32	26	18	18	26	34	28	28	28	28
	Precipitation features	28	7	0	8	0	20	9	36	20	2	12	0	16	4	4	6	0	6	0
	Dissolved crystals	29	19	4	4	6	2	13	12	2	8	4	8	10	4	12	4	4	4	2
	Crystal growth	30	3	6	10	1	4	7	42	22	4	6	2	16	4	16	16	14	18	12
	Scaling	31	3	14	6	11	14	9	20	16	14	4	2	0	4	0	2	4	2	10
	Pits	32	24	26	44	23	44	37	54	22	26	26	32	46	76	62	72	80	76	88
Other features	Elongated depressions	33	19	10	2	0	4	6	8	4	2	8	10	10	14	6	2	6	4	8
	Adhering particles	34	40	46	36	70	40	80	76	76	68	18	18	8	66	80	72	70	90	92
	Droplike or fused skin	35	0	2	6	0	2	3	0	2	0	16	0	0	6	12	0	8	8	6
	Blocky, curvy-planar surfaces	36	84	92	62	53	56	77	78	72	78	64	86	82	68	70	74	64	64	48

Appendix 8: Overview of the microtextures distinguished on the analysed grains presented with the best image.

MICRO TEXTURE	No.	EXAMPLE	No.	EXAMPLE
Grain outline & Relief	1	 BV2	2	 Plym02
	3	 Plym02	4	 Trant's 1
	5	 BV2	6	 Plym01
	7	 JR123-15-V	8	 BV1
	9	 MVO290		 JR123-23-V
	11	 MVO1702	12	 BV1

